Metal-organic networks and metal-porphyrins on superconducting Pb(111): structural, electronic and magnetic properties

Dissertation
zur Erlangung des Grades eines Dr. rer.nat.

am Fachbereich Physik
der Freien Universität Berlin

Gelavizh Ahmadi

Berlin, 2017

Diese Arbeit entstand in der Arbeitsgruppe von Prof. Dr. Katharina J. Franke am Fachbereich Physik der Freien Universität Berlin.

Berlin, 25.07.2017

Erstgutachterin: Prof. Dr. Katharina J. Franke
Zweitgutachter: Prof. Dr. Wolfgang Kuch

Datum der Disputation: 21.09.2017

“Gedruckt mit Unterstutzung des Deutschen Akademischen Austauschdienstes“

To my mother

"I don’t want to believe, I want to know"

Carl Sagan

Abstract

In this thesis, we investigate the formation of self-assembled magnetic nanostructures on the superconducting surface Pb(111). Their structure, electronic and magnetic properties are analyzed by mean of scanning tunneling microscopy (STM) and spectroscopy (STS). Two major strategies are considered to produce such magnetic nanostructures: (1) *in-situ* self-organization between metal atoms and organic molecules. (2) Long range ordering of metallated molecules. The magnetic fingerprint of such nanostructures gives some insight into the antagonistic interaction of the magnetic impurities and the underlying superconducting substrate.

In the first part, structural and electronic properties of tetracyanonaphtho-quinodimethane (TNAP) based metal-organic networks on a superconducting Pb(111) surface are studied. At low temperatures, the TNAP molecules form densely packed islands. When deposited at room temperature, Pb adatoms are incorporated into fourfold bonding nodes with the TNAP molecules leading to long-range ordered porous structures. Co-deposition of NaCl with TNAP yields a Na source for an ionically bonded Na-TNAP structure. Fourfold bonding motives are also created by Fe atoms with the cyano terminations of TNAP. However, the structures are irregular and do not sustain the formation of long-range ordered networks. Some Fe centers with molecules surrounded in a local C_2 symmetry exhibit Shiba states as a fingerprint of a magnetic interaction with the superconducting surface.

In the second part, the self-assembly of metal-porphyrin complexes on Pb(111) is studied. Deposition of iron-tetrapyridine porphyrin (Fe-TPyP) yields long-range molecular islands, which consist of two types of molecules (type A and B). Due to the deformation of the porphyrin macrocycle, both types of the Fe-TPyP molecules show different magnetic fingerprints depending on the overlap between the Fe center and the underlying substrate. In the superconducting state, type A molecules exhibit two Yu-Shiba-Rusinov states at different energies, which are both localized over the whole molecule. One state lies inside the superconducting gap and is correlated to the Kondo resonance seen in the normal state. Interestingly, the ratio between the intensities of the electron-like and hole-like quasiparticle of this Shiba state changes in the same manner as the change of the asymmetry factor of the Fano line-shape of the Kondo resonance over the molecule. Type B molecules exhibit two spin excitations that are extended over the ligand of the molecule. Finally, we study the effect of the substitution of the Fe center to the manganese (Mn) atom that has a different spin state. Moreover, to manipulate the coupling of the Mn center to the substrate, we changed the pyridine end groups to tert-butyl groups. Deposition of the Mn-TPyP molecules yields self-assembled long ranged ordered molecular islands that differ from what is observed with Fe-TPyP molecules although the organic ligand is the same. Self-assembled manganese tetra-phenyl-tert-butyl-porphyrin molecules (Mn-TPTBP) adapt a rectangular arrangement, which is not commensurate with the substrate. For both molecules, Mn-TPyP and Mn-TPTBP, a Shiba state at the gap edge with a *free spin* ground state is observed.

Kurzfassung

Die vorliegende Dissertationsschrift beschäftigt sich mit selbstanordnenden magnetischen Nanostrukturen auf einem supraleitenden Pb(111) Substrat. Deren strukturellen, elektronischen und magnetischen Eigenschaften werden dabei mit Hilfe von Rastertunnelmikroskopie (STM) und -spektroskopie (STS) untersucht. Betrachtet wurden zwei Strategien zur Bildung von magnetischen Nanostrukturen: (1) Die In-situ Selbstanordnung von Metallatomen und organischen Molekülen sowie (2) die Ordnung von bereits metallierten Molekülen. Die geschaffenen Konfigurationen ermöglichen einen Einblick in die Wechselwirkung zwischen den komparativen Phänomenen Supraleitung und Magnetismus.

Das erste Kapitel beschäftigt sich mit Tetracyanonaphtho-quinodimethane (TNAP) basierten metallorganischen Netzwerken auf Pb(111). Bei tiefen Temperaturen bilden sich dicht gepackte TNAP-Inseln. Bei Raumtemperatur hingegen formen sich weitreichend geordnete vierfach symmetrische metallorganische Netzwerk aus Pb-Adatomen und TNAP Molekülen. Gleichzeitiges Aufbringen von NaCl und TNAP führt zur Bildung einer ionisch gebundenen Na-TNAP Struktur. Vierfach symmetrische Bindungen werden ebenfalls erzeugt durch Fe Atome und TNAP mit Cyano-Endgruppe. Jene Strukturen sind jedoch unregelmäßig und somit nicht weitreichend geordnet. Manche der Fe-Zentren, die von Molekülen in einer lokalen C_2-Symmetrie umgeben sind weisen Yu-Shiba-Rusinov Zustände (Shiba-Zustände) auf, die einen Hinweis auf die magnetische Wechselwirkung mit dem supraleitenden Substrat sind.

Im zweiten Teil wird die Selbstordnung von Metallporphyrin-Komplexen auf Pb(111) untersucht. Die Deponierung von Eisen-tetrapyridin porphyrin (Fe-TPyP) erzeugt weitreichend Molekülinseln, die zwei Arten Moleküle enthalten, aufgrund der unterschiedlichen Deformation des Porphyrinrings auf der Oberfläche. Dies führt zu unterschiedlichem Überlapp der Fe-Zustände mit dem Substrat und damit zu verschiedenen magnetischen Signaturen. Im supraleitenden Zustand weisen erstere zwei über das Molekül delokalisierte Shiba-Zustände auf. Einer dieser Zustände korreliert mit einer Kondo Resonanz im normalleitenden Zustand. Interessanterweise ändert sich über dem Molekül das Verhältnis der Intensitäten von elektronen- zu lochartigen Quasiteilchen jenes Shiba-Zustandes in derselben Weise wie die Asymmetrie der Kondo-Linienform. Beim zweiten Molekültyp hingegen sind zwei Spin-Anregungen messbar, die sich über den Liganden des Moleküls erstrecken.

Der letzte Teil untersucht die Substituierung des zentralen Eisenatoms durch Mangan (Mn) und die sich dadurch ergebene Änderung des Spin-Zustands. Des Weiteren wurde durch die Modifikation des organischen Liganden die Kopplung des Metallzentrums zum Substrat geändert. Das Aufdampfen der Mn-TPyP Moleküle führt wieder zu weitreichend geordneten Strukturen, die sich jedoch – trotz desselben Liganden - von der geordneten Struktur von Fe-TPyP unterscheiden. Die selbstordnenden Mangan-tetra-phenyl-tert-butyl-porphyrin (Mn-TPTBP) Moleküle formen rechteckige Strukturen, die nicht kommensurabel mit dem Substrat sind. Beide Strukturen zeigen einen Shiba-Zustand, der zu einem Grundzustand mit freiem Elektronenspin gehört.

Contents

1 Introduction **3**

2 Fundamentals of scanning tunneling microscopy **7**

2.1 Scanning tunneling microscopy and spectroscopy 7

2.1.1 Fundamentals of STM 7

2.1.2 Theory of scanning tunneling microscopy 8

2.1.3 Theory of scanning tunneling spectroscopy 11

2.2 Sample preparation 13

2.3 Experimental setup 15

3 Fundamentals of superconductivity and magnetism **19**

3.1 Superconductivity 20

3.1.1 Bardeen-Cooper-Schrieffer theory of superconductivity 20

3.1.2 Scanning tunneling spectroscopy on superconductors 22

3.2 Magnetic impurities on a superconductor 23

3.2.1 Ligand field 23

3.2.2 Magnetic anisotropy 24

3.2.3 The Kondo effect 26

3.2.4 Magnetic impurity on a superconducting substrate 30

4 Metal-organic networks on Pb(111) **35**

4.1 Introduction 35

4.2 Experimental details 36

4.3 Results and discussion 38

4.3.1 TNAP on Pb(111) 38

4.3.2 Pb-TNAP coordination network on Pb(111) . . . 39
4.3.3 Na-TNAP metal-organic network . . . 41
4.3.4 Fe-TNAP metal-organic network . . . 43
4.4 Conclusions . . . 44

5 Metal-organic complexes on Pb(111) 47
5.1 Introduction . . . 47
5.2 Experimental details . . . 49
5.3 Self assembly of magnetic iron-porphyrin complex on Pb(111)) . . . 49
5.3.1 STM study of ordered Fe-TPyP molecules on Pb(111) . . . 50
5.3.2 Electronic properties of Fe-TPyP molecules on Pb(111) . . . 52
5.3.3 Magnetic properties of Fe-TPyP molecules on Pb(111) . . . 57
5.3.4 Bistable molecules: a molecule with both magnetic fingerprints . . . 79
5.3.5 Summary . . . 81
5.4 Manganese-porphyrin on Pb(111): importance of the central metal . . . 82
5.4.1 STM investigation of Mn-TPyP on Pb(111) . . . 82
5.4.2 Electronic and magnetic properties of Mn-TPyP molecules . . . 84
5.4.3 Summary . . . 85
5.5 Mn-TPTBP molecules on Pb(111): exchanging the end groups . . . 86
5.5.1 Summary . . . 87
5.6 Conclusions . . . 88

6 Summary and conclusion 89

References 93

List of Abbreviations 107

List of Publications 108

Conference Contributions 108

Chapter 1

Introduction

Data processing and data storage are of extreme importance in everyday life. They are the basis of all computers, mobile phones, DVD players, etc. Our society is demanding always faster and smaller devices. However, common semiconductor technology is approaching its physical limit of miniaturization. Ultimately, the goal is to store data in a single atom, where the spin state carries the information. To achieve this goal, basic research strategies focus on producing the intelligent nanostructured systems, in which the spin of one atom can be stabilized in a particular state, switched by an external writing process, and read-out by a non-destructive probe [1–3]. The prerequisite for possible applications is a profound knowledge of the magnetic properties of these building blocks (atoms) in their environment. Although no direct application is in sight, magnetic atoms and molecules on superconductors have drawn a lot of attention over the last years. This is due to their rich physics of interactions on the single atom scale as well as in magnetically coupled nanostructures [4].

Superconductivity and magnetism are two extremely interesting properties of materials but cannot coexist in a material on the macroscopic scale. Superconductors are materials that can conduct current without resistance, i.e., without dissipation and heating of the environment below a material-specific critical temperature [5]. In a type I superconductor, a magnetic field cannot penetrate into the material. The expulsion of magnetic field lines causes a magnet to levitate above a superconductor (Fig 1.1(right panel)). This effect is known as Meissner-Ochsenfeld effect and evidences the perfect diamagnetic state. However, if the magnetic field is too strong, the field lines cannot be expelled anymore and superconductivity breaks down ((Fig 1.1(left panel)). Hence, each type I superconductor has a specific critical field, above which superconductivity is destroyed [6].

The microscopic picture of superconductivity ascribes the phenomenon to pairing of two electrons with opposite spins via a phonon mediated process. These so-called Cooper pairs are responsible for conducting current without any electrical resistance due to their bosonic character [7, 8]. In contrast, magnetism is a result of the alignment of electrons with fermionic character in a way to produce a

ferromagnetic/antiferromagnetic state [9]. In a simplified picture, the formation of Cooper pairs can be disturbed by a magnetic field, which tends to align the anti-parallel spins, eventually leading to the suppression of superconductivity. On the nanoscale, the magnetic moment of an atom can perturb the Cooper pairs by exerting an opposed force on the two electrons. This exchange interaction effectively leads to a scattering potential [4]. The fingerprint of such spin exchange interactions are so-called Yu-Shiba-Rosinov (Shiba) bound states inside the superconducting gap [10–12]. These can be accessed by tunneling spectroscopy as a pair of resonances symmetric to the Fermi level. At the same time, the scattering potential also tends to invoke many-body correlations known as the Kondo effect. The formation of a Kondo singlet competes with the singlet state of the superconductor. If the exchange scattering is small, i.e., $k_{\mathrm{B}}\mathrm{T}_{\mathrm{K}} < \Delta$, the ground state is the superconducting state with a free spin on top. When $k_{\mathrm{B}}\mathrm{T}_{\mathrm{K}} > \Delta$, the system undergoes a quantum phase transition with the new ground state being the singlet Kondo state, in which the adsorbate spin is screened.

The competing interactions have been studied theoretically for many decades [13]. Experimental access to these mechanisms has been rather limited, because one needs direct access to individual magnetic moments and their environments.

The innovation of scanning tunneling spectroscopy provides the opportunity to locally study the effect of the magnetic atoms on superconducting substrates [14]. The first magnetic fingerprints of the spin exchange scattering of magnetic atoms (Mn, Gd) on superconducting Nb(110) has been detected as a Shiba state inside the superconducting gap in 1997 [14]. Almost ten years later, a second STM experiment that investigated single manganese atoms on superconducting layers of Pb showed multiple Shiba states [15]. The first experiment on magnetic molecules (manganese phthalocyanine) unequivocally demonstrated that small differences in the adsorption site yields different energies of the Shiba states, thus signifying different magnetic coupling strengths. The variation of coupling strength left same molecules in the Kondo-screened ground state and others in the free spin ground state [16]. The same experiment at lower temperature, revealed the influence of magnetic anisotropy, which arises from spin-orbit coupling due to the ligand field, in splitting of the Shiba state into a peak triplet [17]. Another class of metal-organic molecules, namely iron-octaethylporphyrin (Fe-OEP) on Pb(111), exhibited a different magnetic fingerprint: instead of Shiba states, spin excitations are observed. This magnetic fingerprint mainly originated from the excitation of Fe spin states that are split due to the existence of magnetic anisotropy in the absence of scattering effects of Cooper pairs [18]. However, the superconducting gap provided a long lifetime of the spin excitation, resulting in the detection of the next spin excitation [19]. Up to now, no general attempts have been made to obtain all different magnetic fingerprints in one experiment. Additionally, the manipulation of these states in a magnetic field has not been fully explained.

Thus, in my research, I focused on obtaining different metal organic nanostructures on superconducting Pb. For obtaining ordered metal organic nanostructures and also governing the function of magnetic atoms in a desirable way, I employed two main strategies: (1) The first included the self-assembly of metal organic

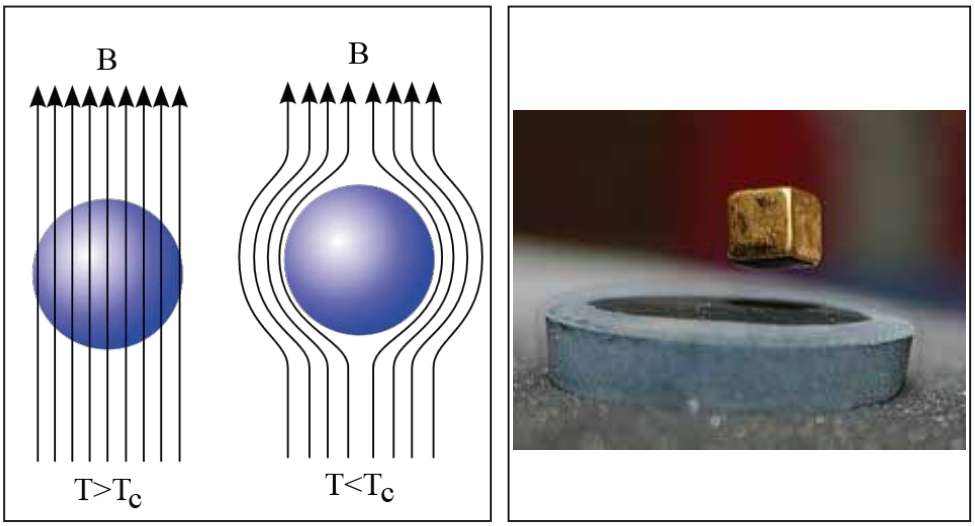

Figure 1.1: a) A superconducting object (violet blue) is exposed to an external magnetic field B. At temperatures smaller than the critical temperature $T < T_C$, the superconductor repels the magnetic field. However, at temperatures higher than the critical temperature, the magnetic field flows through the object. b) A magnet levitates over a superconductor. Images taken from [20].

networks in-situ on a Pb(111) surface. Choosing organic acceptor molecules with a high electron affinity sustains bond formation to a metal atom. Substituting the metal atoms by others with different spin state can produce a wide category of metal-organic networks with different functionality and properties. (2) The second approach was based on self-assembly of embedded magnetic atoms in organic molecules, for instance, metal organic complexes. Choosing flexible organic ligands can provide a key-tool to manipulate the coupling of the central metal to the substrate in addition to the possibility of exchanging the central atom. Our main tool is a low temperature scanning tunneling microscope (LT-STM), which offers the unique possibility to image, probe and manipulate the atomic and molecular systems with atomic spatial resolution.

The goal of this thesis is to understand the universal spin exchange interactions of magnetic impurities with the Cooper pairs. Additionally, we want to investigate the metal-organic nanostructures with different magnetic properties and manipulate their interactions strengths in a controlled way. The exact role of the environment of the metal atom is investigated. The tip of the STM at different distances can be used as an external force to manipulate the magnetic properties. By using different metal atoms, we tune the spin state and study the effect of this change in their magnetic properties. Additionally, by substituting the organic ligand we manipulate the hybridization between the magnetic atoms and the underlying substrate. Investigating the effect of these manipulations of structure, electronic and magnetic properties of the magnetic nanostructure in detail can provide a way to design the systems whose properties can be changed

according to the demands.

The thesis is ordered as follows:

We first introduce the fundamental basis of the STM in addition to its capability of spectroscopy (chapter 2).

In the third chapter we explain the theoretical background of superconductivity as well as the spectroscopic signals of the superconductor-vacuum-superconductor tunneling junction. Furthermore, the magnetism of single atoms is explained in an isotropic and anisotropic environment. Finally, the fingerprints of the magnetic interaction between a magnetic atom and the underlying substrate in the normal and superconducting states are described.

In the forth chapter, we explain the growth of metal-organic networks on superconducting Pb(111). Here, different metal atoms have been linked via organic acceptor molecules. Among all different successfully produced metal-organic networks from different metal atoms, one Fe-organic network has shown signs of magnetic interaction with the underlying substrate.

The last chapter is dedicated to the investigation of magnetic atoms embedded in a molecular complex, a so-called metal-porphyrin. Iron-tetrapyridine-porphyrin (Fe-TPyP) molecules are grown on a Pb(111) substrate and form self-assembled molecular islands. The molecules exhibit different magnetic fingerprints depending on their environment. These site specific properties are studied in detail to obtain a better understanding of the molecule-substrate interactions. We replace the central metal to manganese that has a different spin state to study the effect of this change to the assembly, conformation, electronic and magnetic properties of the Mn-TPyP molecule. Furthermore, to manipulate the interaction between the Mn atom and the Pb substrate, we have substituted the pyridine end group to phenyl-tert- butyl end groups that have more bulky character.

Chapter 2

Fundamentals of scanning tunneling microscopy

2.1 Scanning tunneling microscopy and spectroscopy

When it comes to investigate physical properties at the atomic scale in real space, scanning tunneling microscopy (STM), invented in 1982 by Binning and Rohrer, is a versatile apparatus [21]. They have shown that, STM can provide topographic images of conducting surfaces with atomic resolution [22]. In 1991, Donald Eigler successfully revealed the atomic manipulation capability of STM [23]. Additionally, scanning tunneling spectroscopy can provide information about the electronic and magnetic properties of materials down to the atomic scale thanks to the spectroscopic ability of STM [24].

In this chapter, I describe the general principle of scanning tunneling microscopy and spectroscopy. The first part is dedicated to the working principle of STM followed by the theoretical description of the tunneling current and its relation to the operation of STM. Then, the theory of the elastic and inelastic scanning tunneling spectroscopy is introduced. In the last part, I characterize the experimental setup and sample preparation.

2.1.1 Fundamentals of STM

The quantum mechanical tunneling effect is the basis of the scanning tunneling microscope [25]. A tunneling current arises from the penetration of the electron wave function through a small potential barrier with a certain probability. In STM, the electron tunnels from an atomically terminated metallic tip to a conducting surface (and vice versa). The tip and the sample are separated by a vacuum barrier of typically a few Å, which acts as a potential barrier. Fig.2.1(a) shows a sketch of a STM junction, where an electron from the tip with the wave function Ψ_{ele}, depicted here as a red sinusoidal wave, decays exponentially

while tunneling through a potential barrier ($\mathrm{E_{vac}}$) into the sample.

In absence of an applied bias to the tip or sample, the electrons can tunnel with equal probability in both directions between tip and the sample, which gives rise to a zero net tunneling current. By applying a small bias voltage, a finite tunneling current flows through the tunneling barrier between the tip and the sample.

Fig.2.1(b) shows a drawing of an STM setup, the tunneling current is measured between the tip and a sample at the distance of z under an applied bias. To control the tip-sample distance, we take advantage of the strong dependence of the tunneling current on the tip-sample distance z. Typically, by changing the tip-sample distance by 1Å, the corresponding tunneling current changes by one order of magnitude [26]. To get a topographic image, the tip is attached to a piezoelectric element, allowing to precisely move the tip in space with sub-Å precision. There are two main operational modes which are schematically shown in Fig.2.1(c,d). In the *constant-current* mode, Fig.2.1(c), the tip scans over the surface such that a feedback loop adjusts the tip-sample distance z, to keep the tunneling current constant at each scanning point. The feedback values as a function of tip position then gives the topographic image of the sample. The *constant-height* mode, Fig.2.1(d), is based on keeping the tip-sample distance constant while recording the tunneling current. The variation of the tunneling current is used to obtain an image of the sample surface. However, in this mode we need to be sure to have a flat surface to avoid unintentional tip sample contact [27].

2.1.2 Theory of scanning tunneling microscopy

To theoretically describe the working principle of STM, we employ the Tersoff-Hamann model. In this model, the tunneling current between a spherical tip apex of known radius, R, and a flat surface in a certain distance, d, under the applied bias, $\mathrm{V_{bias}}$ is calculated. Under such circumstances, the Fermi levels of tip and sample are shifted by $e\mathrm{V_{bias}}$ with respect to each other (see Fig.2.2(a,b)). Fig.2.2(a) shows a schematic drawing of a positive sample bias, such that electrons tunnel from the occupied states of the tip to the unoccupied states of the sample. Hence, by applying a negative sample bias, electrons tunnel from the occupied states of the sample to the unoccupied states of the tip. The total tunneling current, I, is a sum of all tunneling events across the tunneling barrier shown as the arrows in Fig.2.2(a,b). In first order perturbation, the tunneling current is obtained by the expression developed by Bardeen [7, 8]

$$I = \frac{2\pi e}{\hbar} \sum_{\mu,\nu} f(E_\mu)\left[1 - f(E_\nu + e\mathrm{V_{bias}})\right] |M_{\mu\nu}|^2 \delta(E_\mu - E_\nu), \tag{2.1}$$

with $\mathrm{V_{bias}}$ and $f(E)$ being the applied voltage and the Fermi function, respectively. $M_{\mu\nu}$ is the tunneling matrix element, which is ascribed to the transmission probability between tip and sample states, ψ_μ and ψ_ν, with their corresponding energies of E_μ and E_ν, respectively. By diagonalization of the

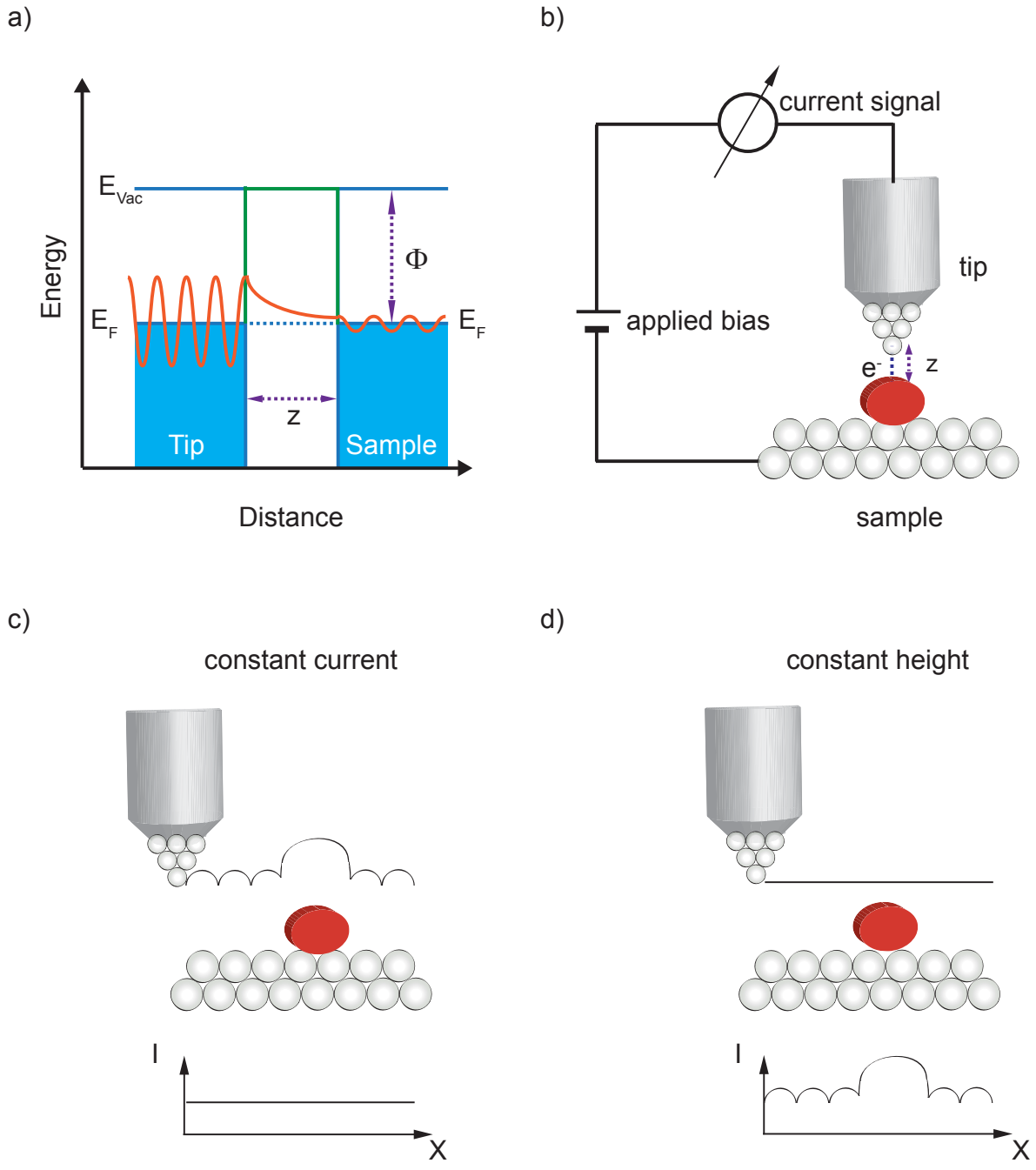

Figure 2.1: Schematic representations of a) the tunneling current for a metal (tip)-insulator (vacuum)-metal (sample) junction. Electrons tunnel from the tip with a certain probability to the sample at distance of z due to their wavelike character (red line). b) STM working principle. An atomically terminated metal tip is brought close (z) to the sample. By applying a bias voltage, a net tunneling current flows between tip and the sample. c) Constant current topographic mode. d) Constant height topographic mode.

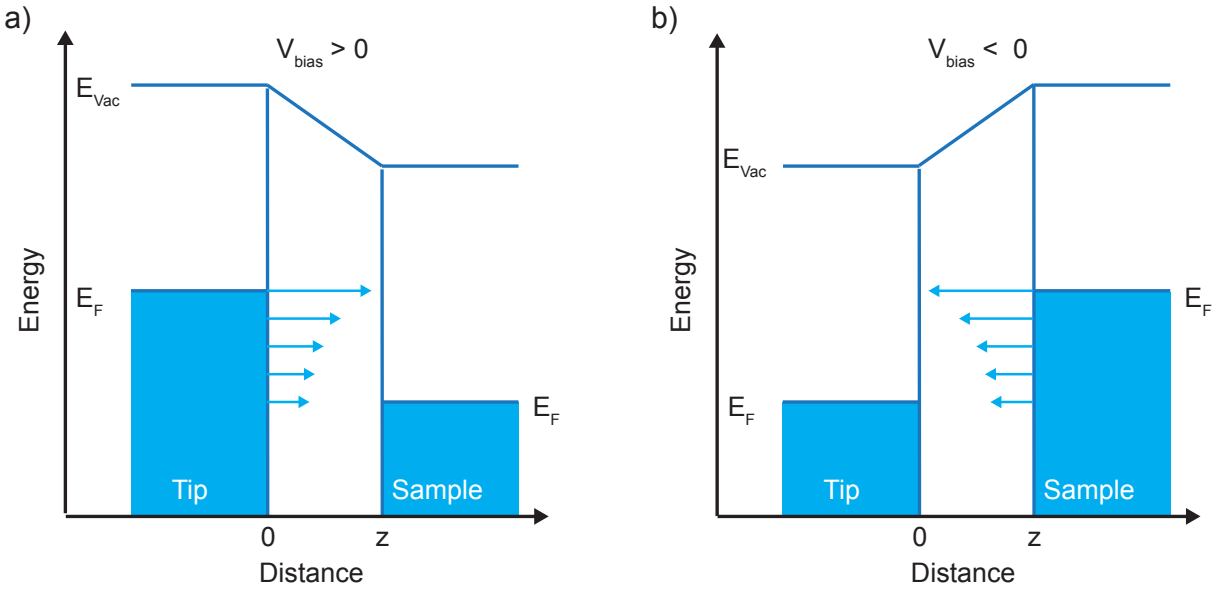

Figure 2.2: Schematic drawing of the tunneling process for a) positive sample bias. Electrons tunnel from occupied states of the tip to the unoccupied states of the sample. All states from the Fermi level E_F to E_F+$\mathrm{V_{bias}}$, shown as blue arrows, are contributing to the tunneling current. Electrons from states at higher energy values have a higher tunneling probability due to a lower potential barrier (longer arrows). b) Negative sample bias. Electrons tunnel from occupied states of the sample to unoccupied states of the tip.

tunneling matrix we obtain for small bias voltages:

$$|M_{\mu\nu}|^2 \propto exp\left\{-2z\frac{\sqrt{2m}}{\hbar}\sqrt{\Phi+\frac{eV}{2}-E}\right\}, \tag{2.2}$$

where Φ is the average work function of tip and sample. To simplify Eq.2.1, the sum over all the states is replaced by the integration over all energies of the states. Under the assumption of small bias voltages and low temperatures, the Fermi function becomes a step function and the tunneling current can be rewritten as

$$I = \frac{2\pi e}{\hbar}\int_{E_\mathrm{F}}^{E_\mathrm{F}+e\mathrm{V_{bias}}} dE\rho_\mathrm{t}(E-e\mathrm{V_{bias}})\rho_\mathrm{s}(E)|M_{\mu\nu}|^2. \tag{2.3}$$

Here, $\rho_\mathrm{t}(E)$ and $\rho_\mathrm{s}(E)$ are the density of states (DOS) of tip and sample at this energy, respectively. By assuming a flat DOS of the tip, the main factors affecting the tunneling current are the tunneling matrix element and the DOS of the sample. To a certain extent, such a simple expression describes very well the experimental results.

In case of a more complex tip apex and inelastic tunneling contributions, this approximation is not valid anymore. In this case, higher order tunneling processes and more complex assumptions need to be considered in order to interpret the experimental findings.

2.1.3 Theory of scanning tunneling spectroscopy

Besides the imaging capability of STM, we can collect information about the electronic and magnetic properties of the sample by means of scanning tunneling spectroscopy (STS). We have shown that the tunneling current depends on the density of states of the tip and sample, as well as the tunneling matrix. By taking the derivative of the tunneling current with respect to the applied bias we obtain:

$$\begin{aligned}\frac{dI}{dV} &\propto \rho_t(E_F)\rho_s(E_F + e\mathrm{V_{bias}})|M_{\mu\nu}|^2 \\ &+ \int_{E_\mathrm{F}}^{E_\mathrm{F}+e\mathrm{V_{bias}}} dE\rho_t(E - e\mathrm{V_{bias}})\rho_s(E)\frac{\mathrm{d}|M_{\mu\nu}|^2}{\mathrm{d}E} \\ &+ \int_{E_\mathrm{F}}^{E_\mathrm{F}+e\mathrm{V_{bias}}} dE\rho_s(E)\frac{\mathrm{d}\rho_t(E)}{\mathrm{d}E}|M_{\mu\nu}|^2.\end{aligned} \tag{2.4}$$

Under the assumption of small bias voltages, we assume the matrix element to be constant, thus the second term becomes zero. Additionally, we assume that the DOS of the tip is fairly independent of applied biases, which leads to the vanishing of the third term of Eq.2.4. Therefore, Eq.2.4 is simplified and can be rewritten as:

$$\frac{dI}{dV} \propto \rho_s(E_\mathrm{F} + e\mathrm{V_{bias}}). \tag{2.5}$$

Technically, in scanning tunneling spectroscopy we record the differential conductance (dI/dV) signal. In the differential conductance, we consider three main codependent parameters: I, $\mathrm{V_{bias}}$ and z. In spectroscopy measurements, we keep one of the parameters constant and record the dI/dV, which depends on the other two, at different applied biases. There are two main operation spectroscopy modes: In the constant height operational mode ($\mathrm{I} - \mathrm{V_{bias}}$), which is the most widely used spectroscopic method, the tip is placed at the desired place, the feedback is disabled and the dI/dV is recorded at each bias point. The dI/dV signals are proportional to the DOS of the occupied and unoccupied states of the sample at their corresponding negative and positive sample bias, respectively (see in Fig.2.3(a)). In the other operational mode, the constant current mode ($\mathrm{I} - Z$), the tunneling current is held constant by means of the feedback loop while simultaneously sweeping the bias voltage and recording the dI/dV signal. This mode is extremely useful when high biases are applied (up to 10 eV) because it minimizes the effect of the electric field as well as large tunneling current between tip and sample on the adsorbate [28]. In this operational mode, ($\mathrm{I} - Z$), due to the variation of z, the tunneling matrix changes, which slightly shifts the energy of the recorded adsorbate states [28].

Technically, the STM setup and consequently the measurements can be affected by the existence of external mechanical and electrical noises. The outcome of such an effect will be seen as a decrease of the so-called signal-to-noise ration in spectroscopy. In order to improve the signal-to-noise ratio, we take advantage of the lock-in amplifier technique. By using the lock-in amplifier, we are able to directly record the dI/dV signal. The working principle of a lock-in amplifier is based on adding an AC voltage $V_\mathrm{mod}(t) = V_\mathrm{mod}\sin(\omega t)$, to the DC applied bias voltage, resulting in a modulated tunneling current. In

the case of small modulation V_{mod}, the modulated tunneling current can be written in the form of a Taylor expansion:

$$I[\mathrm{V_{bias}} + \mathrm{V_{mod}} \sin(\omega \mathrm{t})] \propto I(\mathrm{V_{bias}}) + \frac{\mathrm{d}I}{\mathrm{d}V} V_{\mathrm{mod}} \sin(\omega t) + \mathcal{O}(V_{\mathrm{mod}}^2). \tag{2.6}$$

The first term is attributed to the tunneling current, which is the so-called zero-order component. The second term is the first derivative of the current and is proportional to the DOS of the sample [29].

The principle of elastic and inelastic scanning tunneling spectroscopy is shown in Fig.2.3. In case of elastic tunneling, by applying a positive bias to the sample, an electron travels from the energy window [E_F, E_F+$\mathrm{V_{bias}}$] of the tip to unoccupied states of the adsorbate (e.g. a molecule). The initial and final states of the tunneling electron have the same energy, thus this tunneling is an elastic tunneling event. The recorded tunneling current shows an increase at the energy of the occupied and unoccupied orbitals of the molecule. From the simultaneously recorded dI/dV spectra we obtain the signal that is proportional to the DOS of the molecule (see Fig.2.3(a)).

In addition to the elastic tunneling path, the tunneling electrons can excite degrees of freedom like vibrations and spin excitations by providing the appropriate energy of these excitations (orange wiggled line in Fig.2.3(b)). Since these excitations change the energy of the tunneling electrons, it is an inelastic tunneling event. Inelastic tunneling process can only occur at and above a certain threshold energy $E_{IETS} = \hbar\omega$. This extra tunneling channel can be seen as a kink in the tunneling current (see Fig.2.3(b)). The corresponding dI/dV signal shows a step-like feature at the energy of $\pm\hbar\omega$. The total tunneling current can be written as:

$$I_T = I_{el} + I_{inel}. \tag{2.7}$$

The elastic part has been introduced in Eq.2.1 and is linearly proportional to the applied bias ($e\mathrm{V_{bias}}$). Under the condition that the excitation lifetime is much shorter than the average time between elastic and inelastic tunneling processes [30], the inelastic part is approximately related to the reduced voltage $e\mathrm{V_{bias}} \pm \hbar\omega$. To formulate the inelastic tunneling current, we need to account for all electrons that excite the inelastic excitations traveling from/to the tip to/from the sample:

$$\begin{aligned} I_{inel} \propto \sum_i^N W_i [& \underbrace{\int_{-\infty}^{+\infty} f(E + \hbar\omega_i - e\mathrm{V_{bias}})(1 - f(E))dE}_{t \to s} + \\ & \underbrace{\int_{-\infty}^{+\infty} (1 - f(E - \hbar\omega_i - e\mathrm{V_{bias}}))f(E)dE}_{s \to t}]. \end{aligned} \tag{2.8}$$

W_i stands for the probability to tunnel through any of all inelastic channels. The first and second terms stand for the inelastic tunneling current achieved by tunneling from the tip to the sample and vice-versa, respectively. This integral can be solved analytically:

$$I_{inel} \propto \sum_{i}^{N} W_i [\frac{(\mathrm{V_{bias}} - \hbar\omega_i/e) f^*(e\mathrm{V_{bias}} - \hbar\omega_i)}{f^*(e\mathrm{V_{bias}} - \hbar\omega_i) - 1} + \frac{(\mathrm{V_{bias}} + \hbar\omega_i/e) f^*(-e\mathrm{V_{bias}} - \hbar\omega_i)}{f^*(-e\mathrm{V_{bias}} - \hbar\omega_i) - 1}], \tag{2.9}$$

where $f^*(\epsilon) = exp(\epsilon/k_BT)$ with k_B being the Boltzmann constant [31]. By calculating the first derivative of Eq.2.9 with respect to the applied bias, we obtain:

$$\frac{dI_{inel}}{d\mathrm{V_{bias}}} \propto \sum_{i}^{N} W_i [\frac{f^*(e\mathrm{V_{bias}} - \hbar\omega_i)(f^*(e\mathrm{V_{bias}} - \hbar\omega_i) - 1 - \frac{e\mathrm{V_{bias}} - \hbar\omega_i}{k_BT}}{(f^*(e\mathrm{V_{bias}} - \hbar\omega_i) - 1)^2} + \frac{f^*(-e\mathrm{V_{bias}} - \hbar\omega_i)(f^*(-e\mathrm{V_{bias}} - \hbar\omega_i) - 1 + \frac{e\mathrm{V_{bias}} + \hbar\omega_i}{k_BT}}{(f^*(-e\mathrm{V_{bias}} - \hbar\omega_i) - 1)^2}. \tag{2.10}$$

By simplifying Eq.2.10, we can write the general conductance formula as:

$$\frac{dI_t}{d\mathrm{V_{bias}}} \propto \frac{dI_{el}}{d\mathrm{V_{bias}}} + \sigma_{inel}[f`(-e\mathrm{V_{bias}} + \hbar\omega_i) + f`(e\mathrm{V_{bias}} + \hbar\omega_i)] \tag{2.11}$$

where σ_{inel} is the inelastic conductance and $f`(\epsilon) = (1 + exp(\epsilon/1.46k_BT))^{-1}$ [30, 32]. This results in two energetically symmetric steps in the STS signal (see dI/dV trace in Fig.2.3(b)).

Another spectroscopic accomplishment of the STM is the simultaneous recording of the dI/dV signal at each point of the surface at a certain applied bias voltage $\mathrm{V_{bias}}$ during the recording of a topography image. Therefore, we obtain a so-called dI/dV maps, which contain information on the spatial distribution of the DOS just at one specific energy $e\mathrm{V_{bias}}$ in contrast to the topographic image, which is the sum over all states from the Fermi level (E_F) to $E_F + \mathrm{V_{bias}}$ [33].

2.2 Sample preparation

The sample used in our experiment was Pb(111). Lead (Pb) has a face centered cubic (fcc) crystalline structure and becomes superconducting below 7.2 K . The (111) surface symmetry of Pb is hexagonal with a lattice constant of 3.5Å (see Fig.2.4). In contrast to coinage metals (Cu, Ag, Au) with (111) surface symmetry, Pb(111) exhibits no Shockley-type surface state. Pb(111) is cleaned by successive cycles of Ne^+ ion sputtering at an energy of 900 eV followed by annealing at 430 K to assure its atomically cleanliness. Furthermore, the samples were prepared by sublimation of different adsorbates and pre-cooled before transferring it to the STM. The preparation of different systems will be mentioned in their corresponding chapters.

As we discussed in the previous section, the spectroscopic resolution is restricted to the thermal broadening originating from the measurement temperature. To overcome this resolution limit, we use a

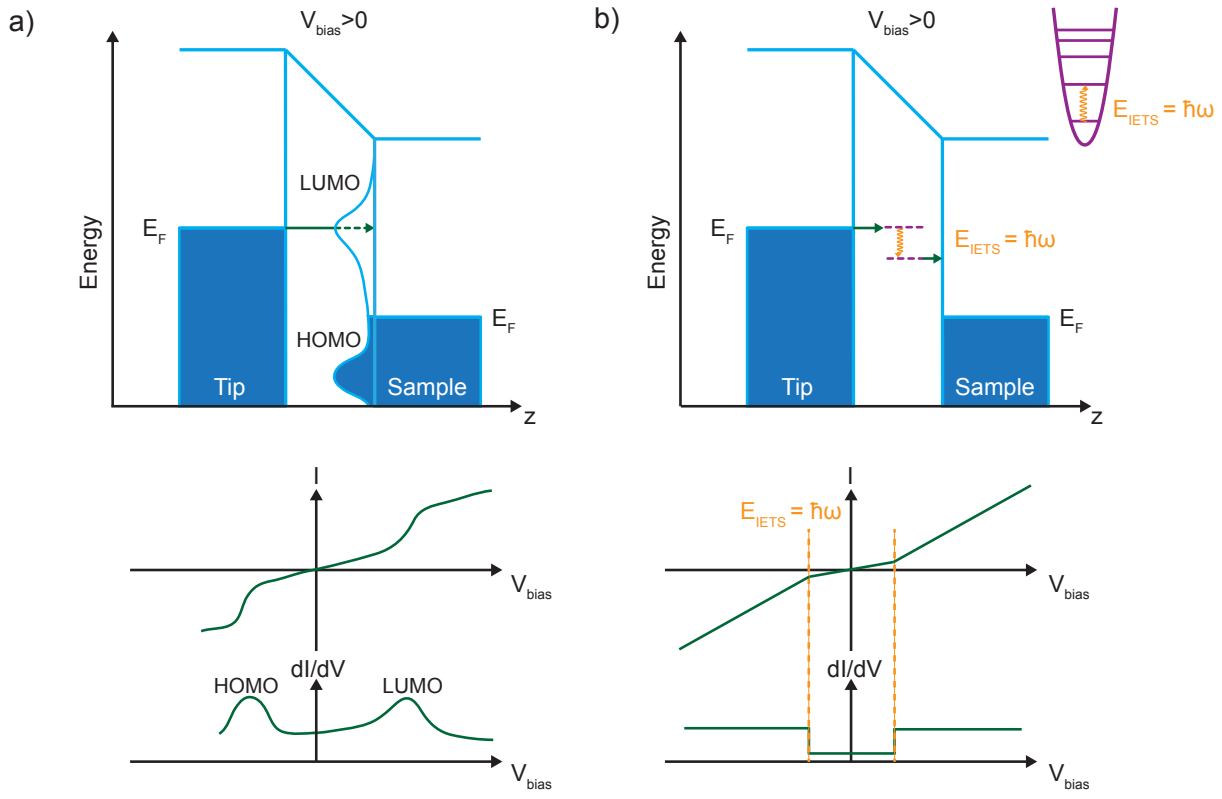

Figure 2.3: a) Schematic drawings of a) elastic tunneling spectroscopy. The Fermi level of the sample is lowered by applying a positive bias to the sample. Electrons tunnel to the unoccupied states of the adsorbate (e.g. molecule) at adequate positive sample bias. This tunneling leads to a nonlinear increase in the current and the corresponding dI/dV spectrum resembles the DOS of the adsorbate (lower panels). b) Inelastic tunneling spectroscopy. The system is excited to another state by transferring energy of $\mathrm{E_{IETS}} = \hbar\omega$ from the tunneling electron to the adsorbate (orange wiggled line). This induces a kink in the current signal and consequently steps in the dI/dV spectra at the energy of $\mathrm{E_{IETS}} = \pm\hbar\omega$.

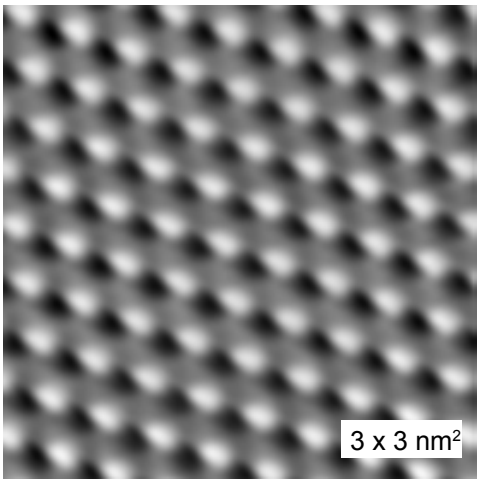

Figure 2.4: Atomic resolution topography of Pb(111). (I= 50 pA, $V_{bias} = 50$ meV)

technical "*trick*" by wisely choosing a tip with a sharp peak in the DOS close to the Fermi level instead of a tip with a flat DOS at E_F. In such case the dI/dV signal will be only proportional to the DOS of the tip. A superconducting tip with a sharp increase of the quasi-particle DOS close to the Fermi level can be used to significantly improve the resolution of spectroscopy [32]. In this case, the spectra measured with the superconducting tip are a convolution of the DOS of the tip and the sample (see Sec.3.1.2). To prepare a superconducting tip, the tip, which is made of tungsten, is covered by a thick layer of superconducting lead. This has been achieved by indentation of the tip deep into the sample while applying a bias voltage of about 100 V.

2.3 Experimental setup

The STM apparatuses used to conduct the measurements consist of two main ultra high vacuum (UHV) chambers, a preparation chamber and a measurement chamber, which can be isolated from each other through a valve (see Fig.2.5(a)). The UHV condition below 5×10^{-10} mbar is maintained by turbo-molecular pumps, ion pumps and titanium sublimation pumps implemented on both chambers. A movable manipulator can be used to transfer the sample between the two chambers.

The preparation chamber is equipped with the necessary tools for preparing atomically clean samples under the desired conditions. The standard equipment such as sputtering facility (Ne gas, sputter gun), annealing stage, mass spectrometer and different types of exchangeable molecular or atomic evaporators are implemented into the preparation chamber.

The STM chamber consists of the STM scanning head in thermal contact with a liquid helium bath cryostat with an equilibrium temperature of 4.2 K. Fig.2.5(b) shows the schematic drawing of the bath

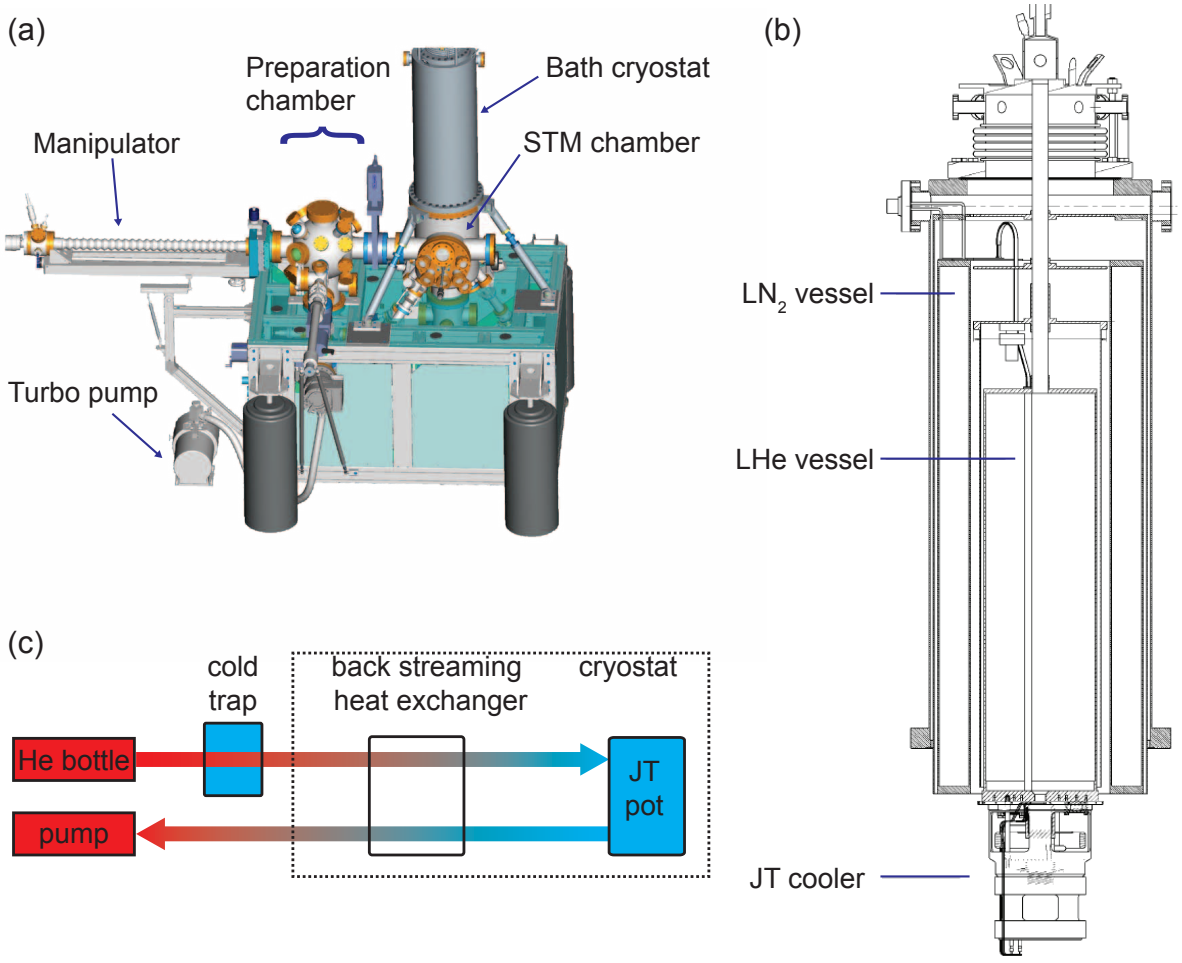

Figure 2.5: (a) Drawing of the *SPECS* JT-STM vacuum chamber hosting the STM as well as a preparation chamber. Components are indicated in the sketch. (b) Design of the SPECS JT-STM bath cryostat with an inner vessel containing liquid helium surrounded by a vessel with liquid nitrogen. Special to this design is the JT cooler, reaching temperatures of 1.1K. (c) Simplified scheme of the JT cycle. Red indicates high temperatures, whereas blue indicates low temperatures. Figures are taken from [34].

cryostat. It consists of the liquid nitrogen cryostat to protect the helium cryostat from thermal radiation of the environment. Furthermore, the final temperature is further reduced to 1.1 K thanks to a cooling system based on the Joule-Thomson effect [34].

The schematic drawing of the Joule-Thomson cooling stage is shown in Fig.2.5(c). Helium gas from a high pressure helium bottle at room temperature, that is placed outside of the cryostat, is pre-cooled with liquid nitrogen to trap its impurities. By pumping the helium gas through a capillary system, the helium gas enters the cryostat through the back streaming heat exchanger and cools down further. Upon entering the JT pot, the helium gas expands adiabatically and cools the system down to 1.1 K.

This cooling mechanism can be understood as following: In case of a non-ideal gas, the system can gain or lose energy during an adiabatic expansion. The amount of the corresponding temperature change depends on the parameters of the system and is quantified by the Joule-Thomson coefficient:

$$\mu_{\mathrm{JT}} = \frac{\partial T}{\partial p} = \frac{V}{C_{\mathrm{p}}}(\alpha T - 1), \tag{2.12}$$

where T is the temperature, P is the pressure, C_P is the heat capacity and V is the volume of the gas. However, the parameter α defines the heating/cooling expansion of the system, which is $\alpha > 1/T$ in the case of cooling the system [35].

An external magnetic field is an essentiality of investigating magnetic systems. Our JT-STM is equipped with a superconducting split-coil magnet, which is arranged according to the setup of a pair of Helmholtz coils. In this arrangement, the two coils are separated by a distance d equal to their radius. This results in a homogeneous magnetic field in the center between the coils, where the sample and tip are positioned. The Biot-Savart law describes this magnetic field:

$$B(R/2) = \left(\frac{8}{5\sqrt{5}}\right)\frac{\mu_0 n I}{R}. \tag{2.13}$$

Here, μ_0 stands for the vacuum permeability. R and n are the radius of the coils and the number of windings of the coils, respectively. At a current of approximately 20 A, in our setup, we can achieve a magnetic field of ± 3 T perpendicular to the sample surface.

Chapter 3

Fundamentals of superconductivity and magnetism

Single magnetic atoms and molecules are promising candidates to play a major role in future information technology [1, 36]. Their local magnetic moments, together with their ability to form nanostructures by self-assembly provide an interesting toolkit for designing circuits and devices for information processing and storage. For practical purposes, the individual building blocks are typically grown on templates, e.g., on semiconductors, metals, etc [37].

An interesting host material are superconductors, which conduct current with zero resistance [7, 8]. Superconductivity and magnetism have an antagonistic relationship due to their nature. Superconductivity arises from the bonding between two electrons with opposite spin, the so-called Cooper pairs. On the contrary, the magnetism originates from the alignment of electrons with same spin. Therefore, it is crucial to understand the precise principles that govern the interplay of superconductivity and magnetism at the atomic scale. One promising approach lies in the combination of adsorption of single magnetic impurities on superconductors. In this case, the spin of a magnetic impurity can interact with the Cooper pairs of the underlying superconducting substrate and create a state, which is known as Yu-Shiba-Rusinov (YSR) or simply Shiba state [10–12] inside the superconducting gap [11, 16, 17, 38, 39]. The fingerprint of a Shiba state is a pair of resonances in the superconducting density of state and can be measured by means of scanning tunneling spectroscopy. For understanding and tuning the magnetic state of single atoms on a superconductor, we first need to understand the basics of superconductivity and atomic magnetism.

In this chapter, we will discuss the theory of superconductivity and explain the spectroscopic signals obtained in measurements with a superconducting tip on a superconducting sample. Additionally, the basics of paramagnetic atoms and molecules will be explained as well as the interaction of magnetic impurities with normal and superconducting substrates, along with their corresponding spectroscopic characteristics.

3.1 Superconductivity

In 1911, Heike Kammerlingh Onnes discovered superconductivity in mercury at 4.2 K, the temperature of boiling helium. He was awarded the Nobel prize in 1913, and today many technical applications rely on his discovery [40, 41]. Superconductivity is a state of matter in which, below a critical temperature, currents flow without any resistance. The question of the microscopic origin of this new state of matter remained unsolved until in 1958 the outstanding theory of Bardeen, Cooper and Schrieffer (short BCS theory) was formulated. In the following, we briefly introduce the BCS theory for conventional superconductors.

3.1.1 Bardeen-Cooper-Schrieffer theory of superconductivity

Conduction electrons in a normal metal can be approximated by periodic waves with a free electron dispersion relation. The electrons are interacting via an effectively reduced Coulomb repulsion due to the screening of their charges by the ions of the crystal lattice. By reducing the temperature below the transition temperature, the metal can become superconducting. Electrons near the Fermi energy can be coupled to each other via a phonon mediated interaction. A simplified picture of such an interaction is shown in Fig.3.1(a). An electron e_1 travels through the lattice of a material and attracts the positively charged ions, displacing them slightly. This displacement gives rise to a local positively charged region along the path of e_1 (indicated by the red sphere in Fig.3.1(a)). Considering the high velocity of the electron in comparison with the ions in the lattice, the electron can travel to far distances while the lattice displacement slowly decays. During that time, a second electron, e_2, can reach the region with the displaced ions and be attracted to the local positive charge. As a result, these two electrons will effectively attract each other. The Feynman diagram of such a phonon-mediated attraction is presented in Fig.3.1(b). The two electrons with opposite spin and momentum $e_1(k,\sigma)$, $e_2(k',\sigma')$ are represented by straight arrows. The first electron e_1 interacts with the lattice such that it creates a phonon of momentum q (wiggled purple line) and its momentum becomes $k-q$. The second electron $e_2(k',\sigma')$ absorbs the emitted phonon, causing the change of its momentum to $k'+q$. These two electrons with opposite spin and momentum are referred to as a Cooper pair [7]. Therefore, the total spin of a Cooper pair is zero and it can be treated as a boson. Thus, all Cooper pairs condense in the same quantum state.

The Bardeen-Cooper-Schrieffer theory of superconductivity describes these processes by a microscopic model. One assumes that within a small energy window around the Fermi level of $\hbar\omega_D$, where ω_D is the Debye frequency, the electrons in the Cooper pairs are exposed to an effective attractive potential $V_{kk'}$. The system can be described by the following Hamiltonian [7, 8]:

$$H_{\mathrm{BCS}} = \sum_{k\sigma} \varepsilon_k c^\dagger_{k\sigma} c_{k\sigma} + \frac{1}{N}\sum_{k,k'} V_{kk'} c^\dagger_{k\uparrow} c^\dagger_{-k\downarrow} c_{-k'\downarrow} c_{k'\uparrow}. \tag{3.1}$$

Here $c^\dagger_{k\sigma}$ and $c_{k\sigma}$ are the electron creation and annihilation operators, respectively. The energy of the

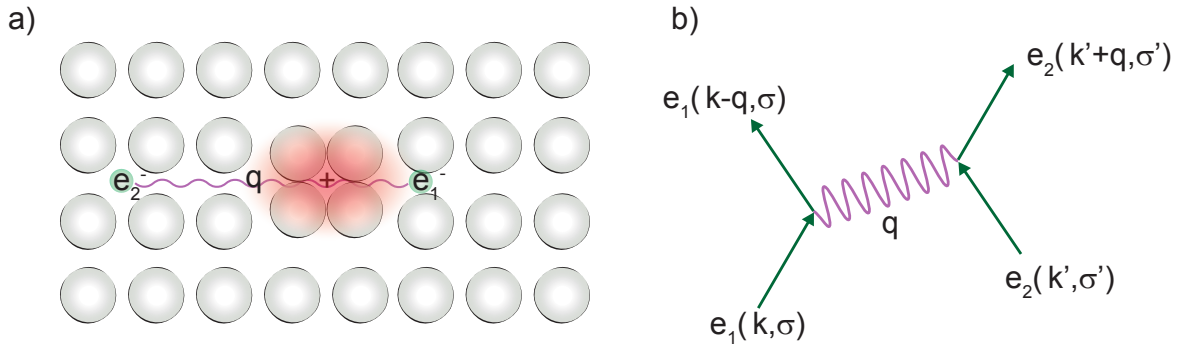

Figure 3.1: a) Illustration of the phonon-mediated creation of a Cooper pair. Lattice ions are represented as silvery balls. The electrons of a Cooper pair are shown by green balls. The phonon that mediates the pairing of these two electrons is shown by the red wiggled line. b) Feynman diagram of the Cooper pair formation. The arrows and wiggled line stand for the interacting electrons and the phonon, respectively. Time evolves from bottom to top.

electrons is represented by ε_k (assuming the chemical potential μ, which corresponds to E_F in equilibrium, is set to zero). Considering the mean field approximation of $c^\dagger_{k\sigma}$ and $c_{k\sigma}$ operators, which replaces the total field of all particles acting on a single particle with the mean field of all total particles (N), we can rewrite the Eq.3.1 as

$$H_{\mathrm{BCS}} = \sum_{k\sigma} \varepsilon_k c^\dagger_{k\sigma} c_{k\sigma} + \frac{1}{N} \sum_{k,k'} V_{kk'} (\langle c^\dagger_{k\uparrow} c^\dagger_{-k\downarrow} \rangle c_{-k'\downarrow} c_{k'\uparrow} + c^\dagger_{k\uparrow} c^\dagger_{-k\downarrow} \langle c_{-k'\downarrow} c_{k'\uparrow} \rangle - \langle c^\dagger_{k\uparrow} c^\dagger_{-k\downarrow} \rangle \langle c_{-k'\downarrow} c_{k'\uparrow} \rangle). \tag{3.2}$$

Furthermore, we introduce a pairing potential, also known as the superconducting order parameter Δ_k, which is equal to half of the energy to break a Cooper pair [5]:

$$\Delta_k = -\frac{1}{N} \sum_{k'} V_{kk'} \langle c^\dagger_{k\uparrow} c^\dagger_{-k\downarrow} \rangle. \tag{3.3}$$

A Bogoliubov transformation is used by Bardeen, Cooper and Schrieffer to diagonalize the above Hamiltonian. It introduces two new fermionic operators $\gamma_{k\uparrow}$ and $\gamma_{-k\downarrow}$, which are quasi-particle operators that consist of electron and hole components. These operators are related to the electron creation and annihilation operators as [42]:

$$\begin{pmatrix} \gamma_{k\uparrow} \\ \gamma^\dagger_{-k\downarrow} \end{pmatrix} = \begin{pmatrix} u_k & -v_k \\ v_k & u_k \end{pmatrix} \begin{pmatrix} c_{k\uparrow} \\ c^\dagger_{-k\downarrow} \end{pmatrix}. \tag{3.4}$$

Because of their fermionic nature, the $\gamma_{k\uparrow}$ and $\gamma_{-k\downarrow}$ operators obey the anticommutation. Therefore, u^2 and v^2, which are the expectation values of filled and empty Cooper pairs, fulfill the relation $u^2 + v^2 = 1$ [42]. Finally, the Hamiltonian of Eq. 3.1 becomes:

$$H_{\mathrm{BCS}} = \sum_{k\sigma} [E_k \gamma^{\dagger}_{k\sigma} \gamma_{k\sigma} + (\varepsilon_k + \Delta \langle c^{\dagger}_{k\uparrow} c^{\dagger}_{-k\downarrow} \rangle)]. \tag{3.5}$$

Here, $\mathrm{E}_k = \sqrt{\varepsilon_k^2 + |\Delta_k|^2}$ is the quasi-particle excitation energy and has a minimum value of the order parameter Δ_k. In case of a conventional superconductor, the density of states of the superconductor can be expressed as:

$$\rho_{\mathrm{S}} \propto \frac{\mathrm{E}}{\sqrt{\mathrm{E}^2 - \Delta^2}}. \tag{3.6}$$

This indicates that the density of states at energies smaller than Δ is zero. The density of states at Δ is a very sharp resonance that corresponds to the condensation of quasiparticles.

3.1.2 Scanning tunneling spectroscopy on superconductors

In our experiment we perform scanning tunneling spectroscopy. This probes the single particle density of states of the material. The density of states of a superconductor can be written in terms of the density of state in the normal states as follows:

$$\rho_{\mathrm{S}} = \begin{cases} \rho_0 \dfrac{E}{\sqrt{E^2 - \Delta^2}} & \text{for } |E| > \Delta \\ 0 & \text{for } |E| < \Delta, \end{cases} \tag{3.7}$$

where ρ_{S} and ρ_0 are the density of states in the superconducting and normal state, respectively.

Fig.3.2(a) shows the density of states given by Eq.3.7. Within the superconducting gap at $|E| < \Delta$, there is no single particle density of states. The superconducting gap is enclosed by two singularities at $E = \pm\Delta$, which correspond to the threshold for the excitation of quasi-particles, as described by Eq.3.5. In our experiment also the tip is in a superconducting state. A schematic drawing of such a superconductor-vacuum-superconductor junction is shown in Fig.3.2(b), with a positive sample bias voltage applied. At a bias voltage of 2Δ, the quasi-particles tunnel from occupied states of the superconducting tip to unoccupied states of the superconducting sample (vice versa for negative bias voltages). At energies lower than 2Δ, the tunneling of quasi-particles is forbidden, as there are no states within the superconducting gap. Fig.3.2(c) shows a dI/dV spectrum recorded with a superconducting Pb tip on the superconducting Pb(111) single crystal at 1.1 K. Two sharp quasi-particle peaks can be seen at a bias of $\pm 2\Delta \approx \pm 2.75$ meV. Each of these peaks contains two resonances labeled as Δ_1 and Δ_2, indicated by dashed gray lines. This can be explained by the two band superconductivity of the Pb substrate [43, 44], as each of the two Fermi sheets of Pb gives rise to a distinct gap.

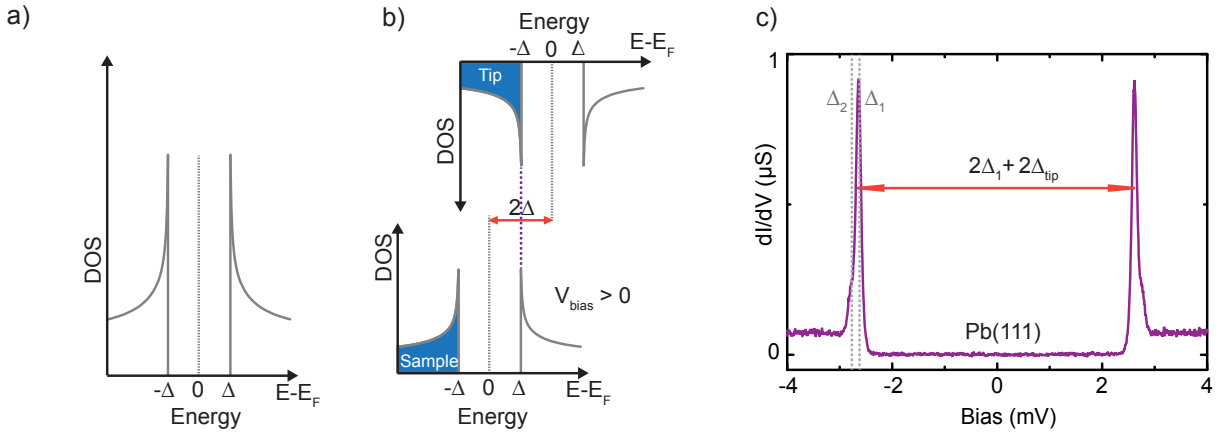

Figure 3.2: a) Density of states of a superconductor around $\mathrm{E_F}$. b) Drawing of a superconductor (tip)-vacuum-superconductor (sample) junction. Positive bias voltage $V_{bias} = 2\Delta$ is applied to the sample, resulting in tunneling of quasiparticles from the tip to the sample. c) dI/dV spectrum on Pb(111) with a superconducting tip at 1.1 K. The two quasi-particle peaks are separated by $2\Delta_1 + 2\Delta_{\mathrm{tip}}$, indicated by the red arrow. Each side of the quasi-particle peak consists of two peaks, Δ_1 and Δ_2, marked with dashed gray lines. The feedback was opened at $V_{\mathrm{bias}} = 5$ meV and $I = 500$ pA with a modulation of $V_{\mathrm{mod}} = 15$ μeV.

3.2 Magnetic impurities on a superconductor

In an atom, magnetism arises from unpaired electrons [45]. The configuration of these electrons in the ground state is determined by Hund's rules [46]. Hund's first rule states that the total spin $|\vec{\mathrm{S}}|$ of the system is maximized due to parallel alignment of the individual spins of the electrons. According to the second rule, those orbitals are occupied first, that lead to a maximization of $|\vec{\mathrm{L}}|$. Moreover, spin-orbit coupling results in the coupling of the total spin momentum $\vec{\mathrm{S}}$ with the total orbital momentum $\vec{\mathrm{L}}$, which add up to a momentum $\vec{\mathrm{J}}$. The magnetic moment of an atom in the gas phase, i.e., isotropic environment, has no preferred magnetic direction. As soon as the atom is placed in an anisotropic environment, e.g., by adsorption on a surface or by embedding to a molecular complex, the rotational symmetry is broken and thus the magnetic moment experiences a preferential orientation. In the following, we discuss the influence of an anisotropic environment on the magnetic moment of an atom adsorbed on a surface or embedded in a large molecule.

3.2.1 Ligand field

To characterize the effect of the local environment on the magnetic moment of an atom we consider a transition metal with partially filled 3d orbitals. Fig.3.3(a) shows the spatial distribution of real combinations of the spherical harmonics of the five 3d orbitals. In an isotropic environment, they are energetically degenerate and their total angular moment L is zero.

By placing atoms around it, with a so-called square planar symmetry, the degeneracy of the 3d orbitals will be lifted due to the Coulomb interaction between the electrons of the central atom and the electrons of the surrounding atoms (see Fig.3.3(b)). Depending on the spatial distribution of the 3d orbitals and their bonding direction to the neighboring atoms, they experience different Coulomb repulsion and thus shift independently in energy. For example, the $d_{x^2-y^2}$ orbital directly points to the neighboring atoms and hence shifts highest in energy. On the contrary, the d_π (d_{xz}, d_{yz}) orbital lies on the lowest level, as they point diagonal to the axis between center and atoms. It is worth mentioning that the occupation of the split levels is competing with Hund's first rule to maximize the total spin, as the energy splitting of the d-levels can be higher than the spin-pairing energy, leading to low-spin molecular complexes.

3.2.2 Magnetic anisotropy

Due to the ligand field, the degeneracy of the d-orbitals is lifted and the new ground state is composed of all degenerate d-orbitals. This new ground state also has zero orbital angular momentum. However, due to the admixture of this orbitals through virtual excitation processes, the atom can retain a finite orbital angular momentum that can couple to the spin and be treated as a perturbation effect. The spin-orbit coupling of the central magnetic atom gives rise to the so-called magnetocrystalline anisotropy and lifts the degeneracy of the different spin projections. Since this splitting requires no external magnetic field, it is called zero field splitting (ZFS) [45]. Considering the relatively small energy of the spin-orbit coupling compared to the ligand field energy, we can treat the spin-orbit coupling as a perturbative effect. Therefore, to describe ZFS we use the spin Hamiltonian approach given by:

$$\hat{H} = DS_z^2 + E\left(S_x^2 - S_y^2\right). \tag{3.8}$$

D and E are the axial and transverse magnetic anisotropy, respectively, and $S_{x,y,z}$ give the spin projection in x, y and z direction [47, 48]. The first term describes the energy splitting of the states with different spin projection along the z-direction, $\mathrm{m_s}$, while the second term expresses the mixing of these states upon further reduction of symmetry.

As an example, Fig.3.3(c) shows the energy levels of a spin-1 system under different conditions: (1) in the presence of no magnetic anisotropy; (2) with axial anisotropy $D > 0$ and the absence of transverse anisotropy $E = 0$; (3) in the presence of axial and transverse anisotropy, $D > 0$ and $E \neq 0$. Without magnetic anisotropy, there is no preferred orientation of the spin, such that all spin projections $\mathrm{m_s} = \pm 1$ and 0 are degenerate. A positive axial anisotropy D lifts the degeneracy of these state, such that $\mathrm{m_s} = 0$ lies lower in energy and becomes the ground state and the $|\pm 1\rangle$ states are higher by an energy D. The positive value of D corresponds to the so-called *hard-axis* anisotropy and favors the state with low spin projection. On the contrary, negative D is called *easy-axis* and favors the state with highest spin

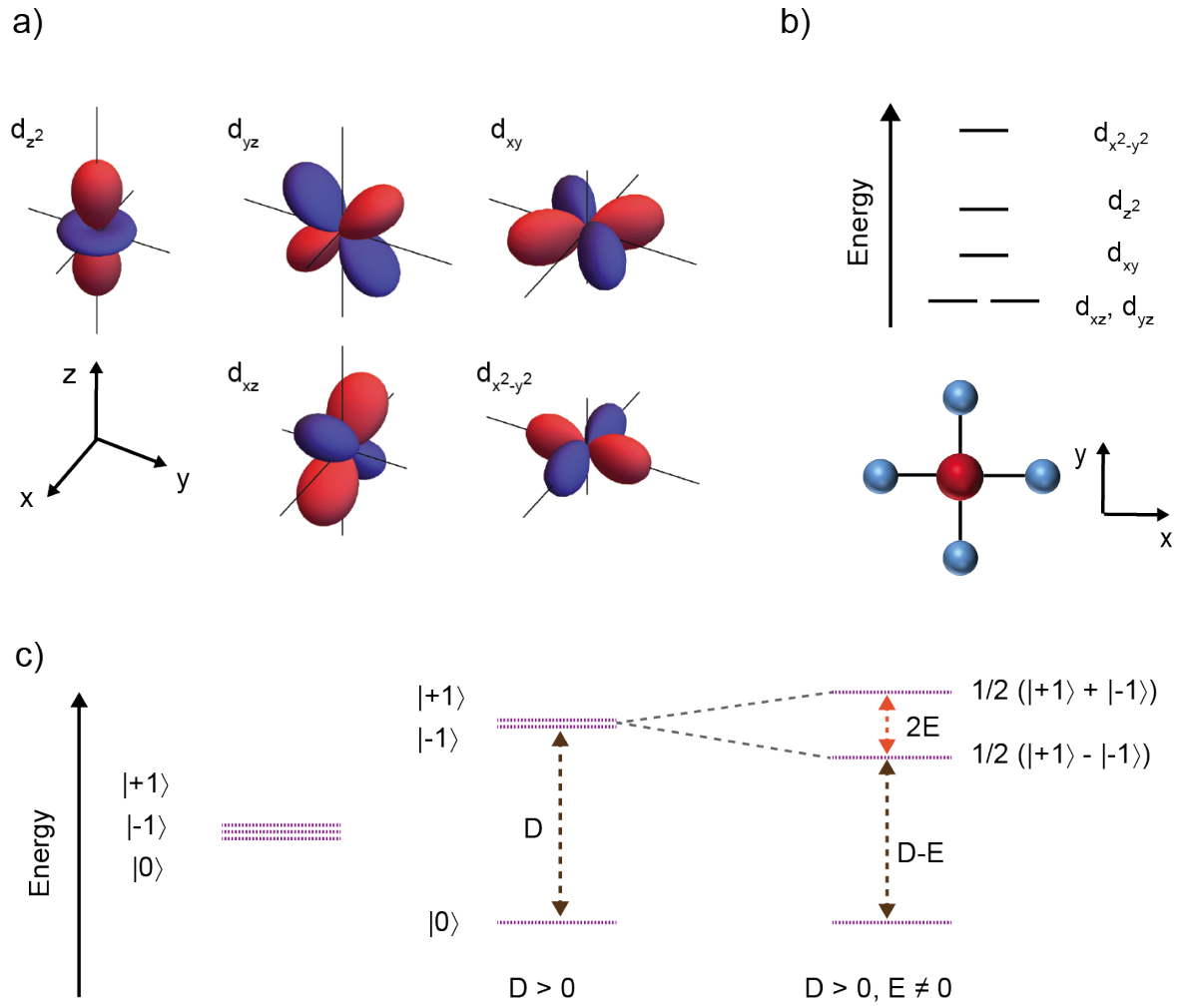

Figure 3.3: a) Real part representation of wavefunctions of the 3d-orbitals. b) Due to the influence of the ligand field, the degeneracy of the d-orbitals is lifted. The central metal atom (red sphere) experiences the square planar ligand field of the neighboring atoms (blue spheres). c) In an isotropic environment all spin projections of a system with S = 1, $m_s = \pm 1$ and 0 are degenerate. The hard axis anisotropy lifts the degeneracy of the spin states such that $|0\rangle$ is the ground state. The transversal anisotropy mixes the $|\pm 1\rangle$ states and produces two new states $|+\rangle = \frac{1}{\sqrt{2}}(|+1\rangle + |-1\rangle)$ and $|-\rangle = \frac{1}{\sqrt{2}}(|+1\rangle - |-1\rangle)$.

projection. Furthermore, the transversal anisotropy E mixes the $|\pm 1\rangle$ states and gives rise to two new states of $|+\rangle = \frac{1}{\sqrt{2}}(|+1\rangle + |-1\rangle)$ and $|-\rangle = \frac{1}{\sqrt{2}}(|+1\rangle - |-1\rangle)$ [47, 49].

To obtain a magnetic atom in such an anisotropic environment, as we described above, one can incorporate a magnetic atom into an organic ligand. This can lift the degeneracy of the spin states of the atom. An additional effect occurs when adsorbing the molecule on a surface. Here, the magnetic moment interacts with the conduction electrons. Furthermore, in the superconducting state, the magnetic moment of the impurity can interact with Cooper pairs. In the following, we will describe the magnetic fingerprint of the impurity adsorbed on normal and superconducting substrates. The resulting many-body phenomena are the Kondo effect and Yu-Shiba-Rusinov states, which will be discussed below.

3.2.3 The Kondo effect

The electrical resistance of a pure metal decreases towards lower temperature, due to a reduction of the electron-phonon interaction, which is known as Matthiessen's[1] rule. However, by cooling a metal which contains paramagnetic impurities below a certain temperature, surprisingly, its electrical resistance increases again [50]. This abnormality could first be explained by Jun Kondo in 1964, nearly three decades after its discovery [51], and is hence called the Kondo effect.

His model is based on scattering of the conduction electrons at the magnetic impurities by spin-spin interaction [51]. At the atomic scale, the Kondo effect has been observed over the last decade in various experiments on single adatoms on surfaces [52, 53], and in quantum dots [54, 55], and more sophisticated systems of coupled Kondo lattices [56–58]. To understand the theory behind the Kondo effect, the so-called Anderson impurity model is introduced, which describes the energy levels of a magnetic impurity coupled to a metal.

Single impurity Anderson model

Anderson established a Hamiltonian that considers a single impurity level (*d* or *f* level of the impurity) and the conduction band of the host metal. Due to hybridization of the orbitals of the impurity with the surface, the orbital is broadened by Γ [59]. Fig.3.4(a) shows a schematic illustration of such a system. The impurity orbital has an energy ε_{d}. To add a second electron with opposite spin, the Coulomb energy U has to be paid. For the Kondo effect to occur, the following conditions have to be fulfilled: $\varepsilon_{\mathrm{d}} < \mathrm{E_F}$; $\varepsilon_{\mathrm{d}} + \mathrm{U} > \mathrm{E_F}$; $\Gamma \ll \mathrm{U}$.

A simplified picture of the spin-spin interaction between the impurity electron and the conduction electrons of the host metal is shown in Fig.3.4. According to the Heisenberg uncertainty principle, $\Delta \mathrm{E} \Delta \mathrm{t} \geq \hbar$ with $\hbar$, being the Planck constant. This implies that for a short period of time the electron in the singly occupied orbital can hop to the host metal (Fig.3.4(b)). Therefore, by means of virtual excitations the impurity level is empty and can be refilled again with an electron from the substrate. In another process,

[1] Augustus Matthiessen, British chemist, 1831-1870

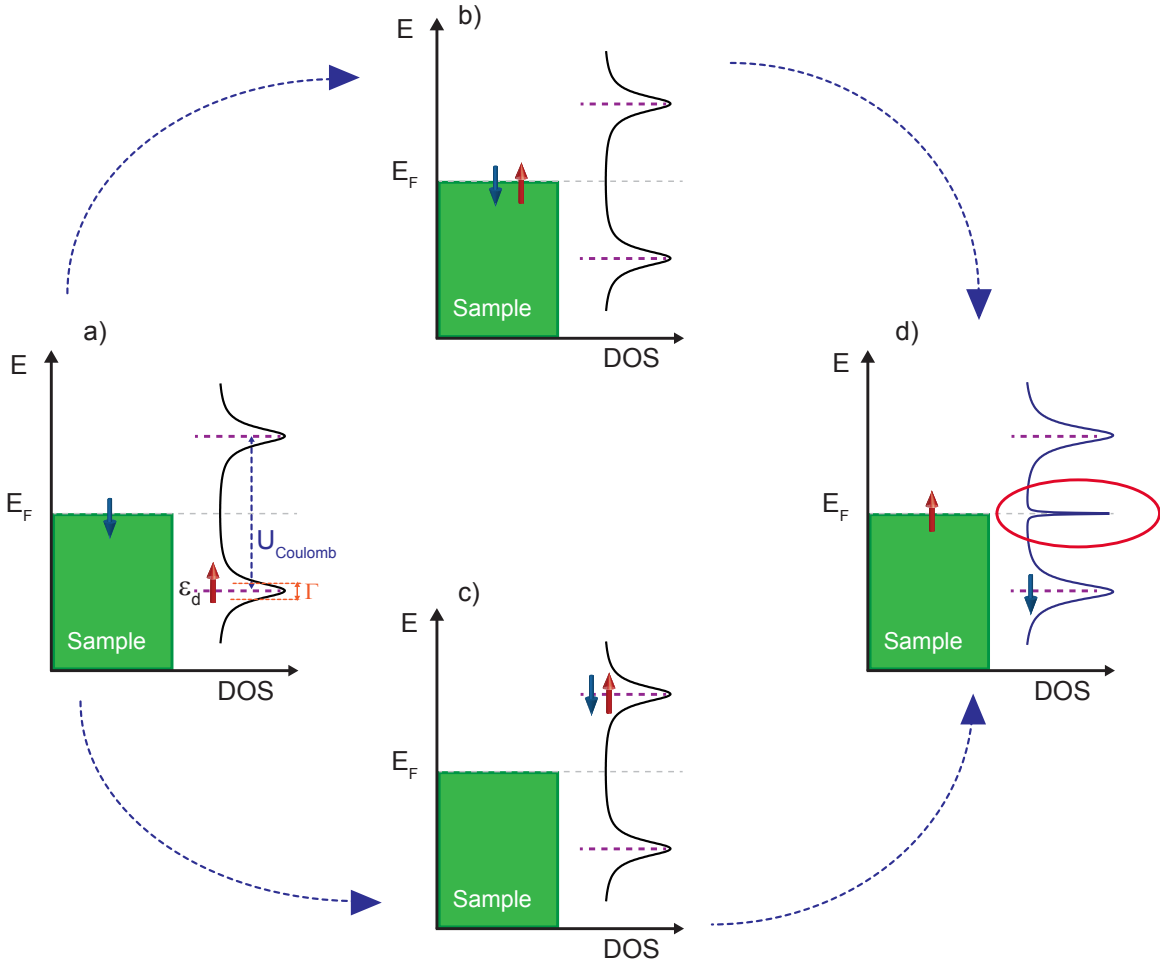

Figure 3.4: a) Scheme of the DOS of a magnetic impurity on a metal. The orbital of the magnetic impurity is occupied by a spin-up electron at an energy ε_d below E_F. Due to the hybridization with the substrate, the impurity orbital has a width of Γ. The doubly occupied orbital is separated by the Coulomb energy U from the singly occupied state and has an energy of $U+\varepsilon_d$. Spin exchange scattering can flip the spin of the impurity electron via two virtual processes: b) by emptying the singly occupied orbital or c) by filling the doubly occupied orbital. In both virtual processes, the conduction electrons from the substrate at the Fermi level are involved. d) The spin exchange scattering results in a many-body state at the Fermi level referred to as Kondo state (highlighted by the red ellipse).

an electron from the substrate can hop onto the impurity, leading to a double occupation for a short period of time (Fig.3.4(c)). Afterwards, the system can relax in two ways: either the spin of the impurity is the same as before the scattering event or it is reversed. In both processes, only electrons with the opposite spin participate in the Kondo effect (Fig.3.4(d)). As a result, the spin exchange scattering of conduction electrons of the magnetic impurity modifies the DOS of the system. A new state, the so-called many body Kondo state appears as a Lorentzian peak at the Fermi energy (highlighted by a red ellipse in Fig.3.4(d)).

Anderson used the following Hamiltonian to describe the Kondo effect [60]:

$$H_A = \sum_{k,\sigma} \varepsilon_k c^\dagger_{k,\sigma} c_{k,\sigma} + \sum_{\sigma} \varepsilon_d n_{d,\sigma} + U\, n_{d,\uparrow} n_{d,\downarrow} + \sum_{k,\sigma} \Big(V_k c^\dagger_{d,\sigma} c_{k,\sigma} + V_k^* c^\dagger_{k,\sigma} c_{d,\sigma} \Big). \tag{3.9}$$

The first term belongs to the host metal electrons with σ being spin $\uparrow$ and $\downarrow$. c_k and $c_k^\dagger$ are electron annihilation and creation operators. The second and third terms describe impurity orbitals that can host at maximum two electrons with opposite spin and that are separated from each other by the Coulomb energy U. The last term considers the spin exchange interaction between the conduction electrons and the electron in the impurity orbital that hybridizes with the substrate, with V_k being the exchange matrix element [60].

The above mentioned spin exchange processes at the impurity site are energy conserving processes. Therefore, only the electrons close to the Fermi level participate in the spin exchange interaction. Additionally, we can use the canonical transformation of the Anderson Hamiltonian (Eq. 3.9) to obtain the so called Kondo Hamiltonian [61]:

$$H_K = \sum_{\sigma} \varepsilon c^\dagger_\sigma c_\sigma + J \overrightarrow{\mathrm{s}} \cdot \overrightarrow{\mathrm{S}_d}. \tag{3.10}$$

Here, $\overrightarrow{\mathrm{S}_d}$ and $\overrightarrow{\mathrm{s}}$ are the impurity spin and the spin of the conduction electrons, respectively. The antiferromagnetic coupling between the magnetic electron and the conduction electrons J is introduced as:

$$J = -|V_k|^2 \frac{U}{\varepsilon_d (U + \varepsilon)}. \tag{3.11}$$

Kondo solved Eq. 3.10 by considering the spin-dependent interaction between the conduction electrons and the impurity electron to obtain the electrical resistivity [51]. He obtained a logarithmic term for the electrical resistivity that was proportional to the temperature. The critical temperature at which the resistivity became relevant is called the Kondo temperature T_K [62]:

$$k_\mathrm{B} T_\mathrm{K} \propto \mathrm{e}^{-J}, \tag{3.12}$$

with k_B being the Boltzmann constant.

The Kondo temperature can be calculated from the parameters of the Anderson model as:

$$T_\mathrm{K} = \frac{\mathrm{W}}{k_\mathrm{B}} = \sqrt{2\Gamma \frac{U}{\pi}} \exp\left[\frac{-\pi}{2\Gamma} \left(\frac{1}{\varepsilon_d} + \frac{1}{U + \varepsilon_d} \right)^{-1} \right], \tag{3.13}$$

with W being the half width at half maximum of the Kondo resonance [63]. Therefore, the Kondo temperature provides a measure of the spin exchange coupling strength between the magnetic impurity and the conduction electrons of the surface. Considering the exponential dependency of the Kondo temperature on U, Γ, and ε_d, the Kondo temperature is very sensitive to small changes of these parameters.

Kondo fingerprint in STM: quantum interference

For surface impurities the Kondo effect can be detected by means of STM. Two pioneering STM experiments have measured Kondo resonances independently in 1998 [52, 53]. Surprisingly, the lineshape of the Kondo resonance was not a perfect Lorenzian, reflecting the many body state in the DOS. Instead, it showed an asymmetric peak, which could be well described with a Fano lineshape. It arises from the interference between different transport paths with the same initial and final states [64].

Electrons from the tip have two possibilities to tunnel to the sample. Fig.3.5(a) shows both paths, of which the first is direct tunneling to the unoccupied states above $\mathrm{E_F}$ of the surface, and the second is indirect tunneling via the Kondo resonance of the magnetic impurity. Their interference results in the resonance appearing with a Fano line shape, which is described by [63]:

$$\mathrm{Fano}(E) \propto \rho_0 + \frac{(q+\epsilon)^2}{1+\epsilon^2}, \tag{3.14}$$

where $\epsilon = \frac{\mathrm{E}-\mathrm{E_K}}{\mathrm{W}}$, with $\mathrm{E_K}$ being the position in energy of the Fano resonance. The so-called Fano factor q corresponds to the ratio between the direct and indirect tunneling probabilities t_1 and t_2, and is expressed as [64]:

$$q = \frac{t_2}{2\pi\rho_0 \mathrm{V} t_1}. \tag{3.15}$$

Here, V is the hybridization matrix element between the impurity level with the continuum of the underlying substrate.

The Fano factor q defines the corresponding line shapes of the resonances. Fig.3.5(b) shows three Fano line shapes, which have different q factors. In case of the q factor going to infinity, the Fano line shape exhibits a perfect Lorentzian line shape, corresponding to the dominance of indirect tunneling. However, in case of dominance of direct tunneling, the q factor is zero and the Fano resonance appears as a dip. Intermediate values of the q factor give rise to asymmetric curves, as can be seen for q=1 in Fig.3.5(b) [63].

The Kondo resonance under the influence of external factors

After understanding the physical picture of the Kondo effect, the influence of external parameters such as magnetic field and temperature have to be considered. The Kondo resonance is broadened by temperature. The relation between this broadening under the assumption of $\mathrm{T} \ll \mathrm{T_K}$ can be expressed as [65]:

$$\mathrm{W} = \sqrt{(\pi k_\mathrm{B} T)^2 + 2(k_\mathrm{B} T_\mathrm{K})^2}. \tag{3.16}$$

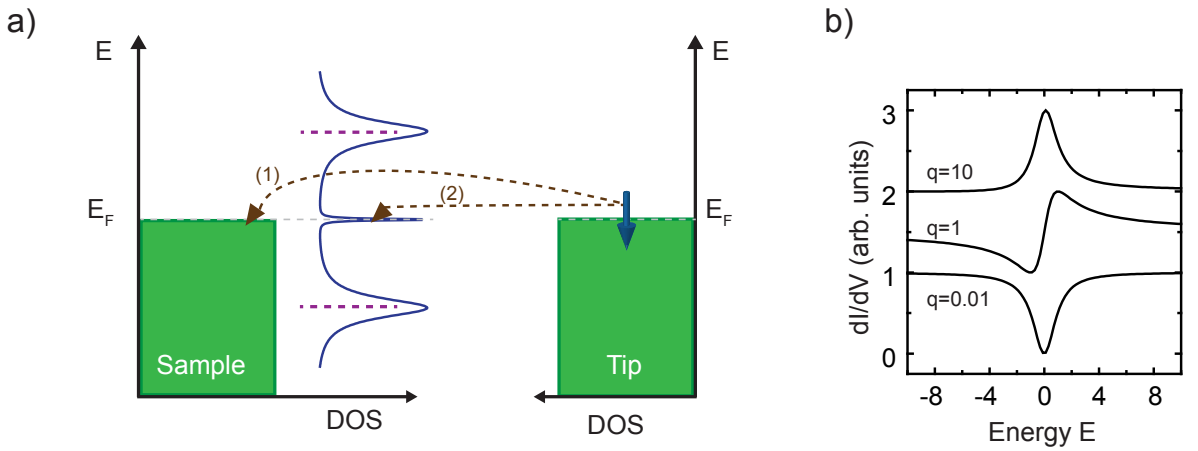

Figure 3.5: a) Sketch of the STM junction consisting of the tip and a magnetic impurity with singly/doubly occupied molecular orbitals on the surface. Electrons from the tip have two different tunneling paths: (1) Direct tunneling to unoccupied states of the surface. (2) Indirect tunneling through the Kondo state. These two paths can interfere with each other and give rise to a Fano line shape of the Kondo resonance in experiment. b) Fano line shape with different q factors as indicated in the figure.

Moreover, the many-body ground state of the screened spin from the magnetic impurity and the conduction electrons remains unperturbed in case of small applied magnetic fields. However, as soon as the Zeeman energy of the external magnetic field is similar compared to the spin exchange interaction energy (between the magnetic impurity and the underlying surface) the Kondo resonance starts to split [66, 67]. This magnetic field, which is called the critical field can be calculated as:

$$\mathrm{B_C} = \frac{k_\mathrm{B} T_\mathrm{K}}{2\mathrm{g}\mu_\mathrm{B}}, \tag{3.17}$$

where μ_B and g are the Bohr magneton and the gyromagnetic factor of a free electron, respectively. By increasing the magnetic field, the Kondo resonance splits, according to the Zeeman effect [68]. The behavior of the Kondo resonance with temperature and external magnetic field can be used as a criterion to unambiguously identify the Kondo effect to be the origin of a zero-bias feature in the spectra.

3.2.4 Magnetic impurity on a superconducting substrate

The spin exchange scattering between the conduction electrons of a normal metal substrate and the electrons of the magnetic impurity has been discussed in the previous section. In this section, the interaction between a magnetic impurity and the Cooper pairs of a superconducting substrate will be discussed. Therefore, we briefly describe the effect of paramagnetic impurities on the Cooper pairs, starting with the *classical spin*,

which is a static spin. This will be followed by the *quantum spin* picture, using the Anderson impurity model introduced above.

Classical spin

Exchange scattering between the spin of an impurity and the quasiparticles of a superconductor weakens the pairing energy of the Cooper pairs locally. This gives rise to a new state inside the superconducting gap. The strength of the exchange coupling is determined by the potential and magnetic interaction of the impurity spin. These states have been described theoretically by L. Yu, H. Shiba, and A.I. Rusinov in the 1960s and are known as Yu-Shiba-Rusinov (YSR) states or Shiba states [10–12]. In the following we will discuss the theoretical description of the Shiba states, starting from a classical spin. A classical spin is a static spin with a fixed magnetization direction. This is achieved by setting $\mathrm{S} \to \infty$ with $J \to 0$, such that their exchange interaction $\mathrm{S}J$ is finite. Shiba introduced the Hamiltonian [69]:

$$\hat{H} = \sum_{\mathbf{k}\sigma} (\mathrm{V} + \epsilon_{\mathbf{k}}) c^{\dagger}_{\mathbf{k}\sigma} c_{\mathbf{k}\sigma} - \Delta_0 \sum_{\mathbf{k}} \left(c^{\dagger}_{\mathbf{k}\uparrow} c^{\dagger}_{-\mathbf{k}\downarrow} + c_{-\mathbf{k}\downarrow} c_{\mathbf{k}\uparrow} \right) - \frac{J}{2N} \sum_{\mathbf{k}\,\mathbf{k'}} c^{\dagger}_{\mathbf{k}} \boldsymbol{\sigma} c_{\mathbf{k}} \mathbf{S}. \tag{3.18}$$

Here, σ is the spin of a superconductor quasiparticle and V is the scalar potential of the impurity. The exchange coupling between the impurity and the underlying superconductor gives rise to a pair of bound states at an energy of [69]:

$$E_{\mathrm{Shiba}} = \pm \Delta_0 \frac{1 - \alpha^2 + \beta^2}{\sqrt{(1 - \alpha^2 + \beta^2)^2 + 4\alpha^2}}, \tag{3.19}$$

with $\alpha = \pi \rho_0 S J$, $\beta = \pi \rho_0 V$ and ρ_0 being the density of states in the normal state. Three different situations are of interest: (1) $\alpha > 1 + \beta$, meaning that the exchange coupling strength between the impurity spin and the Cooper pairs is large enough to bind a single spin to the impurity. The new ground state of the impurity electron and the superconducting substrate is then $S = 0$. This give rises to a Shiba state right at the edge of the BCS gap. By decreasing the exchange coupling strength, the Shiba state shifts towards the Fermi energy [38, 70–72]. (2) In case of $\alpha = 1 + \beta$, the exchange coupling is reduced such that the energy of the Shiba state is zero. At this point a quantum phase transition occurs into a $S = \frac{1}{2}$ ground state [13]. (3) Upon further decreasing of the exchange coupling strength $\alpha < 1 + \beta$, the Cooper pairs remain intact and the ground state is $S = \frac{1}{2}$. In a spectrum, a Shiba state corresponds to a quasiparticle excitation from the ground state ($S = 0$ or $S = \frac{1}{2}$) to the first excited state ($S = \frac{1}{2}$ to $S = 0$) by adding or removing an electron. The signature of a Shiba state in an excitation spectrum can be resolved as two peaks at opposite energies with respect to the Fermi level inside the superconducting gap [73].

Quantum spin

Often, the description of an impurity as a classical spin is insufficient because the spin of an impurity is not a fixed classical spin. Thus the spin of the impurity possesses a dynamic magnetization direction, which can be involved in spin exchange scattering processes, e.g., the Kondo effect. Hence, the spin of impurity has to be described in a quantum mechanical picture. In this case, we apply the Anderson impurity model to treat our system. As it has been explained in the previous section (Sec.3.2.3), we assume an unpaired electron in a singly occupied level lying at the energy ε_{d} that is separated from the doubly occupied state by the Coulomb repulsion U. The corresponding energy of the Shiba state can be expressed as [69]:

$$E_{\mathrm{Shiba}} = \pm\Delta_0 \frac{\Gamma^2 - (\varepsilon_{\mathrm{d}} - \mu + \mathrm{U}/2)^2 - (\mathrm{U}/2)^2}{\sqrt{(\Gamma^2 + (\varepsilon_{\mathrm{d}} - \mu + \mathrm{U}/2)^2 - (\mathrm{U}/2)^2)^2 + \Gamma^2\mathrm{U}^2}}, \tag{3.20}$$

where μ is the chemical potential and Γ is the coupling strength of the impurity level with the underlying substrate. It is worth mentioning that a nonzero μ breaks the electron-hole symmetry and thus gives rise to different intensities of electron-like and hole-like quasiparticle components of the Shiba state.

Similar to the case of a classical spin (see Sec.3.2.4), when the exchange coupling strength is high enough to bind a single spin to the impurity, the impurity is *screened*, and the system's ground state is a singlet $S = 0$ (Fig.3.6(a)). This many-body state that arises from the impurity spin and quasiparticles that bind to it, corresponds to the Kondo state. The width of this Kondo state is larger than the superconducting gap ($k_{\mathrm{B}}T_{\mathrm{K}} > \Delta$). By decreasing the exchange coupling strength such that the impurity spin is not bound to any quasiparticles, the ground state of the system is a spin doublet $S = \frac{1}{2}$ the so-called *free spin* configuration. Here, there is no Kondo resonance in the superconducting state. However, in the normal state, the system exhibits a Kondo state with a Kondo width smaller than the superconducting gap ($k_{\mathrm{B}}T_{\mathrm{K}} < \Delta$) (Fig.3.6(b)). The exchange coupling strength of the quasiparticles with a magnetic impurity determines the Shiba ground state as well as the Kondo width. The relation between the Kondo width and the evolution of the Shiba state can help us to reveal the ground state of the particular experimental system [16, 17]. In the following chapter, we study the interaction between the magnetic impurity and a superconducting surface. The evolution of the interaction between the magnetic moment of an impurity with the substrate will be investigated depending on their adsorption site and tip influence.

Additionally, the intensity of the electron-like quasiparticle (indicated as red line in Fig.3.6(a,b) middle panels) and hole-like quasiparticle (indicated with green line in Fig.3.6(a,b) middle panels) can differ from each other. This asymmetry is determined by the scalar potential, which changes the probabilities of exciting the Shiba state by adding or removing an electron differently [74]. In a simplified picture, this means that, if the excitation of the Shiba state by adding an electron has higher probability, the intensity of the hole-like quasiparticle is higher [74].

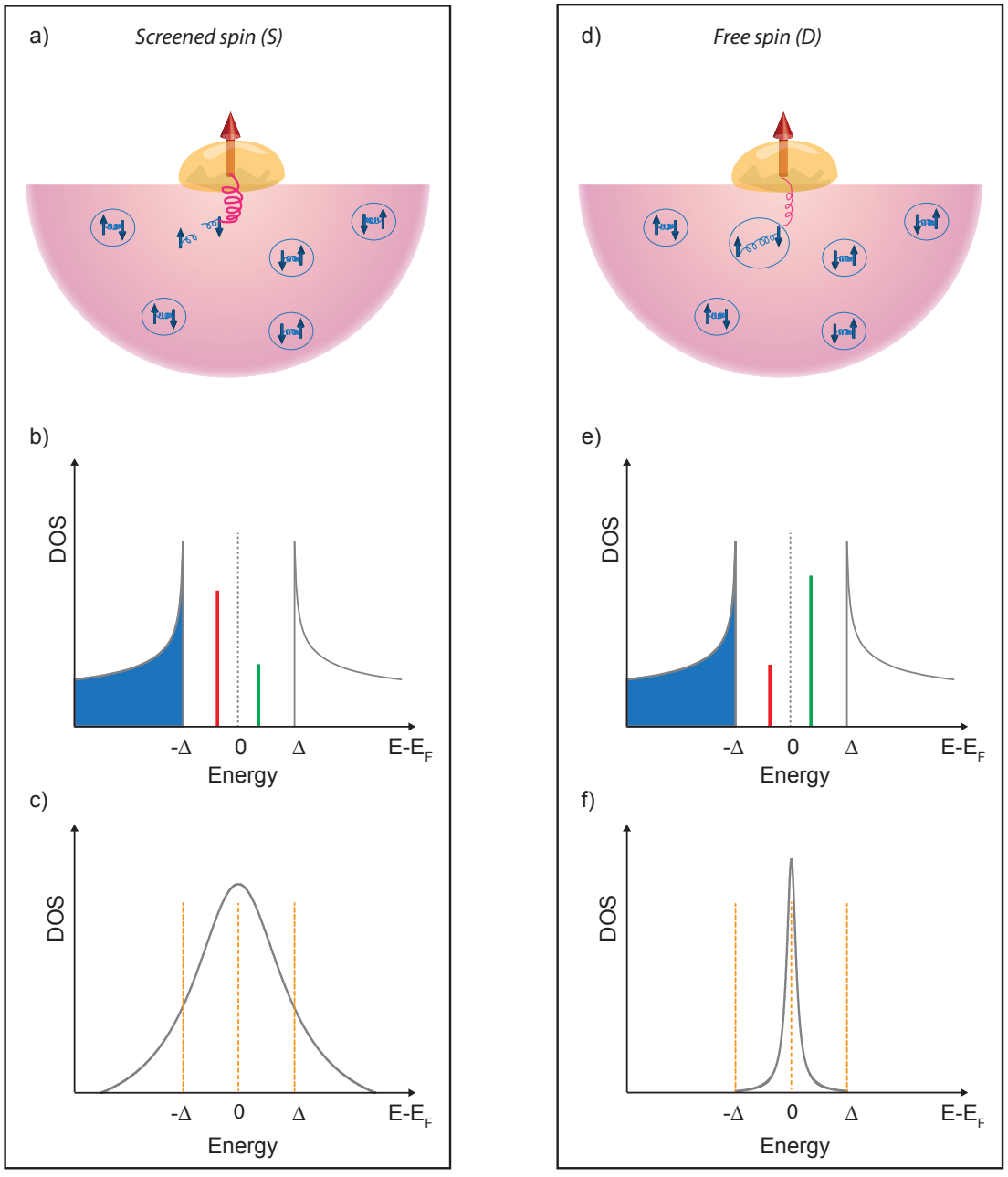

Figure 3.6: a) Schematic drawing of the *screened spin* regime. The exchange coupling strength J is larger than the Cooper pairing, resulting in a screened many body state. b,e) The electron-like and hole-like quasiparticle components of the Shiba state are shown with red and green lines, respectively. Depending on the scalar potential they can exhibit asymmetric intensities. c) The corresponding Kondo resonance, showing a larger width than the superconducting gap. d) *Free spin* regime. The exchange coupling strength J is smaller than the pairing energy. f) The corresponding Kondo resonance has a smaller width than the superconducting gap.

Chapter 4

Metal-organic networks on Pb(111)

The results presented in this chapter have been published as:

- *"Self-assembly of tetracyanonaphtho-quinodimethane (TNAP) based metal-organic networks on Pb(111): Structural, electronic, and magnetic properties"* by G. Ahmadi and K. J. Franke, *Applied Surface Science* **373**, 2 (2016).

4.1 Introduction

The adsorption of molecular layers is one of the key strategies to confer a desired functionality to a surface. The construction of long-range ordered structures relies on self-assembling processes, which are driven by attractive forces between the adsorbates. Interactions of the adsorbates with the substrate further influence the resulting structure and electronic properties. Enormous amounts of examples of self-assembled homo-molecular [75–77], hetero-molecular [77–79], as well as metal-organic structures [77, 80, 81] have been reported on noble metal surfaces. Their envisioned functions demand the formation of templates for adsorption cavities [82–85], the tailoring the electronic structure for tuning the dispersion of surface bands [86–88], the stabilization of magnetic properties [89–91] for information storage. New perspectives arise, if the substrate was not a simple metal, but a superconductor. This is particularly interesting for the design of magnetic networks on a superconductor. A single magnetic adsorbate can serve as a scattering potential for the quasiparticles of the superconductor, i.e., the Cooper pairs. This gives rise to so-called Yu-Shiba-Rusinov states [10–12], which appear as transport resonances inside the superconducting energy gap [14–16]. Recently, it has been pointed out theoretically that a lattice of such magnetic scattering centers leads to intriguing topological properties [92]. It has also been emphasized that, in particular, metal-organic structures on superconducting Pb could possibly lead to topological conditions, which bear Majorana states [93].

Here, we explore the self-assembly of metal-organic structures on the superconducting Pb(111) surface. As a promising molecular linker for metallic atoms, we chose 11, 11, 12, 12-tetracyanonaphtho-2, 6-quinodimethane (TNAP). This molecule is well suited as a building block for metal-organic networks with alkali atoms as well as transition metal atoms [94]. On the one hand, the capability to form self-assembled networks with alkali atoms can be ascribed to its large electron affinity ($E_A = 4.7$ eV), which tends to withdraw the valence electron from the alkali atom to form an ionic bond. On the other hand, the cyano terminations with their lone-pair electrons are prone to form coordination bonds to transition metal atoms [75, 77, 81].

We first characterize the structural and electronic properties of pure TNAP on the Pb(111) surface. The mobility and electronic flexibility to sustain different bonding symmetries of Pb atoms leads to a Pb-TNAP network formed at room temperature, where Pb forms the bonding node between the electrophilic cyano terminations. We further show that Na atoms provided by co-deposited NaCl islands lead to long-range ordered Na-TNAP structures, which are probably stabilized by an ionic bonding nature. Co-deposited Fe atoms are also incorporated into bonding nodes with the cyano groups. However, we could not observe long-range ordered structures on Pb(111). We show that the local symmetry of the Fe coordination drastically affects the magnetic properties. Only some Fe atoms surrounded by TNAP molecules in a local C2 symmetry show Shiba resonances as a fingerprint of magnetic interaction with the superconductor.

4.2 Experimental details

All experiments were carried out under ultra high vacuum conditions with the base pressure of $< 10^{-9}$ mbar. An atomically clean Pb(111) surface was prepared by repeated cycles of Neon ion sputtering and subsequent annealing to 530 K. 11, 11, 12, 12-tetracyanonaphtho-2, 6-quinodimethane (TNAP) and sodium chloride (NaCl) were deposited from Knudsen cells at 450 K and 810 K, respectively. Iron was sublimed from an ultra pure rod (99.99% purity) by electron bombardment. The sample was kept at the indicated temperature for each experiment and eventually post-annealed. The sample was then cooled and transferred into a custom-build scanning tunneling microscope, operated at 4.5 K. Tunneling spectra were acquired with a lock-in amplifier at a modulation frequency of 833 Hz. The modulation voltages and feedback conditions are indicated in the figure captions. The STM tip was covered by a thick layer of Pb by controlled indentation into the surface while applying 100 V. This procedure was repeated until the tip exhibited bulk-like Pb properties, in particular a superconducting energy gap around the Fermi level [16].

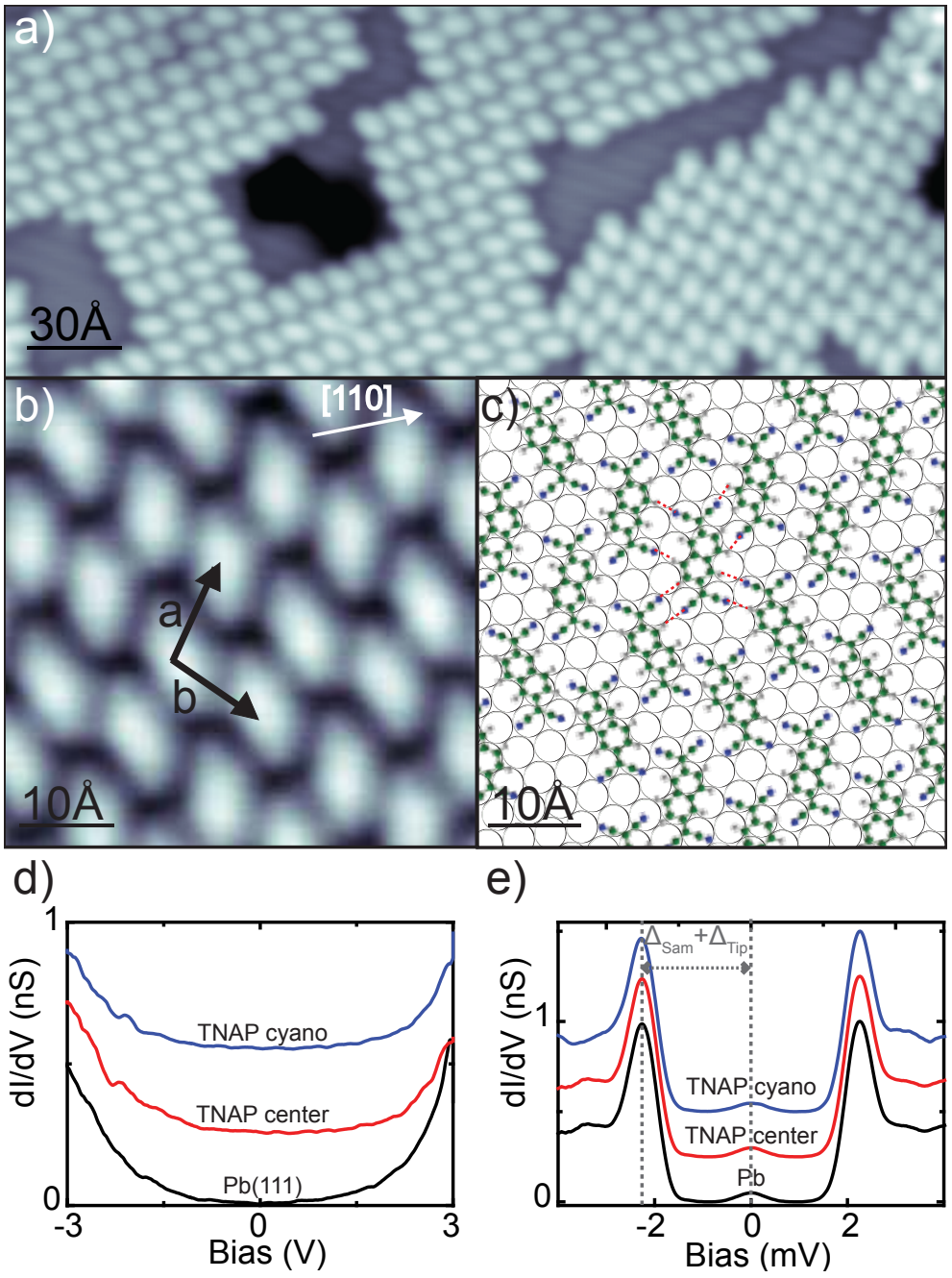

Figure 4.1: a) STM topographic image of TNAP islands on Pb(111)($I = 0.2$ nA and $V_{bias} = 290$ mV) b) STM image of TNAP island with rhombic unit cell indicated by arrows ($I = 1.1$ nA and $V_{bias} = -30$ mV). c) Structure model of TNAP island on top of Pb(111). d) Constant height dI/dV spectra acquired over the different sites of the TNAP molecules and on the clean Pb(111) surface (feedback opened at $I = 0.2$ nA and $V_{bias} = 3$ V with the modulation of $V_{\mathrm{rms}} = 5$ mV). e) Constant height dI/dV spectra around the Fermi level over the different sites of the TNAP molecules and on the clean Pb(111) (feedback opened at $I = 0.23$ nA and $V_{bias} = 10$ mV with the modulation of $V_{\mathrm{rms}} = 0.1$ mV). The spectra in (d, e) are offset for clarity.

4.3 Results and discussion

4.3.1 TNAP on Pb(111)

Deposition of a submonolayer of TNAP onto Pb(111) at 160 K leads to the formation of well-ordered molecular islands as shown in Fig.4.1(a). The islands exhibit a preferential orientation with the molecular rows aligned along the [110] direction of the Pb lattice [95]. A close-up view into the islands reveals the size and shape of the molecules [Fig.4.1(b)]. The molecules are separated by $a = b = 10 \pm 1$ Å, where a and b enclose an angle of $\alpha = 98 \pm 2°$. This allows for a flat-lying adsorption on the substrate, which is typical for organic molecules with an extended π electron system along a flat backbone [75, 78]. The corresponding structural model in Fig.4.1(c) is very similar to TNAP islands on gold [94, 96, 97]. Intermolecular electrostatic forces from the electronegative N atoms to the H atoms of the quinodimethane unit probably stabilize the densely packed islands on both surfaces. Since the difference in the two enantiomers is minute, both of them are statistically incorporated in the islands, as can be recognized from the slighly different orientation of the molecules, similar to the case on Au(111) [97]. Whereas no commensuration of the islands was found on Au(111) [96, 97], the molecules are in registry with every fourth Pb atom in the [110] direction. This commensuration of the two lattices probably contributes to the stabilization of the molecular islands.

TNAP is a model molecular charge acceptor with an electron affinity of $E_A = 4.7$ eV [94]. When brought into contact with a Pb surface, which exhibits a workfunction of $\Phi_{Pb} = 3.8$ eV [98], one may expect a significant amount of charge transfer [99]. To elucidate on the molecular energy level alignment and possible traces of charge transfer, we record scanning tunneling spectra (STS) on the cyano groups and the molecular center. None of them exhibits obvious resonances in the energy range of ± 3 eV [Fig.4.1(d)]. In search for a sign of charge transfer we also examine the region of the superconducting energy gap. Pb is a type I Bardeen-Cooper-Schrieffer (BCS) superconductor with a critical temperature $T_c = 7.2$ K. At our measurement temperature of 4.5 K the superconducting state is characterized by an energy gap of $\Delta = 2.2$ meV. Differential conductance spectra recorded with a superconducting tip on a superconducting substrate reflect the BCS-like resonances as two sharp peaks at an energy of $\pm 2\Delta$ [see Fig.4.1(e)]. The small peak at the Fermi level is due to tunneling of thermally excited quasiparticles [16]. In the case of a single electron being localized in a TNAP orbital one may expect that its exchange interaction with the superconducting substrate gives rise to Shiba states, which are an expression of an anti-ferromagnetic coupling of an unpaired electron spin with the Cooper pairs of the superconductor [10–12]. We do not find a hint of such resonances inside the superconducting energy gap [Fig.4.1(e)].

The absence of any such spectroscopic signatures could be indicative of a large molecular energy gap around the Fermi level. However, this is very unlikely, because the free molecule has an energy gap of $E_g = 1.95$ eV [94], which is typically reduced on a metal surface [100]. Instead, we suggest a completely different scenario, which can be derived from a simple model of energy level alignments considering

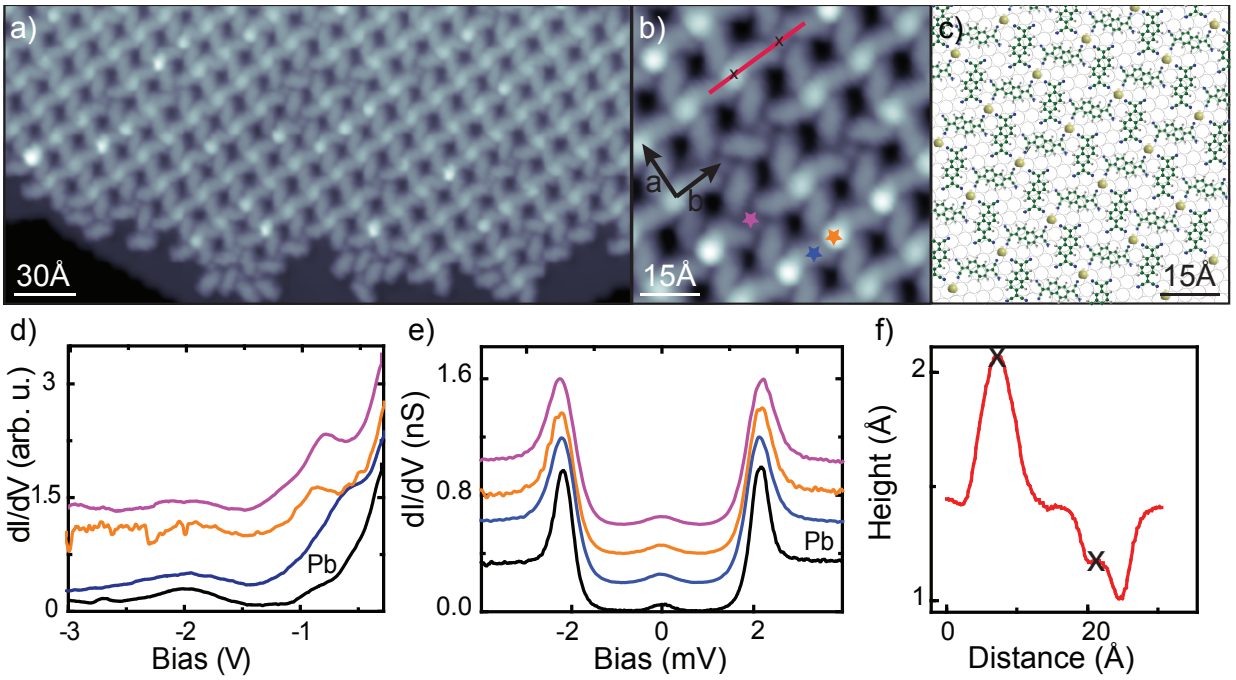

Figure 4.2: a) Large-scale STM image of the porous Pb-TNAP network on Pb(111). b) Zoom into the Pb-TNAP structure with the lattice vectors indicated by arrows a and b ($I = 0.5$ nA and $V_{bias} = 10$ mV). c) Structural model according to the STM images, which provides a commensurate structure with the Pb atoms sitting on hollow sites. d) Constant-current dI/dV spectra acquired over the different Pb atoms and TNAP molecule ($I = 0.5$ nA, lock-in modulation $V_{\mathrm{rms}} = 5$ mV). e) Constant height dI/dV spectra around Fermi level acquired over "dark" and "bright" Pb atoms and a TNAP molecule (feedback opened at $I = 0.5$ nA, $V_{bias} = 10$ mV, $V_{\mathrm{rms}} = 0.1$ mV). The location of the spectra are indicated by colored stars. The spectra in (d, e) are offset for clarity. f) Height profile along the line indicated in (b).

$\Phi_{Pb} < E_{A,\,TNAP}$. Due to the smaller workfunction, electron density is transferred from the substrate to the TNAP molecules [101]. The amount of charge transfer is determined by the electrostatic potential and extension of wavefunctions at the interface. Presumably, this leads to a non-integer charge state with considerable hybridization of molecular and substrate states. The mixing of electronic states also explains the diffuse appearance of the TNAP orbitals in the STM images.

4.3.2 Pb-TNAP coordination network on Pb(111)

We observe a distinctly different structure when the TNAP molecules are deposited at slightly higher temperature, i.e., at 330 K [Fig.4.2(a)]. Instead of the densely-packed molecular island, the resulting structure exhibits open pores. The TNAP molecules can be identified by their size and shape as flat lying in a windmill-shaped arrangement around fourfold nodes, where four cyano groups point towards each other

[Fig.4.2(b,c)]. The nodes are filled with small protrusions, which exhibit two different apparent heights in the STM images, i.e., 2.1 Å and 1.2 Å, respectively. Such a bonding pattern is reminiscent of metal-organic coordination motives, in which a metal atom acts as the bonding "glue" between the electrophilic cyano end groups [102–106]. At this growth temperature, atoms from the step edges possess sufficient thermal mobility for reacting with the TNAP molecules. The formation of similar metal-organic networks frequently occurs on noble metal substrates, where the $3d$ transition metal atoms from the substrate attach to electrophilic molecular endgroups and support a coordination bond [104, 106–113].

The Pb-TNAP network is fully commensurate with the substrate. Its structure can be described by the lattice vectors $a = b = 15$ Å enclosing an angle of $\alpha = 85°$. The Pb adatoms can thus sit in hollow sites, which would also be their energetically preferred adsorption site in an isolated case [114]. The arrangement of the TNAP molecules is stabilized by their coordination to the Pb adatoms as well as by intermolecular electrostatic N–H bonds with the typical length of 2.2 ± 0.2 Å. The N–N distance amounts to 5.6 ± 0.2 Å, resulting in a minimum Pb–N bond length of 2.8 ± 0.2 Å, assuming that the Pb atoms lie in the molecular plane. This value agrees with the typical Pb–N bond lengths in three-dimensional cyano–Pb bonding motives [115, 116]. The two different apparent heights of the Pb adatoms further suggest a rather shallow energetic minimum with a bistable configuration. Occasionally, we observe that the lower configuration can be switched into the higher one during scanning.

Although only one surface-anchored Pb-organic network has been reported so far [117], its occurrence is not too surprising. The large radius and p-block valence electron configuration of Pb allows it to adapt several oxidation states and bonding geometries, being the reason for the wealth of Pb based three-dimensional metal-organic frameworks [118, 119]. However, probably the closest resemblance of the coordination motif is borne to Pb-phthalocyanines, where the Pb core is ligated by four N atoms in a square pyramidal fashion [120].

To investigate the electronic structure within the metal-organic network, we recorded tunneling spectra on the TNAP molecules and the Pb nodes [Fig.4.2(d)]. The unoccupied states do not show any deviation from the plain molecules (not shown). In the occupied states, we find a resonance at -0.9 eV on the Pb adatoms. Its precise value varies between the "dark" and "bright" adsorption state. The TNAP molecules exhibit a resonance at -0.6 eV. Both features are unique to the Pb-TNAP network; neither the pure TNAP island (see above) nor single Pb atoms on Pb(111) show such a resonance [114]. One possible bonding type would be ionic due to charge transfer from the Pb atom to the acceptor molecule TNAP. To check for a possible sign of this, we acquired tunneling spectra in the superconducting energy region. Again, we do not detect any sign of Shiba states, which could signify the presence of an unpaired electron spin and hence single charge occupation. Another possible bonding would be of more covalent character. The bonding angle between C–N–Pb being 180° is in agreement with a directional bonding pattern, similar to windmill structures of transition metal atoms and tetracyanoquinodimethane (TCNQ)– the parent compound of TNAP [103, 105].

4.3.3 Na-TNAP metal-organic network

Motivated by the observation of ionic bonding between TCNQ and alkali metal atoms [105, 121, 122], we explore this possibility for TNAP in the following. As an alkali metal source, we deposit NaCl on the Pb(111) surface at room temperature. This leads to the formation of bi-layer islands of NaCl, similar to their growth on noble metal substrates [see inset of Fig.4.3(a)] [123–125]. Subsequent deposition of TNAP at room temperature results in a dissolution of the NaCl islands. Instead, we find rectangular patterns of TNAP with lattice vectors $a = 9 \pm 1$ Å and $b = 14 \pm 1$ Å [Fig.4.3(a)]. These structures include fourfold nodes of cyano endgroups. These can only be stabilized by the inclusion of an adatom which mediates a bonding configuration and thus overcomes the electrostatic repulsion of the electron-rich cyano terminations. Because Pb atoms lead to a different bonding pattern (see above), the incorporated atom can be assigned to Na. Again, the islands consist of both enantiomers as reflected by the molecular shape in the STM images [Fig.4.3(b)]. Both orientations allow for the quinodimethane unit to align along the [110] crystal direction of the Pb substrate. This imprints the preferential orientation of the islands on the Pb(111) surface. However, we do not find any commensuration of the whole Na-TNAP layer with the substrate [Fig.4.3(c)].

The dissolution of the ionically bonded NaCl islands indicates that the preferentially formed Na-TNAP islands exhibit an even larger bonding energy. Such a large bonding energy typically involves a strong ionic contribution, which is expected to arise from the charge transfer of the $3s$ electron of Na to the electrophilic TNAP molecule [121, 122]. To probe possible signatures of such a charge redistribution, we record differential conductance spectra on the Na and TNAP sites. The spectra on the Na sites reveal a pronounced peak at -0.85 eV, whereas the TNAP spectra are essentially flat [Fig.4.3(d, e)]. If the $3s$ electron is donated from Na to TNAP, the density of states of the closed-shell cationic Na is expected to be depleted in a large energy range around the Fermi level [122]. In contrast, the anionic TNAP species should exhibit its half-filled LUMO orbital close to the Fermi level. The unexpected resonance distribution can, however, be described within the charge transfer model by considering the three-dimensional extension of the molecular orbitals. The transferred electron is mainly localized at the electrophilic cyano groups. The electrostatic potential of the cationic Na atom leads to a deformation of the molecular orbitals and their extension over the Na sites. Thus, the corresponding molecular resonance appears on top of the Na. This scenario has been corroborated theoretically in the very similar system of Na-TCNQ [122].

Differential conductance spectra around the superconducting energy gap on the Na sites do not exhibit Shiba states. This agrees with the closed-shell nature of Na after charge transfer [Fig.4.3(f)]. However, we also do not observe Shiba states on the TNAP. The reason for this absence may be manyfold: the hybridization of TNAP with the substrate may lead to a non-integer charge state or yield a potential scattering strength, where the Shiba states are not sufficiently far away from the superconducting gap edge to be detectable. Furthermore, the existence of Shiba states around an extended scattering potential due to

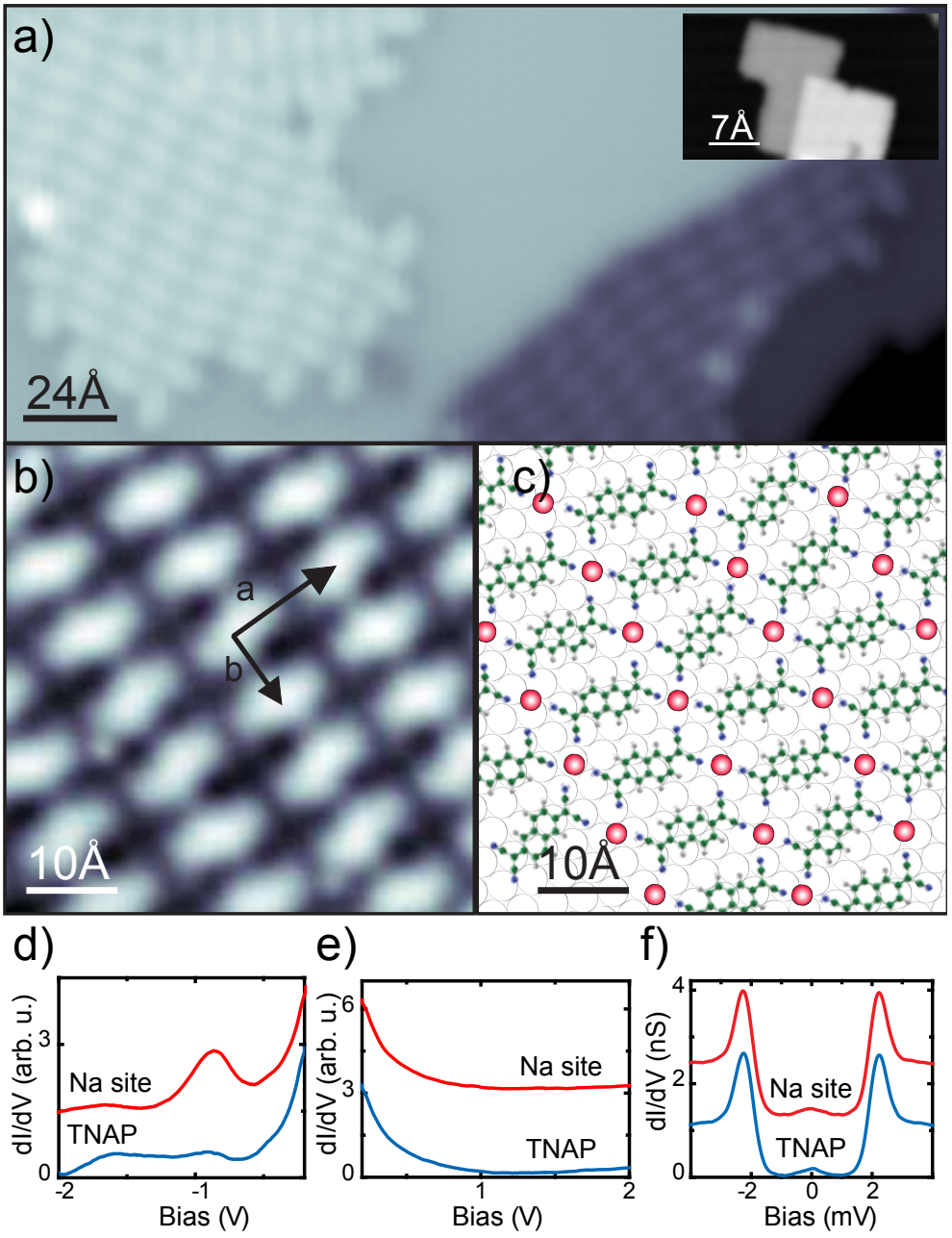

Figure 4.3: a) STM image of the Na-TNAP islands on Pb(111) ($I = 0.017$ nA and $V_{bias} = 1$ V). The inset shows an example of the previously prepared NaCl islands. b) STM zoom-in on the ordered Na-TNAP island ($V_{bias} = -11$mV). c) Proposed structure of Na-TNAP on Pb(111). d, e) Constant current dI/dV spectra acquired over the Na atom and TNAP molecule (set point is $I = 0.5$ nA, $V_{bias} = -200$ mV for (d) and $V_{bias} = 200$ mV for (e), $V_{\mathrm{rms}} = 5$ mV). f) Constant height dI/dV spectra around Fermi level acquired over Na atom and TNAP molecule (feedback opened at $I = 0.3$ nA, $V_{bias} = 10$ mV, $V_{\mathrm{rms}} = 0.1$ mV). The spectra in (d-f) are offset for clarity.

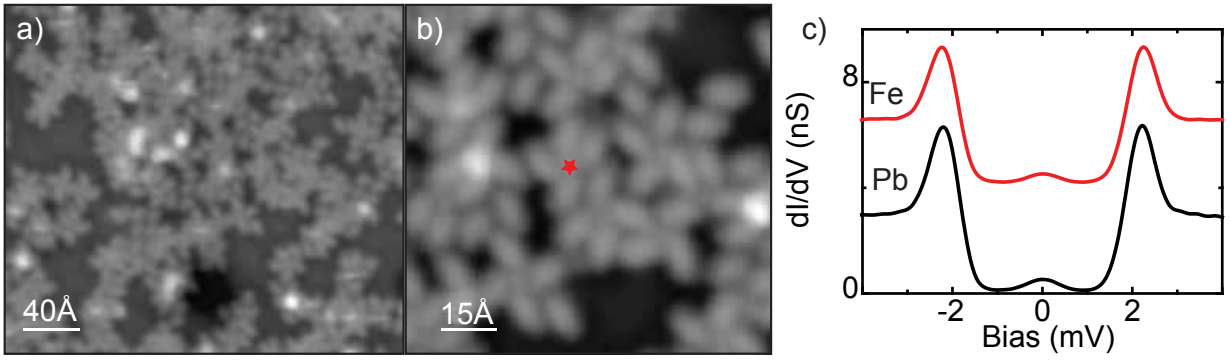

Figure 4.4: STM images of the Fe-TNAP network after deposition at 160 K: a) overview ($I = 0.21$ nA and $V_{bias} = 1$ V), b) zoom on the bonding nodes ($I = 0.21$ nA and $V_{bias} = 100$ mV). c) Constant-height dI/dV spectra acquired over the Fe indicated by a red star and Pb substrate (feedback opened at $I = 0.21$ nA, $V_{bias} = 10$ mV, $V_{\mathrm{rms}} = 0.1$ mV), spectra are offset for clarity.

an unpaired electron spin in an extended orbital has not been observed experimentally, neither discussed theoretically.

4.3.4 Fe-TNAP metal-organic network

To avoid the complexity of an unpaired spin in a delocalized orbital, we next turn to the creation of a metal-organic network, in which a magnetic moment is expected to be carried by a transition metal atom. We co-deposit TNAP molecules and Fe atoms onto the Pb(111) substrate held at 160 K. The resulting adsorption structure is an irregular network as shown in Fig.4.4(a). We can identify different nodes, where cyano groups point towards each other, albeit with different molecular symmetry. These nodes reflect the incorporation of Fe atoms into the TNAP surrounding [Fig.4.4(b)]. We have tested a few of the bonding nodes for a magnetic fingerprint inside the superconducting energy gap. However, for those cases, we could not observe any hint of Shiba resonances [see for example Fig.4.4(c)].

The high irregularity of the structure suggests insufficient mobility of the adsorbates for the creation of long range-ordered patterns. In an attempt to increase the order of the Fe-TNAP network we anneal the structures to 340 K. The overall appearance of the islands still remains highly irregular [Fig.4.5(a)]. Closer inspection of the bonding motives reveals the occurence of bonding nodes around which the TNAP molecules are arranged in a rectangular fashion [Fig.4.5(b)]. We suspect that these centers are Fe atoms, because Pb was shown to prefer a different coordination symmetry (see above). Differential conductance spectra on some of these Fe sites show resonances inside the superconducting energy gap [Fig.4.5(c)]. These Shiba states reflect the presence of a magnetic moment of the Fe atoms, which creates a scattering potential inside the superconductor. Unfortunately, the high irregularity of the structure does not allow for a systematic investigation of the appearance of the states. Their sole occurance in the rectangular lattice

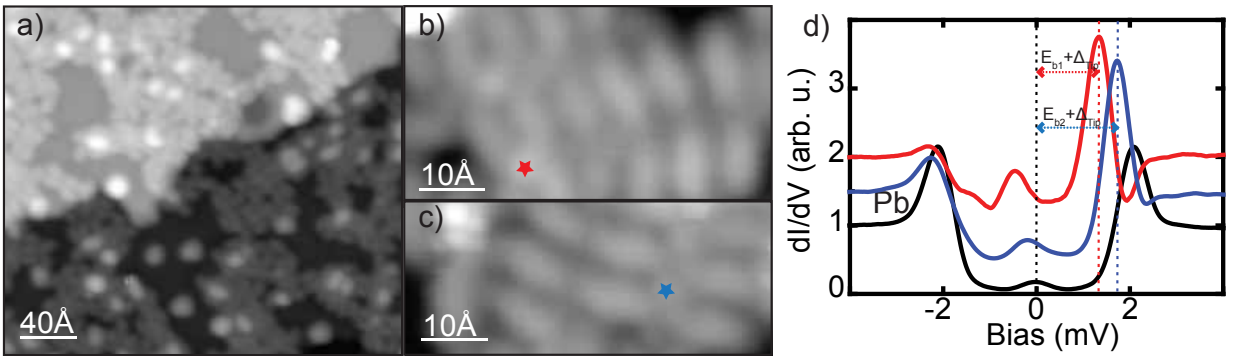

Figure 4.5: STM images of the Fe-TNAP network after annealing to 340 K: a) overview ($I = 0.21$ nA and $V_{bias} = 200$ mV), b,c) zoom on the bonding nodes ($I = 0.1$ nA and $V_{bias} = 110$ mV), d) Constant-height dI/dV spectra acquired over an Fe atom in a molecular C2 bonding node (indicated by a red star) and the Pb substrate (feedback opened at $I = 0.36$ nA, $V_{bias} = 10$ mV, $V_{\mathrm{rms}} = 0.1$ mV), spectra are offset for clarity.

sites suggests the necessity of a certain crystal field around the Fe atom. However, also the adsorption state of the neighboring TNAP molecules may influence the magnetic properties of the embedded Fe atom. The creation of long-range ordered structures is probably inhibited by the incorporation of both Fe and Pb adatoms, which prefer different bonding symmetries.

4.4 Conclusions

The Pb substrate has for long time eludet from studies of self-assembling processes. With the promising perspective of creating magnetic structures with topological properties, superconductors will certainly gain importance as substrates for metal-organic networks [92]. We have explored viable routes to create such networks based on the organic electron acceptor TNAP. We observed a very large mobility of Pb adatoms, which are prone to form coordination bonds with cyano-based organic linker molecules. This mobility hampers favorable kinetics for the formation of extended networks, where the bonding energy is of similar magnitude. In particular, this is the case for transition metals, such as Fe. An ionic bond, which is energetically favored over the Pb coordination bond, circumvents this problem. The combination of an alkalimetal (Na) with the molecule acceptor TNAP has proven to form long-range ordered structures. Despite the charge transfer, these structures did not exhibit fingerprints of a magnetic interaction with the superconducting substrate. In contrast, we have found the desired magnetic interaction with the superconductor on some Fe sites within the Fe-TNAP network. A systematic analysis of the energy level alignment of the Shiba states inside the superconducting energy gap in dependence of their surrounding was not possible due to the high irregularity of the network. Nonetheless, we expect that a careful design of the molecular linkers will allow for the creation of magnetic metal-organic networks with long-range order.

The quest for a magnetic pattern which creates topological states at the interface to the superconductor will surely enforce the efforts towards this goal.

Chapter 5

Metal-organic complexes on Pb(111)

5.1 Introduction

The spin of adsorbed metal-organic molecules on a superconducting substrate can interact with Cooper pairs of the underlying substrate. This can result in a so-called Yu-Shiba-Rusinov many body state [10–12]. Furthermore, depending on the magnetic exchange scattering strength, the spin of the impurity can be Kondo screened or -in weak exchange scattering- the Kondo screening is incomplete as it has been described in Sec.3.2.4. One way to manipulate this spin exchange scattering strength is to embed the magnetic atom into the organic ligand. By wisely choosing of different organic ligands, we can tune the distance between the magnetic atom and the underlying substrate to have different magnetic interaction.

Porphyrin and phthalocyanine organic molecules are well-known classes of molecules to capture different metals and producing metal-organic complexes on surfaces with different magnetic fingerprints [126–133]. It has been shown that manganese-phthalocyanine (Mn-PC) molecules on Pb(111) show a peak triplet that is attributed to the excitation of a three-fold degenerate spin state of Mn as the degeneracy has been lifted up due to the magnetic anisotropy [17]. Depending on the adsorption site, and the hybridization with the substrate, the ground state of this Shiba state undergoes a quantum phase transition [16, 17].

Furthermore, it has been shown that in case of more decoupled molecules iron-octaethylporphyrin (Fe-OEP) on Pb(111), the hybridization between the Fe center and the underlying substrate is small such that the quasiparticles of the substrate are not scattering from the magnetic moment of Fe. However, the magnetic fingerprint of this molecule can be detected via exciting the spin of Fe by providing enough energy. Moreover, the oxidation state of the Fe center has been changed by attaching the Cl atom (Fe-OEP-Cl), due to the long life-time of the spin in excited state, the next spin excitation is possible [18, 19].

Different magnetic fingerprints can be obtained in two ways: (1) using different magnetic atoms with different spin states. (2) Various organic ligands can adapt distinct conformation and, thus, different metal-substrate distances.

To manipulate the metal-sample distances, the porphyrin molecules are suitable candidates as they adapt different conformations upon adsorption on a surface. This can translate into different molecule-sample distances which can give rise to distinct electronic and/or magnetic properties [133–135].

Metal-tetrapyridylporphyrin (M-TPyP) is a π conjugated metal-organic complex, consisting of a central porphyrin macro-cycle with four pyridine groups attached to the macro-cycle via a carbon-carbon σ bond (Fig.5.1). In gas phase, the pyridine groups are perpendicular to the porphyrin plane to minimize steric repulsion [136]. The pyridine groups have two rotational degrees of freedom: they can rotate around the C-C bond (angle α in Fig.5.1) or/and bend with respect to the molecular plane (angle of φ in Fig.5.1).

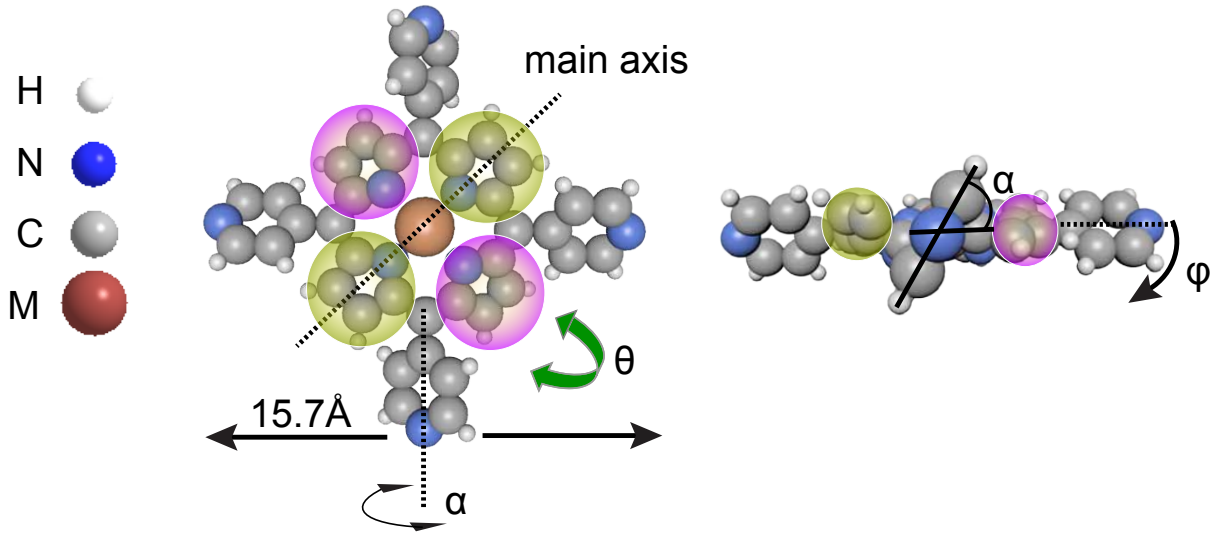

Figure 5.1: Stick and ball model of a M-TPyP molecule with indicated main axis, dihedral angle of the pyridine end group α and the buckling angle of the pyrrole group θ. Each pair of pyrrole groups that buckled up and down are indicated with yellow and pink circles, respectively. The bending angle of the pyridine group with respect to the molecular plane is indicated with φ (on the right).

On a surface, the pyridine groups tend to orientate parallel to the substrate in order to maximize the interaction with the substrate [128]. However, this distortion increases the steric repulsive force, which is reduced by a buckling of the pyrrole groups. Each pair of opposing pyrrole groups tilts up and down with respect to the molecular plane, leading to a saddle shape configuration of the molecule [132]. Fig.5.1 shows two pairs of pink and yellow circles, which indicate the up-tilted and down-tilted pyrrole groups, respectively. The angle of each pyrrole group with respect to the molecular plane is labeled by θ in Fig.5.1. The resulting saddle shape configuration of this family of molecules has been observed for tetraphenylporphyrin (TPP) [128, 137–142] and TPyP complexes [135, 138, 143, 144] on different surfaces.

In this chapter, we first evaporate the Fe-TPyP molecules on Pb(111). We investigate their structure,

electronic and magnetic properties. By substituting the Fe center by Mn, we try to manipulate their magnetic properties. Finally, by changing the pyridine end groups to more bulky tert-butyl end groups, we study the influence of this modification on their magnetic properties.

5.2 Experimental details

All experiments of Fe-TPyP molecules were carried out under ultra high vacuum conditions with a base pressure of $< 5 \times 10^{-10}$ mbar. After preparation, the sample was then cooled and transferred into a Specs Joule-Thompson scanning tunneling microscope JT-STM, operated at 1.1 K. Tunneling spectra were acquired with a lock-in amplifier at a modulation frequency of 912 Hz.

All experiments of Mn-TPyP and Mn-TPTBP were carried out under ultra high vacuum conditions with a base pressure of $< 1 \times 10^{-9}$ mbar. The sample was then cooled and transferred into a home-build scanning tunneling microscope (STM), operated at 4.5 K. Tunneling spectra were acquired with a lock-in amplifier at a modulation frequency of 833 Hz.

An atomically clean Pb(111) surface was prepared by repeated cycles of Neon ion sputtering and subsequent annealing to 430 K. 5,10,15,20-Tetra(4-pyridyl)porphyrin (Fe-TPyP) was deposited from a Knudsen cell at 650 K to the sample that was kept at room temperature during the evaporation. Manganese-5,10,15,20-Tetra(4-pyridyl)porphyrin (Mn-TPyP) and manganese tetra-phenyl-tert-butyl-porphyrin (Mn-TPTBP) were deposited from a Knudsen cell at 650 K and 620 K, respectively, to the sample that was kept at room temperature during the evaporation. The modulation voltages and feedback conditions are indicated in the figure captions. The STM tip was covered by a thick layer of Pb by controlled indentation into the surface while applying 100 V. This procedure was repeated until the tip exhibited bulk-like Pb properties, in particular a superconducting energy gap around the Fermi level [16, 17, 43]. To assure the cleanliness of the tip, we always compare to spectra taken on the bare Pb(111) surface.

5.3 Self assembly of magnetic iron-porphyrin complex on Pb(111))

The iron atom of iron-porphyrin molecules and iron phthalocyanine molecules is in $+2$ oxidation state [18, 145–147]. Depending on the molecular structure as well as the adsorption on different substrates, the Fe^{+2} atom can be in the low-spin state S=0 [148], the intermediate spin state S=1 [149, 150] or the high spin state S=2 [151]. Hence, depending on the spin state as well as the hybridization with the substrate, different magnetic fingerprints of Fe have been detected. Therefore, we choose the Fe-TPyP molecule as a model system, adsorbed on a Pb(111) single crystal substrate to study the effect of the local environment on its magnetic and electronic properties.

5.3.1 STM study of ordered Fe-TPyP molecules on Pb(111)

Deposition of a sub-mono-layer coverage of Fe-TPyP onto the Pb(111) surface leads to the formation of well-ordered molecular islands as shown in Fig.5.2(a). By recording STM topography images at different bias voltages, we observe two types of molecules with different contrast (indicated by green and red circles in Fig.5.2). By changing the polarity of the sample bias, (*e.g.* 800 meV) the contrast of these two types of molecules is inverted (see Fig.5.2(a,b)). The inversion of the apparent height due to the change in the bias polarity indicates that the difference predominantly arises from a difference in the electronic structure between both types of molecules, rather than from different geometrical conformations. The majority type (approx. 80%) is from now referred to as type A and the minority type (20%) as type B. STM images taken at 50 meV show the structure of type A and type B molecules with sub-molecular resolution (Fig.5.2(c) and Fig.5.2(d), respectively). Fe-TPyP molecules on Pb(111) exhibit a two fold symmetry. The reduction of the symmetry is an indication of a distorted molecule [152, 153], which can be ascribed to a saddle shape conformation [139, 154]. The type A molecule shows a central bright protrusion, which originates from the central Fe atom and two bright protrusions that are assigned to the two up-tilted pyrrole rings. The type B molecule has two bright protrusions corresponding to the up-tilted pyrrole groups and a depression in the center. Therefore, it appears plausible that both types of molecules adapt a saddle shape conformation but with slightly different distortions [139].

As one can see in Fig.5.3(a), the molecules form a nearly square structure with lattice constants of $a_1 = b_1 = (13.7 \pm 0.1)$Å (green vectors). In this arrangement, the type B molecules appear in a superstructure with nearly a square structure with lattice constants of $a_2 = b_2 = (31.0 \pm 0.5)$Å (red vectors). In this superstructure, each type B molecule is surrounded by four type A molecules.

By overlaying the symmetry of the substrate to the molecular island, we can investigate the registry of the absorption behavior of the molecules with the underlying Pb(111) substrate. As one can see in Fig.5.3(b), the two main axes of the molecules are rotated by -15° with respect to the [101] high symmetry directions of the substrate which have been previously determined by atomic resolution images. The molecules can have six equivalent orientations, which are all observed in our experiment. Moreover, the lattice of the molecular islands has a small angle ($(7 \pm 1)^\circ$) with respect to the $[101]$ high symmetry direction of Pb(111). Finally, the superstructure of type B molecules is commensurate with the underlying substrate such that all type B molecules of this superstructure are adsorbed on the same site.

However, the superstructure of type B molecules is often disturbed by defects or dislocations on the long range scale. In a three fold symmetric substrate top, bridge and hollow (fcc and hcp) adsorption sites are possible. The type B molecules could adapt to either of the three adsorption sites. In Fig.5.3(b), by assuming that the type B molecules adsorb on hollow sites, type A molecules have mainly on-top and bridge adsorption sites and vice-versa.

In conclusion, the different adsorption sites of the type B and type A molecules provide a unique

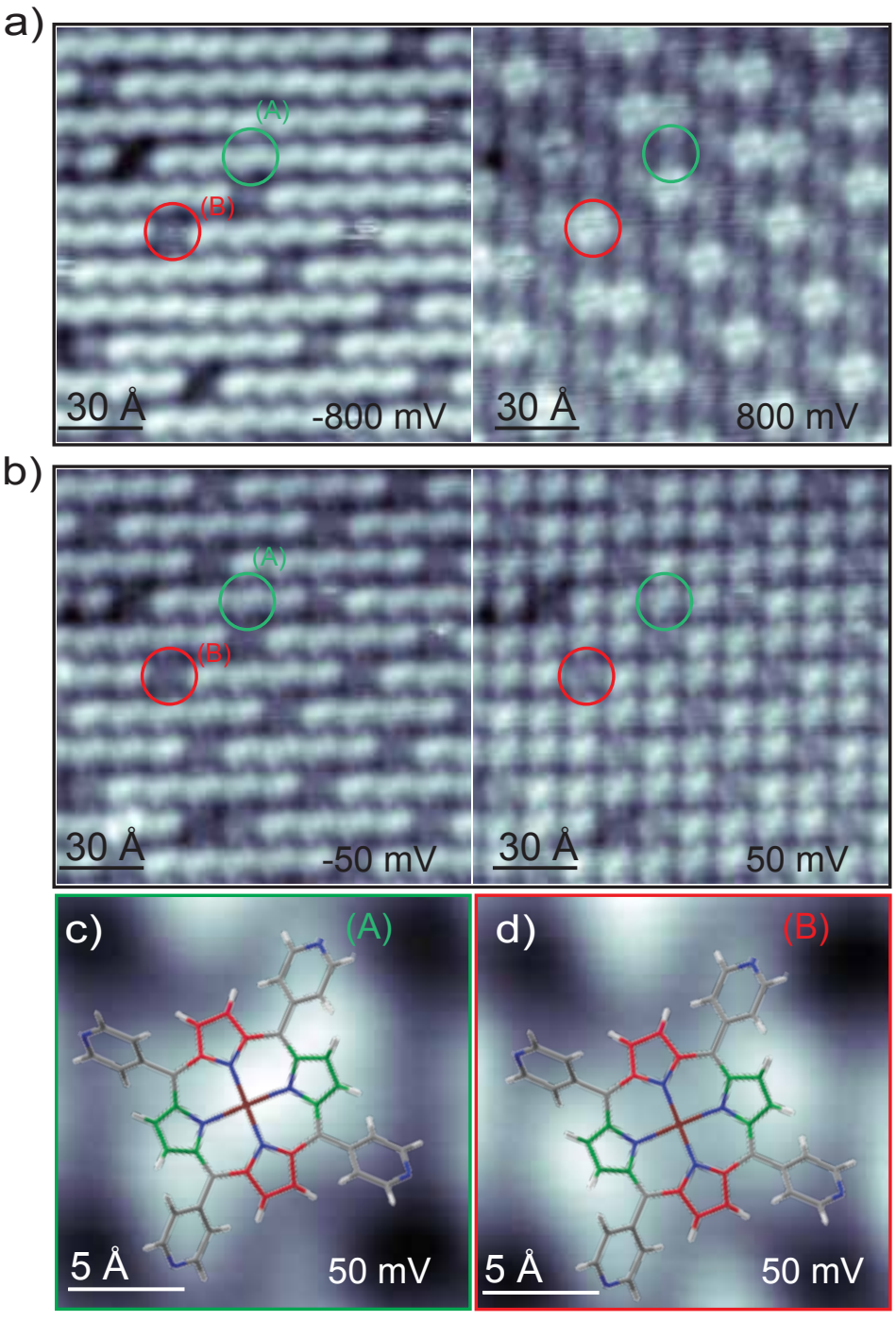

Figure 5.2: a,b) STM images of Fe-TPyP islands at positive and negative bias voltages. Two different types of molecules with different contrasts can be observed: type A and type B molecules marked by green and red circles, respectively. High resolution STM images of c) type A, d) type B molecules (images are taken with $V_{\text{bias}} = 50$ meV). The molecular model is overlaid on top of the STM images.

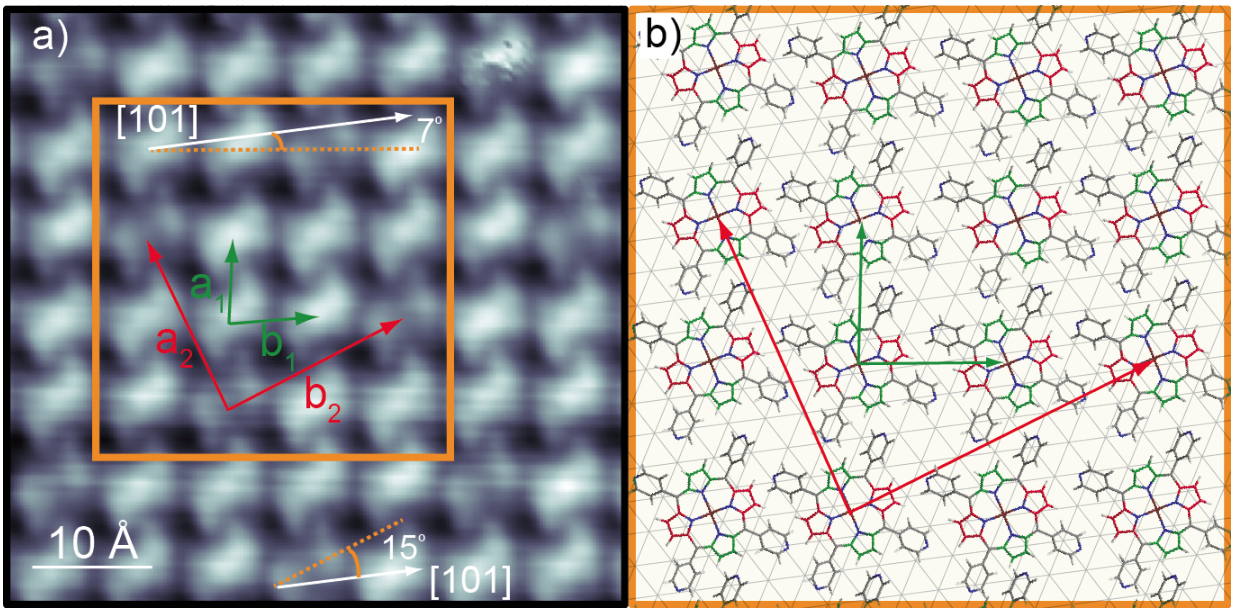

Figure 5.3: a) STM image of Fe-TPyP an island taken at $V_{bias} = 50$ meV. A nearly square molecular arrangement is shown by the green vectors a_1 and b_1 . The superstructure of the type B molecules is shown by the red vectors a_2 and b_2. b) The molecular model of the molecular island, which is indicated by the orange square in (a), is overlaid with the Pb(111) substrate.

opportunity to study the same molecule in different environments. Therefore, in the following, we will focus on the study of the electronic and magnetic properties of each type of molecules, their similarities as well as their differences. In order to understand the fundamental differences between the two types of the molecules in the next sections we will address the following questions: What is the difference between their electronic and magnetic properties? How do the corresponding magnetic properties of each type of the molecules can be correlated with their adsorption sites?

5.3.2 Electronic properties of Fe-TPyP molecules on Pb(111)

In order to study the electronic properties of the Fe-TPyP molecules, we take advantage of the sub-molecular lateral resolution of LT-STM and record dI/dV tunneling spectra on different parts of the molecules. The spatial distribution of the electronic states can be clearly visualized by differential conductance maps, which are recorded at the energies of the corresponding resonances. This allows to compare the localization of these electronic states to the corresponding calculated frontier orbitals of the Fe-TPyP molecule in gas phase.

First, we investigate the properties of both types of molecules at the energy scale of molecular resonances. Fig.5.4(a) shows constant height dI/dV spectra taken on the ligand and on the center of both types of

Fe-TPyP molecules. For type B molecules, the spectrum taken on the ligand exhibits two peaks at 740 meV and 980 meV above E_F (light blue spectrum in Fig.5.4(a)). The spectrum taken on the center of type B molecules shows the same feature but with lower intensity (dark blue spectrum in Fig.5.4(a)).

Subsequently, for type A molecules, the spectrum taken on the ligand exhibits a broad peak at 1.1 eV in addition to a peak with lower intensity at -280 meV (light green spectrum in Fig.5.4(a)). The spectrum taken on the center shows the feature at -280 meV and a trace of the resonance around 1.1 eV that could not be resolved as a peak (dark green spectrum in Fig.5.4(a)). As we have seen in Sec.2.1.3 spectra recorded with the constant height spectroscopic mode have the flaw that a stronger resonance dominates weaker resonances at nearby energies, which makes it difficult to resolve them energetically. One way to overcome this difficulty is to perform constant current dI/dV spectroscopy.

Fig.5.4(b) shows a set of spectra recorded in the constant current mode in the center and on the ligand for both types of molecules. They exhibit a pair of resonances at 725 meV and 940 meV with higher intensity at the ligand. Thus, for type A molecule, the peak at 1.1 eV in constant height mode retains these two peaks that could not been resolved. It is worth to mention that, due to the constant current mode the energies of the resonances are slightly shifted with respect to the energies obtained in constant height mode [28].

The difference between spectra on the ligand and on the center is due to the localization of the frontier molecular orbitals. To investigate their lateral distribution, we mapped the dI/dV signal over both types of molecules at the energies of the resonances. Fig.5.4(d) shows the recorded dI/dV map on a type B molecule at the energy of 700 meV. The lateral distribution of this resonance is very similar to the calculated LUMO for a similar molecule, which has different end groups, iron-tetraphenylporphyrin (Fe-TPP) on Au(111) [151]. This similarity indicates that the underlying substrate as well as the meso-functional groups have a minor effect on the lateral distribution of the LUMO.

We calculated the molecular orbitals of the Fe-TPyP molecule employing the quantum chemistry software Gaussian 09 [155] using DFT based methods. We used the B3PW91 hybrid functional and a split basis set (6-31G* for C, N and H atoms and LANL2DZ pseudo potential for Fe) [156]. Fig.5.5 shows the calculated DOS frontier molecular orbitals under the assumption of a triplet spin state of the molecule. For the Fe-TPyP molecule, different (forced) saddle configurations $\alpha = 12^\circ$ and 60° were considered. The saddle shape is kept constant during the structure optimization and the calculation of the electronic states. Fig.5.5(a,b) shows the spin polarized electronic states of the different saddle shaped Fe-TPyP molecules by assuming arbitrary the Fermi level centered in between the highest occupied molecular orbital (HOMO) and lowest unoccupied molecular orbital (LUMO) (shown as a gray dashed line). Fig.5.4(c) shows some of the (frontier) orbitals labeled as O_{1-7} orbitals.

The lateral distribution of the state at 700 meV of the type B molecule (Fig.5.5(d)) resembles the spatial distribution of the calculated doubly degenerated unoccupied orbitals labeled O_1 and O_2 in Fig.5.5(c). This lateral distribution is very similar to the case of Fe-TPP, which suggest again that the LUMO distribution is

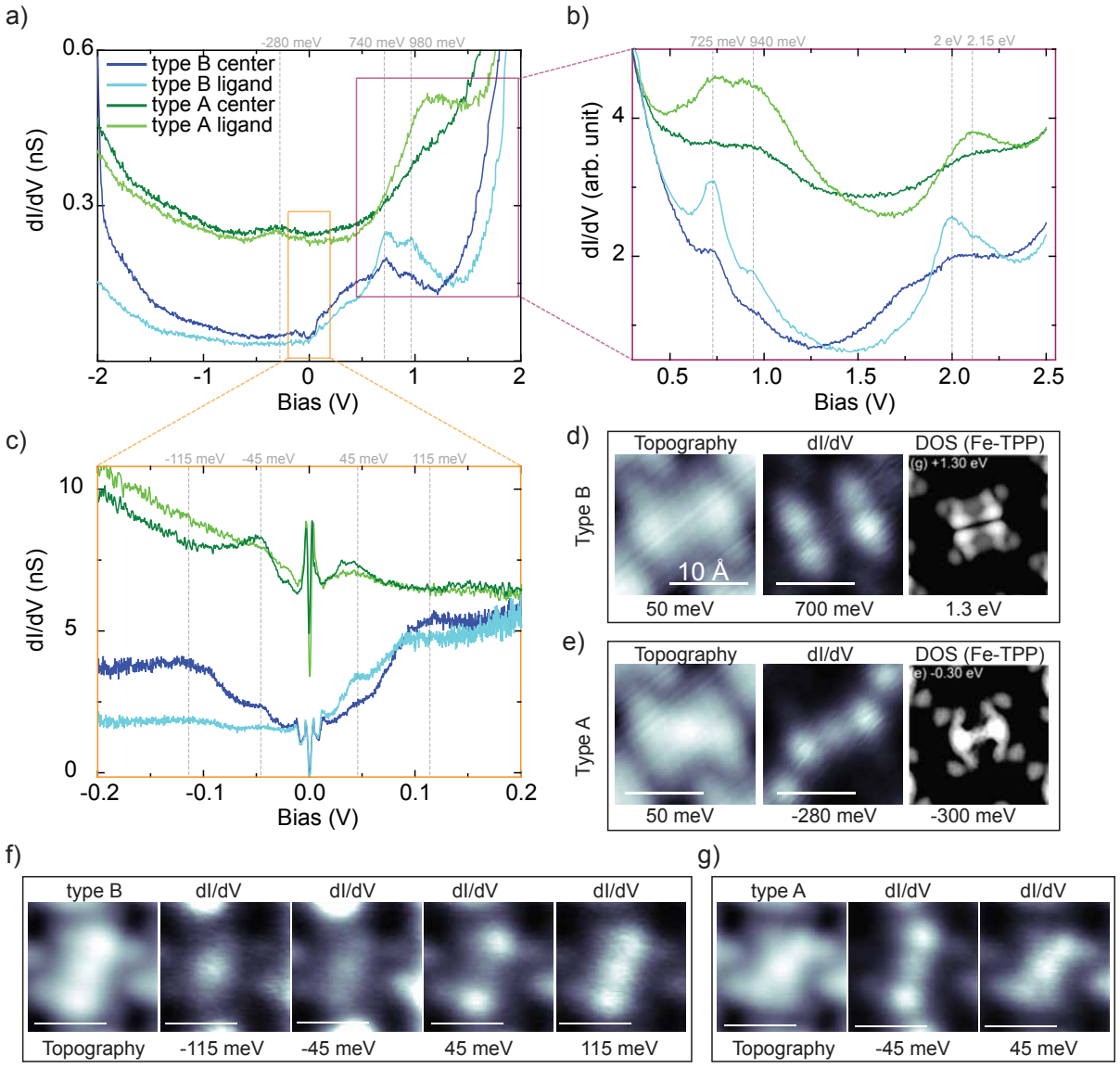

Figure 5.4: a,c) Constant height and b) constant current dI/dV spectra acquired over the center and the ligand of both types of molecules (indicated in the onset of the image). In (a) the feedback opened at $I = 500$ pA and $V_{\text{bias}} = 2$ eV with a modulation of $V_{\text{rms}} = 5$ meV. In (b) the set point is $V_{\text{bias}} = 100$ meV and $I = 500$ pA with a modulation of $V_{\text{rms}} = 1$ meV. In (c) the feedback opened at $I = 500$ pA and $V_{\text{bias}} = 200$ meV with a modulation of $V_{\text{rms}} = 1$ meV). d,e) STM topographic images and constant height dI/dV maps of a type B Fe-TPyP and a type A Fe-TPyP at the energies indicated under the maps. The simulated DOS images of a Fe-TPP on Au(111) at the indicated energies are shown for comparison. DOS images adapted from [151]. f,g) STM topographic images and constant height dI/dV maps of a type B Fe-TPyP molecule and a type A Fe-TPyP molecule taken at different energies as indicated under the maps.

independent of the underlying substrate. The calculated DOS of the two Fe-TPyP molecules with different buckling angles shows that, due to the deformation of the porphyrin macro-cycle, the degeneracy between the LUMO (O_1 and O_2 in Fig.5.5(c)) is lifted. This corresponds to the two peaks at 725 meV and 940 meV of the recorded dI/dV spectra (Fig.5.4(b)) of both types of the molecules.

Fig.5.4(e) represents a dI/dV map at -280 meV of a type A molecule. It shows maximum intensity at the two up tilted pyrrole rings and same intensity of the central iron, consistent with the point spectra taken on the ligand and on the center. This shows some similarities with the calculated HOMO of Fe-TPP on Au(111), [151]. Furthermore, its localization is quite similar to the calculated molecular orbitals O_4 and O_5. However, due to the saddle configuration of the molecules we can only image the O_5 orbital. These orbitals have the character of the π system of the organic macro-cycle as well as of the d_{xz}/d_{yz} orbital of the iron center. However, due to topographic effect of the up-tilted pyrrole in the tunneling experiment, we are only able to resolve the one orbital that is localized on the up-tilted pyrrole.

Moreover, considering the magnetic nature of the Fe center and to reveal any sign of its magnetic properties, we recorded constant height dI/dV spectra at energies close to E_F. Fig.5.4(c) represents the spectra taken on the ligand and on the center of both types of the Fe-TPyP molecules between -200 meV and 200 meV. For type B molecules, the spectrum taken on the iron center exhibits an increase in dI/dV signal at ± 115 meV and ± 45 meV with comparable intensities (dark blue spectrum in Fig.5.4(c)). However, the spectrum taken on the ligand of the type B molecule mainly exhibits the signal at positive bias at similar energies, while the spectrum at negative energies is almost flat (light blue spectrum in Fig.5.4(c)). For type A molecules, the spectra show features at ± 45 meV with their main weight on the ligand of the molecule (dark and light green spectra in Fig.5.4(c)).

To uncover the lateral extension of these features, dI/dV maps at these energies are recorded for both types of molecules. For type B molecules, the feature at 115 meV exhibits a two-fold symmetry and is delocalized over the center and the pyrrole groups (Fig.5.4(f)). By comparing it with calculated molecular orbitals, it resembles the O_4 molecular orbital in addition to the O_7 orbital (Fig.5.5(c)). The feature at 45 meV is localized over the pyrrole groups (Fig.5.4(c)) with a faint signal above the Fe center which indicates a weak character of the O_7. At negative energies, the feature at -115 meV is mainly localized at the center of the molecule. It can, for example, be attributed to the calculated O_7 orbital. Finally, the dI/dV map of the feature at -45 meV shows a more delocalized state with more weight on the central Fe.

For the type A molecule, the state at -45 meV is extended over the central Fe as well as over the macro-cycle of the molecule, very similar to the state at -280 meV for the type A molecule and 45 meV for the type B molecule. However, the state at 45 meV has a different symmetry with more weight on the iron center which might come from other states, *e.g.* the admixture of the O_7 and O_6.

As we have seen in Sec.2.1.3 that vibrations as an inelastic excitation can be seen as a pair of excitations (mainly step-like features) symmetric in energy around the Fermi level. Ohta et.al have investigated iron-phthalocyanine, a similar molecule to Fe-TPyP, on Au(111). They have obtained similar features

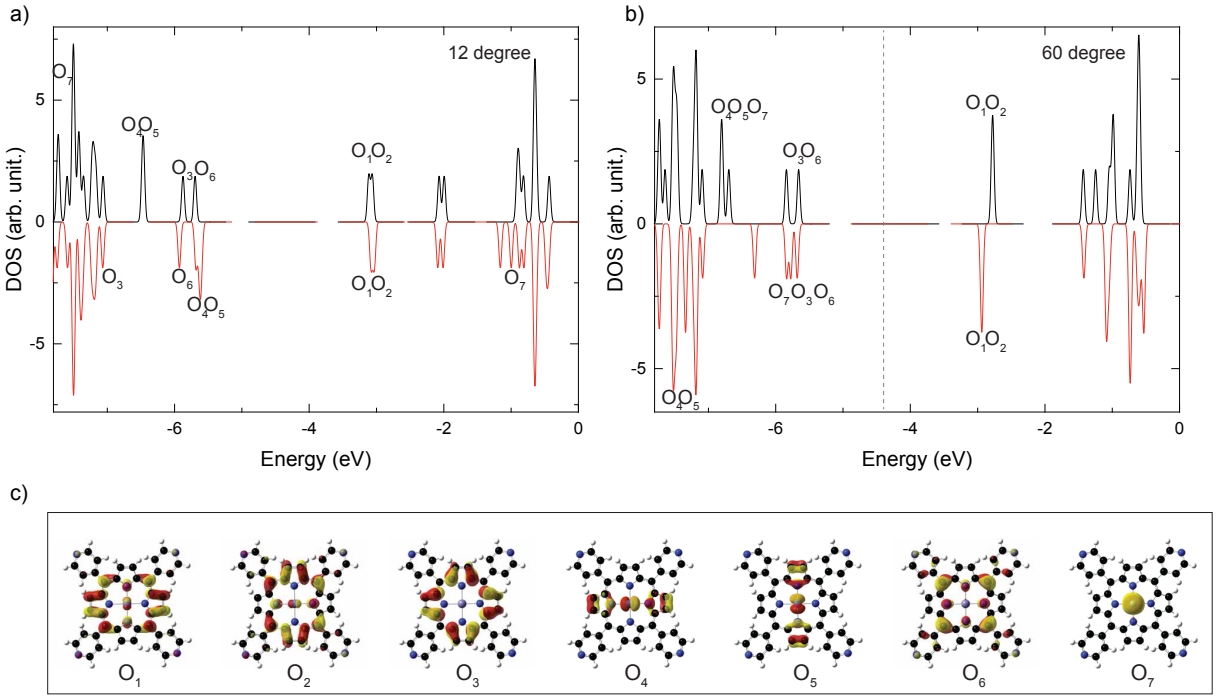

Figure 5.5: a,b) Calculated spin polarized DOS of a saddle shaped Fe-TPyP molecule with different rotational angles of the pyridine group (see in Fig.5.1) a) $\alpha = 12°$ b) $\alpha = 60°$. c) Top view of the calculated (frontier) molecular orbitals labeled O_{1-7}.

in the recorded STS at slightly different energies [157]. They attribute these features to the vibrational modes of the molecule, backed-up by high-resolution electron energy loss spectroscopy [158]. Additionally, our calculation for a Fe-TPyP with $12°$ rotation of the pyridine groups posses similar vibrational modes such that the features at ± 45 meV and ± 115 meV could be assigned to the symmetric and asymmetric stretching modes of Fe-N bond, respectively. However, the localization of the features at $+45$ meV for type B and type A molecules and $+115$ meV for type B molecules are different than the corresponding ones at negative energies. This contradicts the purely vibrational origin for these resonances as their localization is independent of the bias voltage polarity [159]. Furthermore, the localization of the features at ± 45 meV for both types of molecules are different. This is an indication of a more complex nature than the purely electronic or vibrational origin of these features. One possible scenario is to consider these features as a superposition of the DOS of the molecule in addition to the localization of the vibrational mode.

Comparing the calculated DOS of the type B and type A molecules, we see that, depending on the rotational angle of the pyridine group, the frontier molecular orbitals are rearranged. In case of the rotational angle of $12°$, which results in a more deformed porphyrin macro-cycle, the double degeneracy of the LUMO

orbitals is lifted. That is consistent with our spectroscopy for both types of the molecule. Therefore, we can assume that both types of the molecules exhibit the saddle shape which have been reported often for this molecular family [127, 152, 160–162]. Moreover, the similarity of the localization and the symmetry of the feature of type A molecule at -45 meV and the feature of type B molecule at 115 meV suggests that these two features result from the admixture of the same orbitals in addition to vibrational modes.

However, the energy difference of a feature with same localization (-115 meV for type B molecule and 45 meV for type A molecule), indicates different buckling for each type of the molecule which yields the rearrangement of the molecular states. It has to be noted that our calculation is done for a free molecule in gas phase with arbitrary fixed saddle shapes. It is known that slight modifications of the saddle shape would lead to shifts in the energies of the electronic states [142, 152]. Moreover, upon adsorption on the surface, the energy positions of the electronic states might change. This can be understood as following: the surface can act as an extra ligand, thus affecting the energy position of the electronic states. In this case, orbitals with the character of d_{z^2} and d_{xz} / d_{yz} orbitals are more affected due to their extension towards the underlying substrate, that causes stronger hybridization with the surface.

All in all, type A and type B molecules adapt slightly different distortion that might be due to different adsorption sites, which gives rise to different conformations and symmetries. Depending on the symmetry and their hybridization of the orbitals with the underlying substrate, their electronic states are shifted to higher/lower energies. Additionally, the hybridized states between the d-levels and the ligand rearrange and show different localization. Furthermore, the excitation of the vibrational modes becomes more effective due to the orbital assisted tunneling [163, 164].

5.3.3 Magnetic properties of Fe-TPyP molecules on Pb(111)

In the previous parts we have seen that two types of Fe-TPyP molecules exist on Pb(111) due to slightly different hybridization with the underlying substrate which results in different saddle configurations. Spectroscopy revealed that the frontier molecular orbitals of type B and type A molecules originate from hybridized states between the organic ligand and the iron center. However, the energies and the localization of these states are different for each type. In this part, we will focus on the effect of the slightly different distortion of both types of molecules on the magnetic properties and on how the corresponding magnetic fingerprint of the molecules correlates with the electronic properties. To be able to answer these questions, we will study the magnetic properties of both types in the superconducting and the normal state.

Magnetic properties of type B Fe-TPyP molecules: extended spin excitations

Fig.5.6(a) shows two spectra taken at the center (red spectrum) and on the ligand (blue spectrum) of a type B Fe-TPyP molecule in addition to the reference spectrum on pristine Pb (black spectrum). The spectrum on Pb shows the characteristic superconducting gap followed by two sharp resonances at $\pm 2\triangle$

(see Sec.3.1.2). The spectra at the center as well as on the ligand of the molecule exhibit two pairs of resonances in addition to the BCS peaks. Each pair of these resonances is symmetric with respect to E_F at energies of ± 11.3 meV and ± 13.3 meV (shown by two pairs of blue arrows). The differential conductance increases by around 30% after the first excitation as indicated in Fig.5.6(b). Symmetric peaks[1] in the dI/dV signal may indicate inelastic excitations, *i.e.*, spin excitations or vibrations.

In case of a vibrational origin of these excitations, as we have seen in the case of higher-lying excitations as studied in Sec.5.3.2, one expects to observe these peaks also on type A molecules, because they have the same molecular structure. However, the type A molecules do not show such excitations. Furthermore, Heinrich et al. have obtained similar excitations for a similar molecule iron-octaethylporphyrin (Fe-OEP) on Pb(111), which they attribute to spin excitations [165]. Considering the amount of increase of the conductance due to the excitations, the absence of these excitations on type A molecules, and their resemblance with spectra of Fe-OEP on Pb(111), these peaks most likely result from inelastic spin excitations. These spin excitations presumably come from Fe d-orbitals, which are localized in the center of the molecule. However, a spectrum taken on the ligand of a type B molecule exhibits the same excitations. To understand the most probable process that can lead to the presence of spin excitations on the ligand we need to consider the hybridization of Fe d-orbitals with the π system of the molecule. Therefore, by tunneling into these states, energy can be transferred to the Fe-site, resulting in spin excitations.

The origin of these spin excitations can be understood by the following considerations. The Fe^{+2}-center is subject to a molecular ligand field that has a 4-fold symmetry. Fig.5.7 shows the resulting electronic configurations that were reported for similar molecule Iron-tetraphenylporphyrin (Fe-TPP) in bulk [166]. In these electronic configurations of the d-levels, the $d_{x^2-y^2}$ orbital lies higher in energy due to the direct interaction with the nitrogen atoms of the molecule and thus remains unoccupied. The rest of the d-orbitals can have three different arrangements, resulting in three different magnetic configurations: ${}^3A_{2g}((d_{xy})^2,(d_{z^2})^2,(d_{xz}/d_{yz})^2)$, ${}^3B_{2g}((d_{xy})^1,(d_{z^2})^1,(d_{xz}/d_{yz})^4)$ and ${}^3E_g((d_{xy})^2,(d_{z^2})^1,(d_{xz}/d_{yz})^3)$ [126]. On other substrates, depending on the length and angle of the Fe-N bond, the ground state (GS) of the Fe center can be any of these three configurations or even a mixture of them [167, 168]. However, all of them lead to a S=1 system. Furthermore, by placing such a S=1 system in an anisotropic environment, the spin levels $m_S = 0, \pm 1$ are split.

As seen in Sec.3.2.2, in an anisotropic environment spin-orbit coupling causes a splitting of the spin states. In particular, if the d_{xz} and d_{yz} orbitals are degenerate, only axial magnetic anisotropy D exists and its value is inversely proportional to the energy difference between d_{z^2} and the d_{xz} / d_{yz} levels [47]. Furthermore, if this degeneracy is lifted, the system acquires a transverse magnetic anisotropy E, which increases with the splitting of the d_{xz} and d_{yz} levels. In this case, the spin excitations of a S=1 system with $D > 0$ originate from the transition between the ground state $|\phi_0\rangle = |0\rangle$ to the two excited states

[1] The peak line-shape is due to the convolution of the step line-shape of the inelastic excitation and the peak line-shape of the superconducting tip.

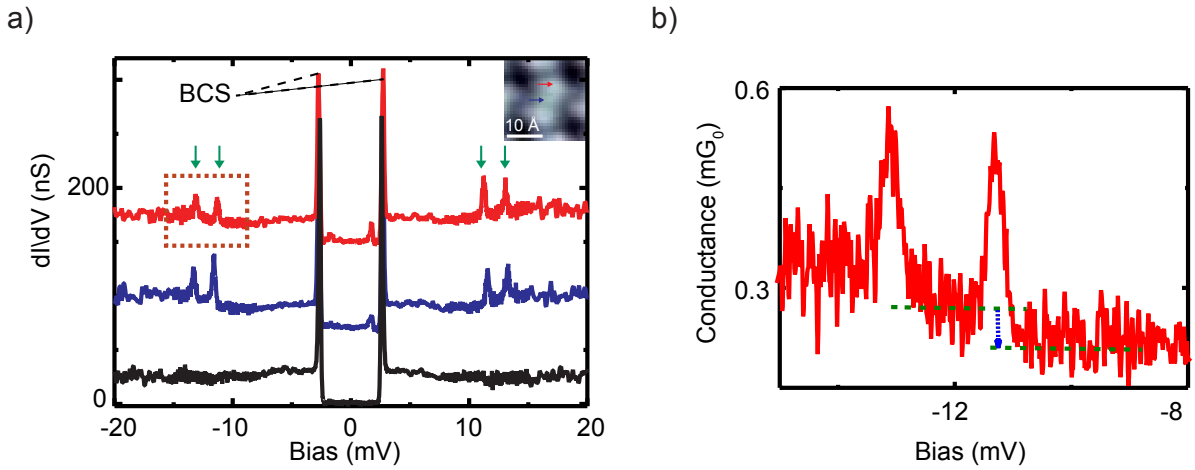

Figure 5.6: a) dI/dV spectra acquired on the center and on the ligand of a type B molecule marked by the arrows in the STM image as well as on pristine Pb(111) (black line). Two pairs of resonances are indicated by green arrows. Two BCS peaks are marked by black dashed lines. b) Zoom in the spin excitation signal shown by the dashed square in (a). The change in the conductance after the first excitation is shown by a blue arrow. The feedback opened at $V_{bias} = 20$ meV and $I = 500$ pA with a modulation of $V_{rms} = 50$ μeV.

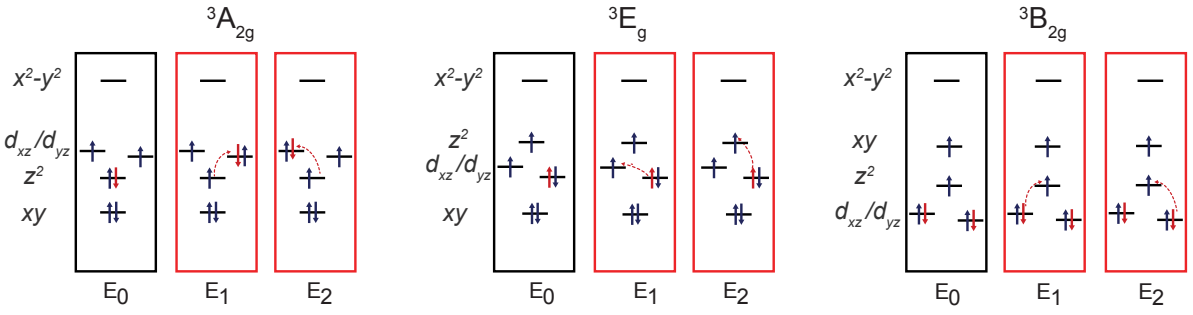

Figure 5.7: Proposed rearrangements of the d-orbitals of the Fe atom. The ground, first and second excited states are labeled by E_0, E_1 and E_2, respectively. The $^3A_{2g}$ configuration is known to have the minimum energy for Fe-TPP in bulk [166]. The $^3B_{2g}$ configuration corresponds to the magnetic configuration of Fe-OEP on Pb(111) reported in [165].

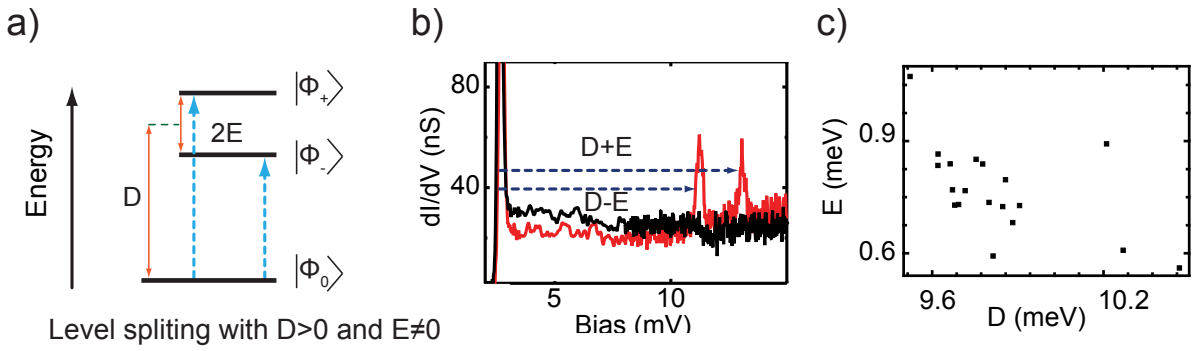

Figure 5.8: a) Energy diagram of the S=1 system with positive axial anisotropy D and non-zero transverse anisotropy E. The three sub-states of the system are represented by $|\phi_0\rangle$ as the ground state and $|\phi_-\rangle$ and $|\phi_+\rangle$ as two excited states. The possible spin excitations are marked by the dashed blue arrows. b) The positive energy part of the spectra show the spin excitations peaks. The corresponding energies of the spin excitations are defined with respect to the BCS gap, as indicated by the dashed blue arrows. c) Distribution of the E and D anisotropy parameters determined for 20 different type B molecules.

$|\phi_-\rangle = \frac{1}{\sqrt{2}}(|+1\rangle - |-1\rangle)$ and $|\phi_+\rangle = \frac{1}{\sqrt{2}}(|+1\rangle + |-1\rangle)$ with same intensities. Fig.5.8(a) shows an energy diagram of such spin excitations with $D \geq 0$ and $E \neq 0$, resulting in two excitations with energies $E_1 = D - E$ and $E_2 = D + E$. Considering the superconducting nature of tip and sample, the energies of the spin excitations are measured with respect to the BCS peaks as shown in Fig.5.8(b).

Fig.5.8(c) shows the scattering of the values of the D and E magnetic anisotropies among different type B molecules. The D anisotropy energy varies by 5% around its average value compared to 30% variation for the E anisotropy. From Sec.5.3, we know that all the type B molecules adapt the same adsorption site. Additionally, the adsorption site mainly effects the d_{z^2} orbital, since this orbital overlaps the most with the substrate. Therefore, the fact that all type B molecules have the same adsorption site can explain the minor variation of the D anisotropy. On the contrary, the E anisotropy arises from the lifting of the degeneracy of the d_{xz}/d_{yz} orbital that is caused by the distortion of the molecule. Therefore, small changes of the saddle configuration of a type B molecule can give rise to important variations of the E anisotropy.

It is necessary to mention that, by considering the positive sign of the axial anisotropy that was determined in the experiment, only the ${}^3A_{2g}$ and ${}^3B_{2g}$ electronic configurations remain potential ground states. The ${}^3E_g$ on the other hand, would result in a negative value for D due to the existence of higher unquenched angular momentum along the z direction than the one perpendicular to it [47].

One way to prove the magnetic origin of the inelastic excitations is to study the behavior of such excitations under the influence of an external magnetic field. The external magnetic field will shift the excitation energy according to the Zeeman energy $\mathrm{E_{Zeeman}} = g\mu_B B S_z$ [169]. Fig.5.9 shows the spectrum

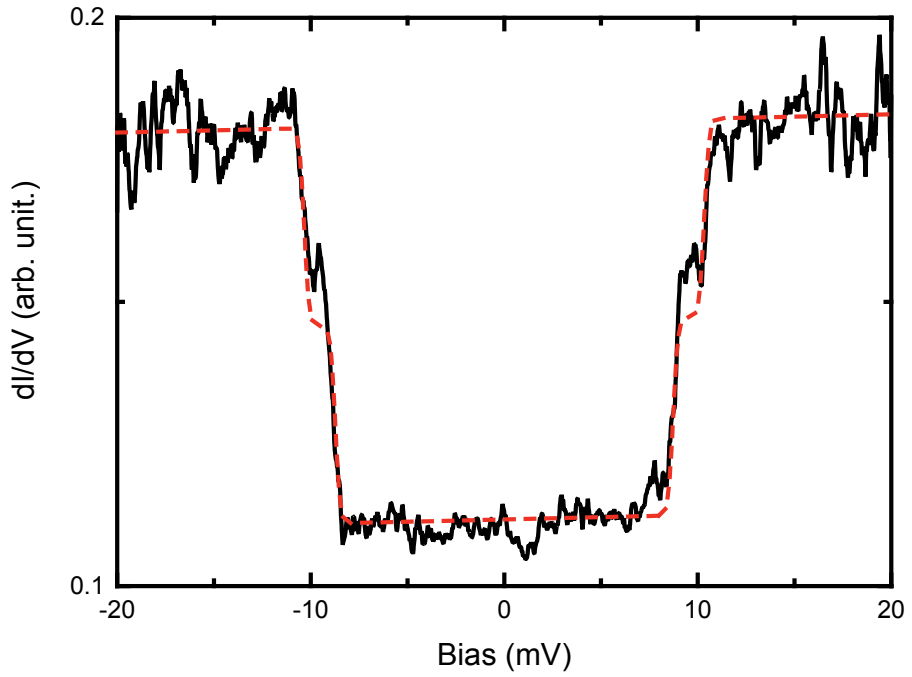

Figure 5.9: dI/dV spectrum acquired on the center of a type B molecule in the normal state. The feedback opened at $V_{\text{bias}} = 20$ meV and $I = 500$ pA with a modulation of $V_{\text{rms}} = 50$ μeV. An external magnetic field of 1.2 T is applied perpendicular to the sample to quench the superconductivity of the sample and the tip. Fitting of S=1 system with D and E anisotropy is shown by the dashed red line.

taken on the center of a type B molecule under an external magnetic field of 1.2 T. The fit under consideration of a S=1 system is shown by a dashed red line, and reproduces fairly well the experimental data. Under an external magnetic field of 3 T, the Zeeman shift of the spin excitations is around 150 μeV which is beyond our resolution ($\sim$ 300 μeV). Thus, we were not able to resolve any shift of the spin excitation in a magnetic field.

To probe the lateral extension of the spin excitations, we recorded dI/dV spectra along the up-tilted pyrrole groups of the molecule (in absence of B-field). Fig.5.10 shows the 2D color plot of these spectra as indicated by a line in the topographic image in Fig.5.10. Interestingly, the energies of the spin excitations vary along the main axis of the molecule. Their energy is higher above the center than above the ligand. It is worth mentioning that the intensity of the first and the second excitation vary slightly over the molecule and differ from each other. For instance, in the case of the spectra taken on the ligand, the intensity of the first and second excitation is very similar at negative energies, while at positive energies, the intensity of the second excitation is smaller than the first one.

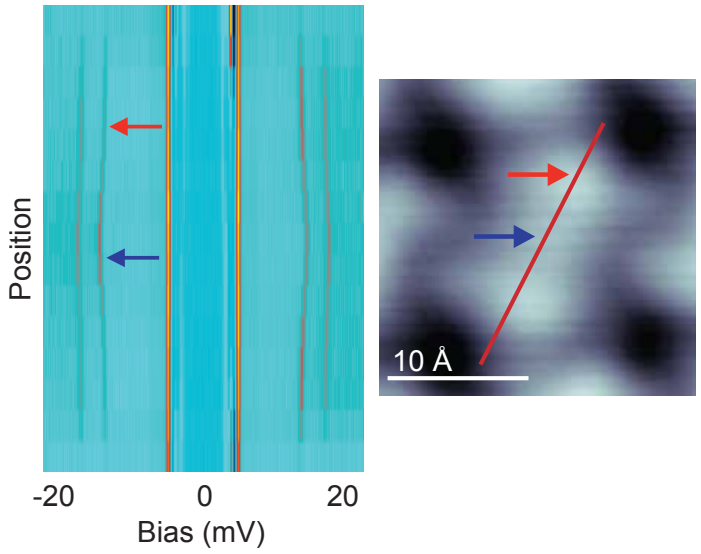

Figure 5.10: False 2D color plot of multiple spectra recorded along the red line shown in the STM image. The line goes along the main axis of a type B molecule. The center and the pyrrole ring are marked by the blue and red arrows, respectively in the STM image and in the 2D plot. The feedback opened at $V_{\text{bias}} = 20$ meV and $I = 500$ pA with a modulation of $V_{\text{rms}} = 50$ μeV.

Manipulation of the magnetic anisotropies: the influence of the tip The variation of the energies of the spin excitations over the molecule can be caused by the presence of the tip, *i.e.* by the electric field imposed by the bias voltage. To characterize the influence of the tip on the spin excitations, we measured at different tip-molecule distances. For all spectra, the feedback was opened at $V_{bias} = 20$ meV and $I = 500$ pA and the tip height was varied by Δz as indicated in Fig.5.11 (negative numbers correspond to moving the tip towards the surface). Fig.5.11(a) shows, as a 2D color plot, a set of spectra taken above the center of the molecule at different tip-molecule distances. In total the tip-sample distance is varied by 200 pm. The energy of the spin excitations increases upon approaching the tip up to $\Delta z = -100$ pm. This corresponds to an increase of D and a decrease of the E anisotropy (Fig.5.11(b)). Approaching the tip even further towards the surface causes instability in the junction. This can be seen in the corresponding *I*(z) signal shown in Fig.5.11(c). One can see an exponential increase of the tunneling current with the distance up to $\Delta z = -80$ pm that corresponds to the tunneling regime. By approaching the tip further, the current shows a sudden jump at $\Delta z = -90$ pm: this is the jump to contact between the tip and sample.

Fig.5.11(d,e,f) shows the result of the same experiment performed on the ligand of a type B molecule with an overall variation of the tip height of 320 pm. Similarly to what is observed above the center, the energy of the spin excitations is increasing with decreasing the tip-sample distance up to $\Delta z = -100$ pm, which corresponds to an increase of D and a decrease of E anisotropy. By approaching the tip further

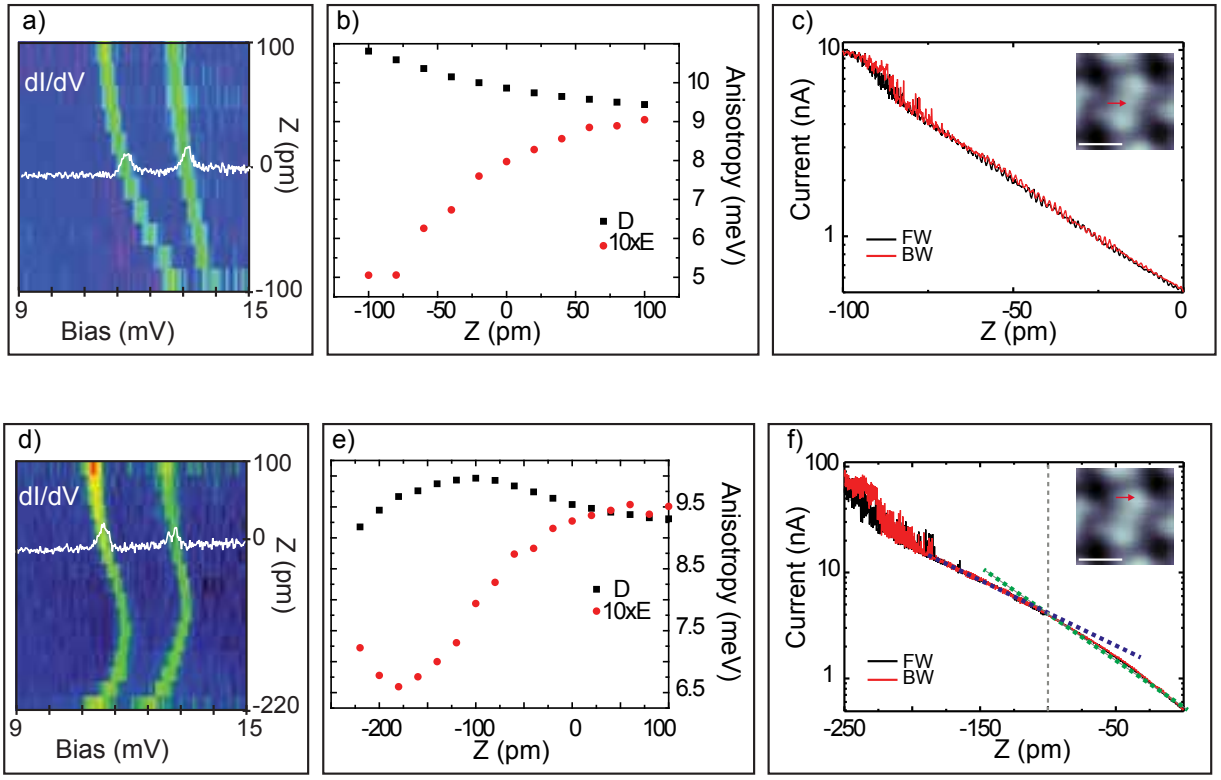

Figure 5.11: False 2D color plot of dI/dV spectra at different tip-sample distances, with decreasing tip-sample distance from top to bottom for a) center d) ligand (indicated by red arrow in onset STM image) of a B type molecule. The approach steps between the spectra are 10 pm. Extracted D and E anisotropy at different tip-sample distances of b) center e) ligand. Tunneling current vs. relative tip approach of c) center and f) ligand. The feedback opened at $V_{bias} = 20$ meV and $I = 500$ pA with a modulation of $V_{rms} = 50$ μeV.

towards the sample up to $\Delta z = -220$ pm, the spin excitations shift to lower energy such that D decreases and E starts to increase again with a minimum at the $\Delta z = -180$ pm. This behavior is very similar to the case of Fe-OEP on Pb(111) [165]. Approaching the tip even more towards the surface causes instability in the junction.

The corresponding tunneling current exhibits characteristic variations (Fig.5.11(f)). Up to $\Delta z = -100$ pm (indicated grey dashed line) it has an exponential increase which is attributed to the tunneling regime (indicated with the green dashed line). Upon further approach of the tip, the slope of the exponential increase of the tunneling current changes, which corresponds to an increase in conductance but still to a tunneling regime (indicated with purple dashed line). This might come from the fact that the pyrrole ring is flexible and thus moves towards the substrate due to the repulsive force that is exerted from the tip. Finally,

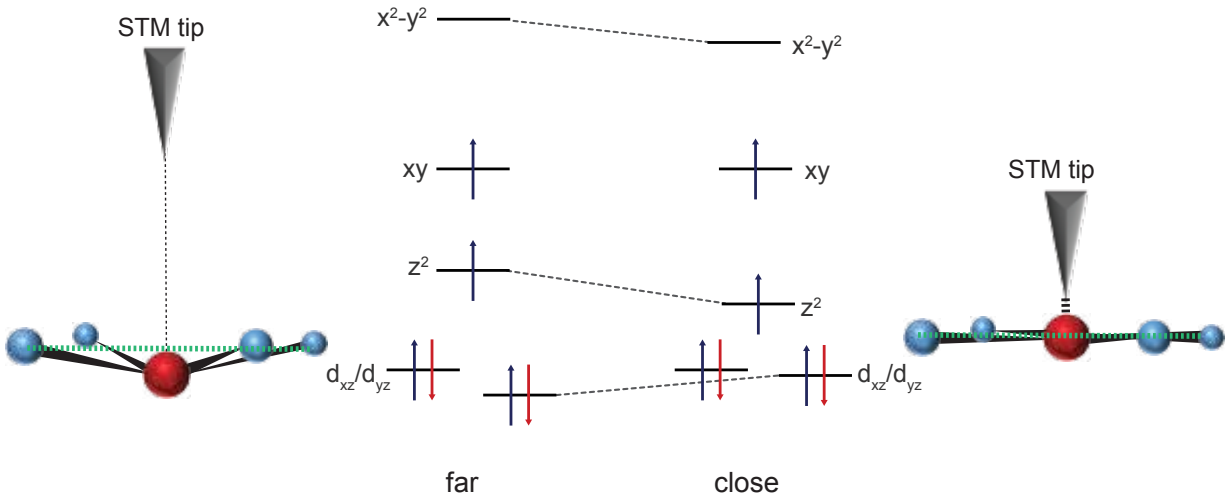

Figure 5.12: Proposed model of the Fe and N atoms in a pyramidal ligand field with 4-fold symmetry. At far distances, the Fe atom is positioned well below the molecular plane as indicated by the green dashed line. The ${}^3B_{2g}$ d level arrangement shown as an example (similar to the Fe-OEP on Pb(111) [165]). By approaching the tip towards the sample, the Fe atom is pulled up and the Fe-N atoms adapt the square planar ligand field. The $d_{x^2-y^2}$ and d_{z^2} orbitals shift to lower energy. The energy difference between d_{xz} and d_{yz} orbitals is reduced.

at a distance around $\Delta z = -220$ pm the tunneling current fluctuates and the tunnel junction is getting unstable.

To explain the mechanism of these changes, we propose a model based on the changes of the Fe-N bond length and its corresponding effect on electronic and magnetic properties [165]. Fig.5.12 shows the ${}^3B_{2g}$ (see Fig.5.7) rearrangement of the d-levels of the Fe center of the Fe-TPyP type B molecule, at far and close tip-sample distances, similar to the level arrangement of Fe-OEP [165]. At far distance, the influence of the tip is minor, thus the molecule is relaxed and the configuration corresponds to the one calculated for the gas phase (see Fig.5.12). We assumed that due to the saddle configuration of the Fe-TPyP molecule, the Fe lies below the molecular plane [139, 165]. By approaching the tip towards the Fe center, the tip exposes an attractive force to the Fe center. Consequently, the Fe atom is pulled out (Fe-surface distance decreased) and the Fe-N bond length decreased. This causes the down shift of the $d_{x^2-y^2}$ and the d_{z^2} orbitals. Additionally, the distortion of the Fe-N cage is reduced, which causes a reduction of the energy difference between the d_{xz} and d_{yz} orbitals. The down shift of the d_{z^2} orbitals reduces the energy difference between the ground state and excited state of the Fe center and, thus, increases the D anisotropy (see Sec.3.2.2). Moreover, reducing the energy difference between the d_{xz} and d_{yz} orbitals causes more

overlap between these orbitals and decreases the E anisotropy.

The proposed model above only considers the atomic d-levels and in case of Fe-TPyP the localization of the orbitals is far beyond the simple atomic orbital picture. Hence, studying the influence of the tip in the case of the ligand is harder to characterize. Surprisingly, the evolution of the D anisotropy is very similar to the case of Fe-OEP on Pb(111), which has been attributed to the rearrangement of the d-orbitals under the influence of the tip. Similarly to the center of the molecule (previous part) and as well as to the Fe-OEP on Pb(111), there are two successive regimes with increasing of D / decreasing of E and then decreasing of D / increasing of E. It is known that the effective forces between the tip and sample depend on their distance. At far distances the long-range attractive forces, *e.g.* Van der Waals forces are dominant [170]. Moreover, these forces originate not only from the atom of the tip apex but also from the other parts of the tip. Therefore, at first place these forces attract the Fe center and change the Fe-N bond such the D anisotropy increases, similar to the case of approaching to the Fe center. However, at closer distances, the repulsive forces predominate and the Fe center will be pushed down. Spontaneously, the bond length of Fe-N changes in favor of decreasing the D anisotropy. The overall behavior of the magnetic anisotropy under the variation of the tip-sample distance is very similar to the case of Fe-OEP on Pb(111) [165].

To conclude, type B molecules exhibit spin excitations that are delocalized over the entire molecule. We observe minor variations of the spin excitation energies among different type B molecules, which is in accordance with the assumption of a same adsorption site that yields same saddle configuration. Moreover, to explain the energy changes of the spin excitations upon tip approach, we proposed a model based on the modification of the ligand field due to the interaction between the Fe center and the tip that could reproduce the variations of the D and E anisotropy parameters.

Magnetic properties of type A Fe-TPyP molecules

In this part, we focus on the type A molecules to study their magnetic properties. We perform the conductance measurements on different parts of the molecules in the superconducting and normal state. The spectra do not show signatures of inelastic excitation as seen in the above section for type B molecules. Instead, they show signatures of magnetic coupling with the superconducting substrate, as will be discussed in detail in the following.

Extension of Shiba states Fig.5.13(a) shows spectra taken on the center (blue) and on the ligand (red) of a type A molecule and also on the underlying substrate as a reference (black). The spectrum on Pb shows a split sharp resonance at 2.75 meV (see the dashed lines in Fig.5.13(a), marking the two gaps Δ_1 and Δ_2) which are attributed to tunneling between the BCS DOS of the tip and the double superconducting gap of sample (see Sec.3.1.2) [43]. The spectrum taken on the center of the molecule (blue), in addition to the BCS peaks, exhibits a pair of intense peaks (150-200 μeV full width at half maximum) inside the superconducting gap (labeled as $\beta_{\pm}$). This pair of intense peaks is attributed to so called Yu-Shiba-Rusinov

(YSR) resonances which will be referred to as Shiba state for simplicity. As discussed in Sec.3.2.4, Shiba states are an expression of exchange coupling of a magnetic moment with the superconductor. The energies of these peaks $\beta_{\pm}$ are symmetric with respect to the E_F located at ± 1.76 meV. Due to the convolution of the DOS of the tip with the sample, after deducting the DOS of the tip, the energy of the Shiba state is $\mathrm{E_S} = \pm 400$ μeV. The intensity of these peaks is asymmetric. The spectrum taken on the ligand also shows the resonances at the same energy but with different intensities. To see the evolution of these peaks over the

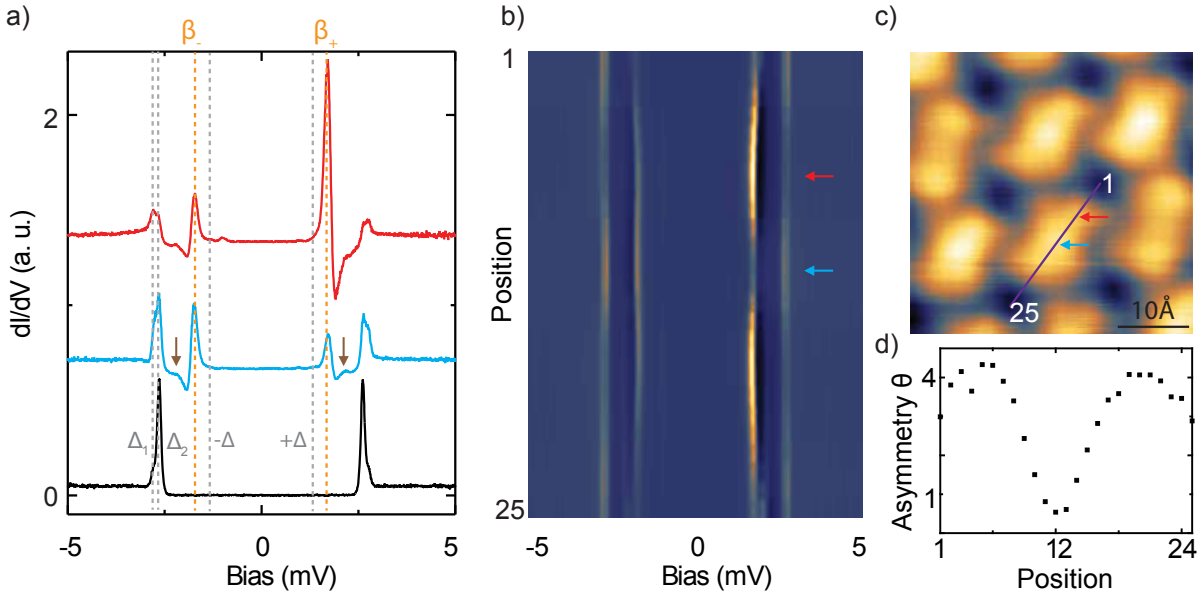

Figure 5.13: a) dI/dV spectra acquired on the center (blue) and on the ligand (red) of a type A molecule indicated by blue and red arrows in (b and c), respectively and the clean Pb(111) surface (black). The feedback opened at $I = 500$ pA and $V_{\mathrm{bias}} = 5$ meV with a modulation of $V_{\mathrm{rms}} = 15$ μeV. b) False 2D color plot of dI/dV spectra along a type A molecule as indicated by a line in (c). c) STM image of Fe-TPyP island. d) Calculated asymmetry ratio of the intensity of hole-like to the intensity of electron-like quasi-particles (intensity(β_+)/intensityβ_-) along a type A molecule as indicated by the line in (c).

molecule we performed spectroscopy along its main axis (indicated by a line in Fig.5.13(c)). The spectra are presented as a 2D color plot in Fig.5.13(b). As one can see, the energy of the Shiba state stays constant. Furthermore, the spectrum taken on the ligand (red spectrum in Fig.5.13(a)) shows that the intensity of the peak at positive energy (β_+) is higher than the one at negative energy (β_-). This intensity difference is inverted in the case of the center (blue spectrum in Fig.5.13(a)). To investigate the variation of this intensity change, we introduce θ as the ratio between the intensity of β_+ to the intensity of the peak at β_-. Fig.5.13(d) shows the change of the intensity ratio parameter, θ, along the main axis of the molecule. It exhibits a minimum in the center and two maxima on the up-tilted pyrrole groups. Additionally, two peaks with very weak intensity that are symmetric in energy with respect to the Fermi level can be seen (shown

with two arrows in Fig.5.13(a)). These peaks are the trace of a Shiba state that comes from the neighboring molecule and will be discussed in detail in the following.

It is worth to mention that the BCS peaks of the spectra taken along the type A molecule exhibit an asymmetry in intensity such that the intensity of the BCS peak at negative energy is higher than the one at positive energy (Fig.5.13(a,b)). The existence of a Shiba state with an energy close to the gap energy such that it cannot be resolved separately can give rise to such asymmetry in the intensity of the BCS peaks.

Spin $\frac{1}{2}$ scattering centers have been discussed intensively in the literature [38]. These can only give rise to one pair of Shiba resonances. However, multiple Shiba states have been observed in case of adatoms and metal-organic molecules on superconductors [15–17, 39, 171]. These multiplicities have been assigned to different origins: (1) Different angular momentum scattering channels, *e.g.* $l = 0, 1, 2$ [15]. (2) Individual scattering potentials from different d-orbitals which are split by the crystal field [39, 171]. The exchange scattering strength of each d-orbital is then determined by its overlap with the underlying substrate. (3) Excitations to different spin levels due to magnetic anisotropy [17, 172]. In this case, depending on the value of the magnetic anisotropy spin can have different levels and their energy splitting is determined by the magnetic anisotropy. Here, contrary to single atoms on surface, the Fe center is separated from the surface due to the organic ligand. Moreover, by assuming that the d-orbitals of the Fe center are arranged similarly to the ones of type B molecules, only d_{xy} and d_{z^2} orbitals contain unpaired electrons. In this case, due to the symmetry, the d_{z^2} orbital points towards the underlying substrate and thus, overlaps with the orbitals of the underlying Pb substrate the most. However, the d_{xy} orbital mainly points towards the organic macrocycle and thus, overlaps very weakly with the underlying substrate. Therefore, d_{z^2} and d_{xy} orbitals can be the origin of the Shiba state inside the superconducting gap and the one at the gap energy, respectively. We thus consider the (2) as a likely scenario. If the magnetic anisotropy was at the origin of the two Shiba states, the D anisotropy value of 9.5 meV obtained from type B molecules would be much higher than the gap energy. Hence we rule out this possibility [17].

To investigate the variation of the Shiba state among different type A molecules, we performed tunneling spectroscopy on 21 different type A molecules. Fig.5.14(a,b) shows as false 2D color plots of spectra taken on their center and on their ligand, respectively. The spectra are ordered according to the energy of the Shiba resonance. All the investigated molecules exhibit a clearly resolvable Shiba state inside the superconducting gap in addition to the asymmetric BCS peaks. The energy of the Shiba state varies between 375μeV to 900μeV. The variation of the Shiba state energy is an indication of different magnetic coupling between the Fe-TPyP molecules and the underlying substrate. Indeed, by adapting different adsorption sites, the molecules can have different magnetic coupling strength [16, 17]. Three exemplary spectra with different Shiba state energies are shown in Fig.5.14(c), corresponding to the three points in Fig.5.14(b) indicated by dashed lines. Additionally, the intensity shows the same asymmetric behavior as in Fig.5.13.

The variation of the magnetic coupling strength of type A molecules to the substrate can originate from corresponding different adsorption sites. To reveal possible patterns of the adsorption sites of the

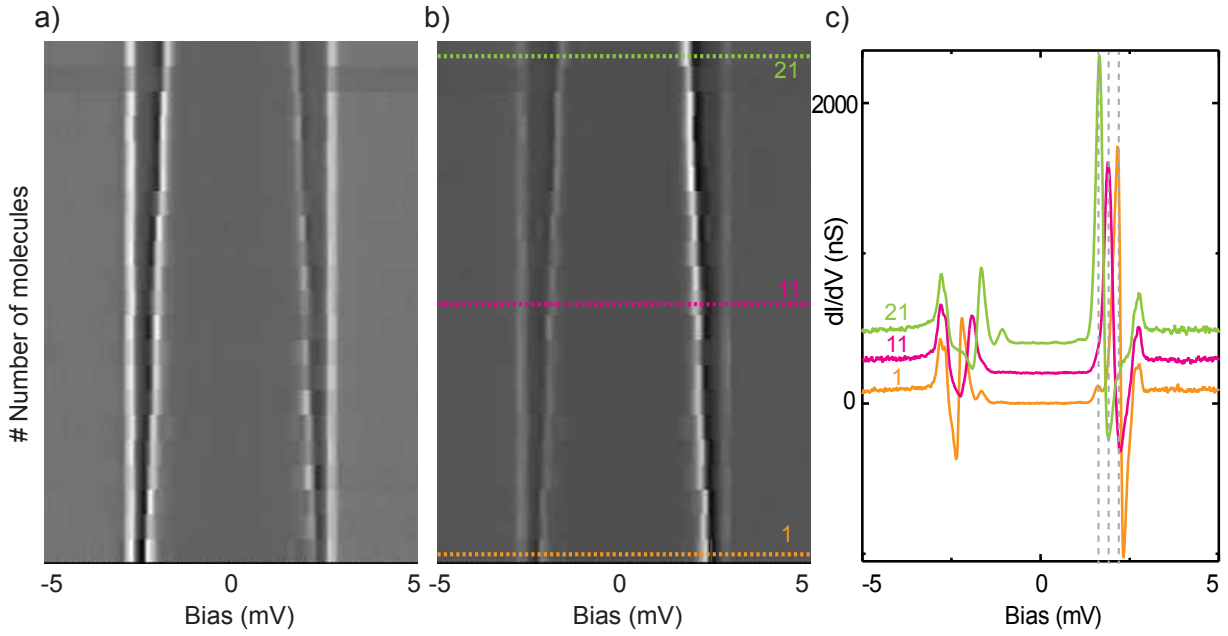

Figure 5.14: 2D color plots of dI/dV spectra taken a) on the center b) on the ligand of 21 different type A molecules in a molecular island. The spectra are ordered according to the energy of the Shiba state. c) Three dI/dV spectra acquired on the ligand of three type A molecules indicated by the dashed lines in (b). The feedback opened at $I = 500$ pA and $V_{\mathrm{bias}} = 5$ meV with a modulation of $V_{\mathrm{rms}} = 15$ μeV.

type A molecules with respect to the substrate, we recorded constant height tunneling current images at the energy of some of the Shiba states (shown on top of the images in Fig.5.15). However, we found no correlation between the localization of the Shiba states at different energies and the underlying substrate. The adsorption sites of type A molecules are hence randomly distributed in a agreement with the model in Sec.5.3.

Considering the extension of the Shiba resonance over the whole type A molecules, we study the possible influence of neighboring molecules. Fig.5.16(c) shows the 2D color plot of spectra taken along a line across three type A molecules in a molecular island (shown by green dotted line in Fig.5.16(a)). The spectra taken on the centers of the three type A molecules and between two neighboring molecules are shown in Fig.5.16(b). We detect no sign of perturbation of a Shiba state by a neighboring molecule, as *e.g.* a splitting or shift. Additionally, the intensity of the Shiba state varies smoothly along the line. Therefore, we can conclude that the Shiba states from neighboring molecules are not coupled to each other. Only a weak trace of a Shiba state from neighboring molecules can be detected in addition to the original Shiba state. This can, for instance, be seen in Fig.5.13(a) where the faint resonances are indicated by two arrows. This observation is in agreement with the spatial extension of the Shiba wave function in the Pb substrate [39]. Moreover, the asymmetry of the BCS peaks is enhanced on the transition point between

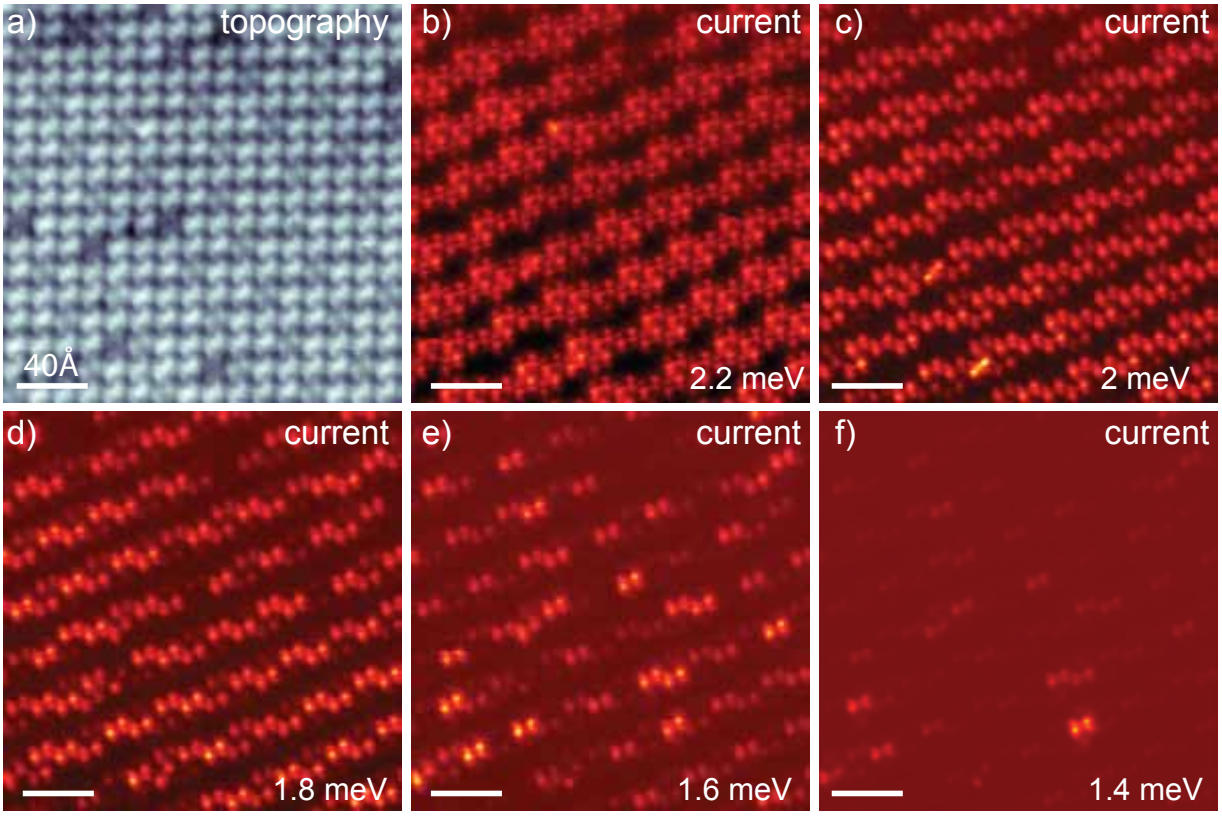

Figure 5.15: a) Constant-current STM image of a Fe-TPyP island ($I = 50$ pA, $V_{\text{bias}} = 50$ meV). b-f) Corresponding constant-height current images recorded at different Shiba states energy values indicated on each image. The feedback opened at the Shiba states energy values ($V_{\text{bias}} = 2.2, 2.0, 1.8, 1.6, 1.4$ meV) and $I = 100$ pA.

molecules. Considering the variation of the tip-sample distance due to the adjustment of the feedback for each spectrum point, this variation might be due to the influence of the tip.

Evolution of Shiba states upon tip approach and quantum phase transition We have seen that for type B molecules (Sec.5.3.3), the presence of the tip changes the magnetic coupling strength between the molecule and the underlying substrate. Therefore, we want to investigate the influence of the tip on the magnetic properties of type A molecules by changing the distance between the tip and the molecule.

Fig.5.17 shows the result of approaching the tip towards the center of a type A molecule. For all spectra, the feedback was opened at $V_{\text{bias}} = 5$ meV and $I = 500$ pA and the tip height was varied by Δz as mentioned in the caption (negative numbers correspond to moving the tip towards the surface). Fig.5.17(a) shows four exemplary spectra recorded on the center of the type A molecule at four different distances (indicated by dashed lines in Fig. 5.17(b)). The complete set of spectra is shown as a 2D color plot in

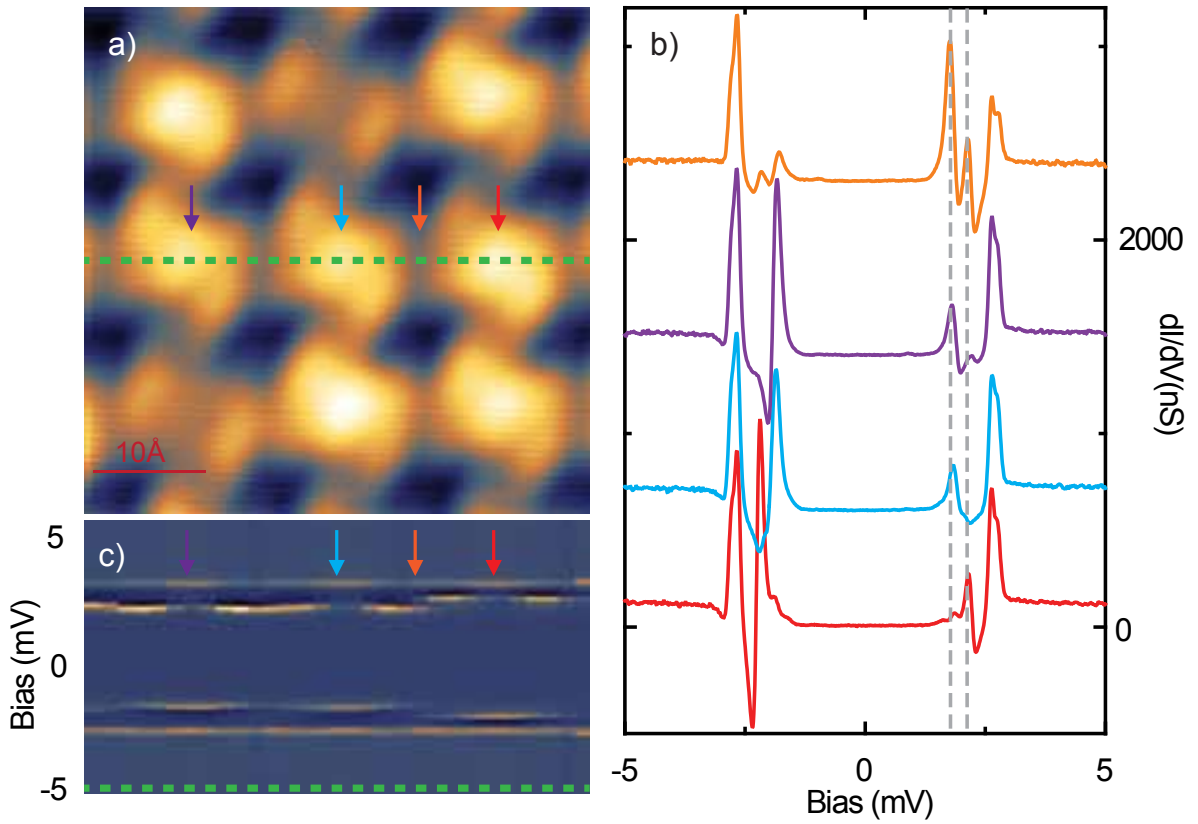

Figure 5.16: a) STM image of a Fe-TPyP molecular island. b) dI/dV spectra acquired on the centers of three neighboring type A molecules and between them as indicated by the arrows in (a). c) False 2D color plot of dI/dV spectra taken along the dashed line in (a). The feedback opened at $I = 500$ pA and $V_{\mathrm{bias}} = 5$ meV with a modulation of $V_{\mathrm{rms}} = 15$ μeV.

Fig.5.17(b) with a total variation of the tip height by 200 pm. Fig.5.17(c) represents the extracted Shiba state energy at each distance, which shifts upon approach by $\sim$ 400 μeV towards the superconducting gap edge. To investigate the evolution of the conductance under tip approach, we recorded the current at different tip-sample distances (Fig.5.17(d)).

Considering the variation of the energy of the Shiba state, the molecule experiences two distinct regimes, which can be tuned by approaching the tip to the molecule. To correlate the behavior of the Shiba states to the influence of the tip, we first record I(z) spectra. These exhibit distinct regimes as can be seen in Fig.5.17(d). The exponential increase of the I(z) signal by approaching the tip up to $\Delta z = -60$ pm is followed by a drastic increase of current up to $\Delta z = -90$ pm which is attributed to the attraction of the Fe center. Upon further approach, the tip contacts the Fe center and can be seen as a plateau in conductance. In the first regime (tip height up to $\Delta z = -90$ pm) the energy of the Shiba state increases towards the

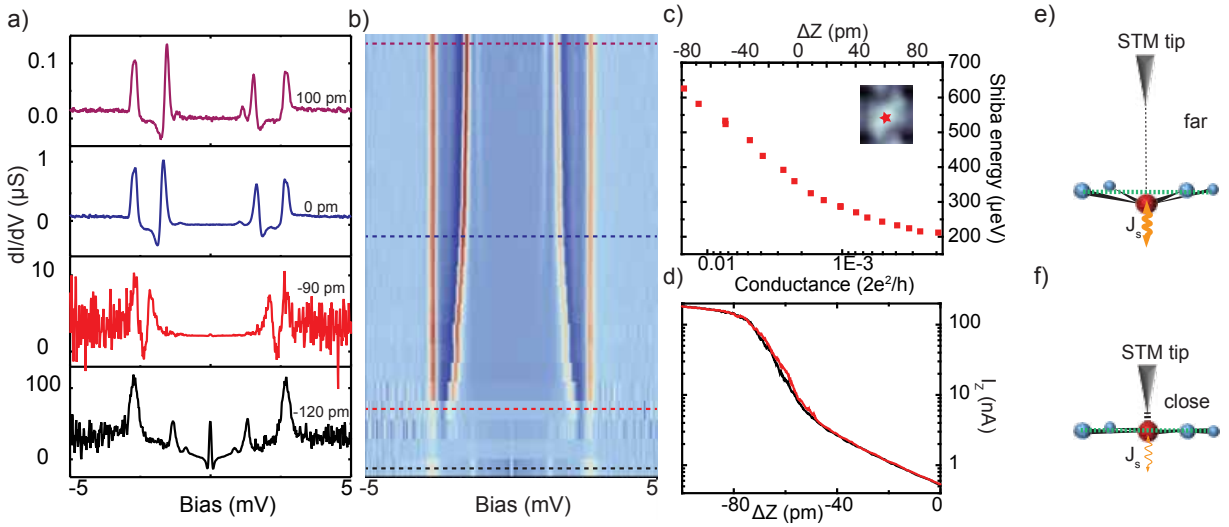

Figure 5.17: a) Four dI/dV spectra acquired on the center of a type A molecule at different tip-molecule distances indicated by the dashed lines in (b). b) False 2D color plot of dI/dV spectra at different tip-sample distances, with decreasing tip-sample distance from top to bottom. Steps between each spectrum are 10 pm. The feedback opened at $I = 500$ pA and $V_{\text{bias}} = 5$ meV with a modulation of $V_{\text{rms}} = 50$ μeV. c) The energy of the Shiba state extracted from the spectra at different tip-sample distances (conductance). d) Tunneling current vs. relative tip approach on the Fe center. The feedback opened at $I = 500$ pA and $V_{\text{bias}} = 5$ meV. Sketch of the proposed model of the tip influence on the relative position of the Fe center in respect to the molecular plane e) at far tip position, the Fe falls below the molecular plan. The exchange scattering strength is relatively strong (orange spiral arrow). f) At the point that the tip is close to the sample, the tip attracts the Fe resulting a rather less distorted molecule. The exchange scattering strength J is weakened by pulling up the Fe center (orange spiral arrow).

superconducting gap edge. In the second regime, the Shiba state vanishes and the characteristic Andreev reflection peaks at $\pm\Delta$ in addition to the DC Josephson peak at E_F arise [173, 174].

To understand the mechanism behind this evolution, we use the same model as in Sec.5.3.3 for the type B molecules. We assumed a porphyrin macro-cycle with four-fold symmetry that is mimicked by Fe bonds to the four nitrogen atoms such as sketched in Fig.5.17(e). When the tip is far away, the Fe center is below the porphyrin plane due to the attractive interaction with the surface. By approaching the tip towards the center of the molecule, the Fe center is attracted towards the tip, resulting in a decrease of the coupling to the substrate (shown by orange spiral arrows in Fig.5.17(e,f)). Under the assumption that the ground state of the Shiba state is a *free spin*, by decreasing the coupling strength to the underlying substrate, the energy of the Shiba state shifts to lower excitation energy which corresponds to the Shiba state being closer to the superconducting gap edge [13, 71, 72, 74, 175]. At the saturated conductance point ($\Delta z = -90$ meV), which might be a sign of the contact between the tip and the Fe center, the Shiba state vanishes and the trace

of the Andreev reflection states and the DC Josephson peak, attributed to the ballistic transport between two superconductors, start to appear (Fig.5.17(f)).

Next, we examined the behavior of the Shiba state, when approaching the ligand. Overall, the tip height is varied by 290 pm. Fig.5.18(a) shows the measured tunneling current at various tip-molecule distances *I*(z). The *I*(z) spectrum exhibits two distinct exponential increases with a slope change at $\Delta z = -120$ pm. Both of these exponential increases correspond to the tunneling regime. Contrary to the center, the tip can move almost by 100 pm more without being in point contact. Fig.5.18(b) shows five exemplary spectra recorded on the ligand of the type A molecule at five different tip heights. Additionally, all spectra recorded at various tip heights with a total variation of 290 pm is shown as a 2D color plot in Fig.5.18(c). The spectra exhibit three distinct regimes which correspond to characteristic shifts of the energy of the Shiba state.

By approaching the tip towards the ligand up to $\Delta z = -20$ pm the energy of the Shiba state increases towards the superconducting gap edge. By further decreasing the tip-molecule distance to $\Delta z = -120$ pm, the energy of the Shiba state starts to decrease towards E_F and reaches a minimum very close to the Fermi level (~ 20 μeV). At this point the asymmetry of the electron-like and hole-like components of the Shiba state is minimal. Along with the further increase of the conductance, the asymmetry of the peaks of the Shiba state reverses to favor of the electron-like part of the Shiba state (red spectrum in Fig.5.18(b)), in addition to a broadening of the Shiba resonance that shifts away from the Fermi level. We attribute this characteristic behavior of the Shiba state at the Fermi level with almost no asymmetric peaks to a quantum phase transition point. Moreover, the quantum phase transition reflects in the inversion of the asymmetry of the electron-like and hole-like components of the Shiba state. The quantum phase transition happens by changing the Shiba spin ground state. Here, the Shiba ground state is a *free spin*, which due to the influence of the tip, the ground state of the Shiba transforms to a *screened spin*. Subsequently, upon further approach to $\Delta z = -160$ pm, the energy of Shiba state moves towards the superconducting gap edge (green spectrum in Fig.5.18(a)). Finally, by decreasing the distance of the tip and the sample even further, the spectrum exhibits no clear trace of the Shiba state (black spectrum in Fig.5.18(a)). The evolution of the energy of the Shiba state at different conductances up to the vanishing of the Shiba state is represented in Fig.5.18(d). To clarify this characteristic evolution, we use the same assumptions about the symmetry and arrangement of the Fe-N atoms of the molecule as in the previous part. By approaching the tip towards the center of the molecule up to $\Delta z = -20$ pm, the pyrrole group is attracted towards the tip, resulting in a decrease of the coupling to the substrate. Considering a *free spin* ground state of the Shiba resonance, by decreasing the coupling strength to the underlying substrate, the energy of the Shiba state shifts to lower excitation energy, closer to the superconducting gap edge and reaches a maximum value at $\Delta z = -20$ pm. Interestingly, this behavior is very similar to the case of the center of the molecule (previous part) by approaching around $\Delta z = -90$ pm, which indicates reaction to the tip. Upon further approaching the tip up to $\Delta z = -120$ pm, the energy of the Shiba state is shifting towards E_{F} which corresponds to an increase of the exchange coupling strength of the magnetic impurity to the Cooper pairs of the substrate.

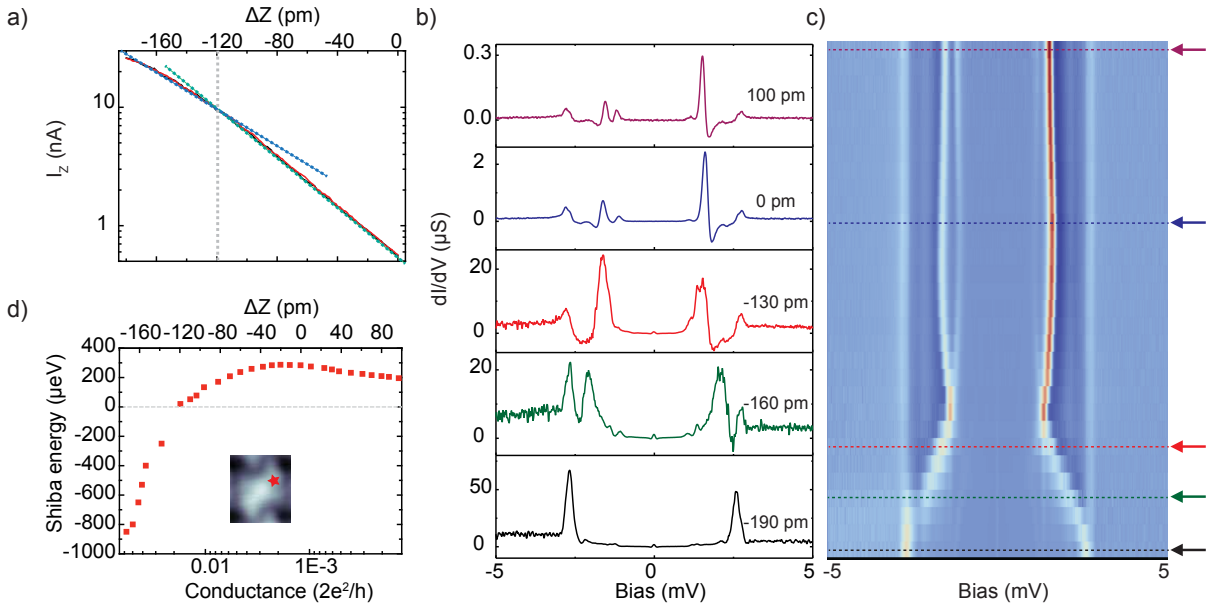

Figure 5.18: a) Tunneling current vs. relative tip approach for the ligand. The feedback opened at $I = 500$ pA and $V_{\text{bias}} = 5$ meV. b) Five dI/dV spectra acquired on the ligand of a type A molecule at different tip-molecule distances indicated by the dashed lines in (c). c) False 2D color plot of dI/dV spectra at different tip-sample distances, with decreasing tip-sample distance from top to bottom. Steps for each spectrum are 10 pm. The feedback opened at $I = 500$ pA and $V_{\text{bias}} = 5$ meV with a modulation of $V_{\text{rms}} = 50$ μeV. d) The energy of the Shiba state extracted from the spectra at different tip-sample distances. The quantum phase transition point is indicated by dashed line.

At the tip height of $\Delta z = -120$ pm the intensity of the electron-like and hole-like part of the Shiba state is almost the same which is an indication of the quantum phase transition point [16, 17]. Furthermore, by approaching the tip towards the molecule up to $\Delta z = -160$ pm the asymmetry of the Shiba peaks is reversed and, in addition, the Shiba state energy shifts towards the superconducting gap edge. Indeed, this is due to the transition to the *screened spin* ground state of the Shiba state that causes the shift of the Shiba state towards the superconducting gap edge. It is noted that the higher order Andreev reflection assisted relaxation processes can cause the inversion of the asymmetry [176]. Nevertheless, considering the energy shift of the Shiba state in addition to the faint trace of the Andreev reflection, we can exclude this relaxation effect. Upon further increase of the exchange coupling strength between the magnetic moment of the type A molecule with the underlying substrate, the Shiba state will merge to the superconducting gap edge and be seen as asymmetric BCS peaks. The faint sign of the characteristic Andreev reflections peaks and the DC Josephson peak in addition to the non-saturated conductance spectra suggest that the tip and the molecule are not yet in the contact regime (see Fig.5.18(a)).

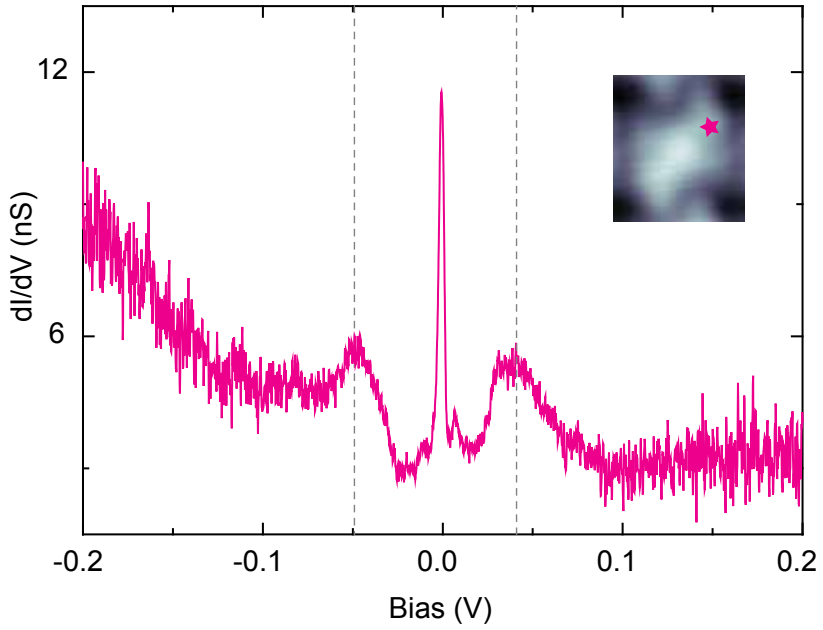

Figure 5.19: dI/dV spectrum acquired on the ligand of a type A molecule under an external magnetic field of 1.2 T shown by red star in the onset STM image. The feedback opened at $I = 800$ pA and $V_{\mathrm{bias}} = 200$ meV with a modulation of $V_{\mathrm{rms}} = 1.5$ meV.

Kondo effect on type A molecules and its relation to the Shiba states Up to now we studied the magnetic properties of type A molecules in the superconducting state. In the following we want to study the magnetic properties of the Type A molecule in the normal state. To study the magnetic properties of the Fe-TPyP molecule in the normal state, we quench the superconductivity in the sample and the tip by applying an external magnetic field up to 1.2 T. Fig.5.19 shows a spectrum taken on the ligand of a type A molecule in the normal state. We attribute the sharp peak at E_F to a Kondo resonance and the two broader resonances at ± 45 meV to the vibrational mode of the molecule which has been also detected for the type B molecules (see Sec.5.3.2). To determine the Kondo width, we fit the resonance by a Fano function (Sec.3.2.3). This yields a Kondo width of 1.1 meV (after numerical extraction of the thermal and modulation broadening). Interestingly, the Kondo width is smaller than the superconducting gap. This is an additional proof that the Shiba state is in the so-called *free spin* state. Indeed, in this case, due to the weak coupling strength of the spin to the substrate, scattering events are too weak for an efficient spin screening [177].

Considering the extracted Kondo width from the fitted spectra, an external magnetic field of $B_c \simeq 2.35$ T can split the Kondo resonance (see Sec.3.2.3). Fig.5.20 shows the spectra taken on the ligand of a type A molecule under various magnetic fields. The Kondo lineshape of spectra taken under magnetic fields

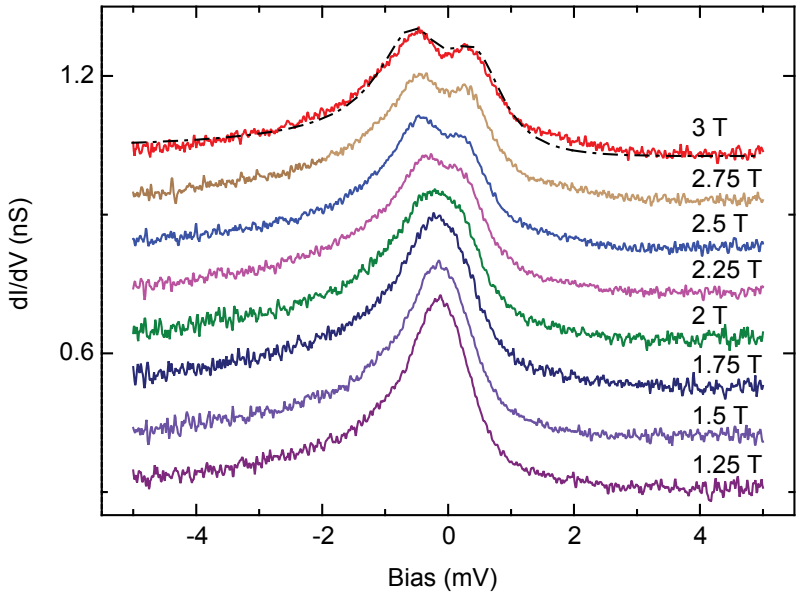

Figure 5.20: dI/dV spectra acquired on the ligand of a type A molecule under various external magnetic fields up to 3 T. The fitted spectrum at 3 T with two Fano functions shown as dashed line. The feedback opened at $I = 500$ pA and $V_{\rm bias} = 5$ meV with a modulation of $V_{\rm rms} = 30$ μeV. The spectra are offset for clarity.

up to 2 T remains unchanged. Furthermore, the spectrum taken at 2.25 T shows a small splitting of the Kondo resonance, which fits fairly well with the calculated critical field of $B_c \simeq 2.35$ T. By increasing the magnetic field to 3 T, the Zeeman energy of the splitting (see Sec.3.2.3) can be extracted from the spectrum (fitted by two Fano functions shown by dashed curves in Fig.5.20) and is around $\simeq 700$ μeV which is in agreement with the expected Zeeman splitting energy ($2g\mu_B$) [178].

We studied the variation of the Kondo width by taking spectra on different type A molecules. The variation of the Kondo width among different type A molecules is similar to our measurement uncertainty of ~ 300 μeV. Hence, we consider the Kondo width to be similar on all molecules. It has been shown that there is a direct relation between the Kondo exchange scattering strength $k_{\rm B}{\rm T_K}$ and the Shiba state energy [16, 17]. This relation can be described by [16, 70, 73, 179]:

$$a \approx \frac{\pi\Delta_0}{4k_{\rm B}{\rm T_K}} ln \frac{4k_{\rm B}{\rm T_K}}{\pi\Delta_0}, \tag{5.1}$$

where $E_{\rm Shiba} = \pm\Delta_0 \frac{1-a^2}{1+a^2}$. As we have seen in the previous part, type A molecules show one Shiba state within the gap as well as asymmetric BCS peaks that we attribute to another Shiba state very close to

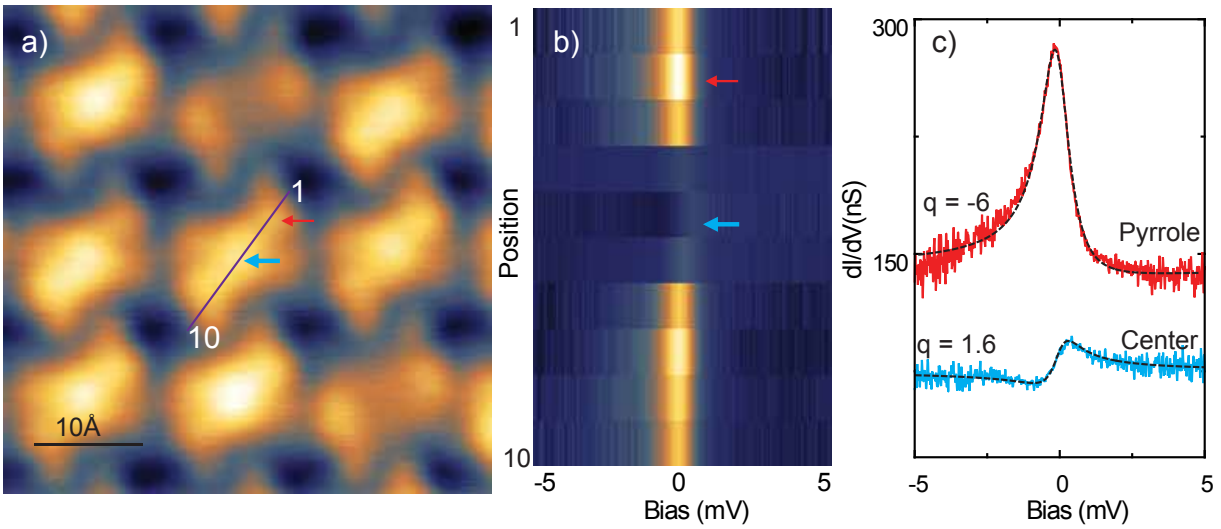

Figure 5.21: a) STM image of Fe-TPyP island. b) False color 2D plot of dI/dV spectra along a type A molecule as indicated by the line in (a)(B=1.2 T). c) dI/dV spectra acquired on top of the ligand and the center of a type A molecule by arrows in (a,b). The fitted spectra with Fano function shown as dashed lines. The feedback opened at $I = 500$ pA and $V_{\mathrm{bias}} = 5$ meV with a modulation of $V_{\mathrm{rms}} = 50$ μeV. The spectra in (c) are offset for clarity.

the gap edge. In the following, we address the possible correlation between the observed Kondo resonance in the normal state and these two Shiba states seen in the superconducting state.

A Shiba state with its energy close to the gap edge can be obtained in two distinct cases: (1) The magnetic exchange strength is so weak that the energy of the Shiba state is very close to the gap energy. In this case, the spin of the impurity is a *free spin* and the corresponding Kondo temperature will be very small [13, 71, 175], *i.e.* it will lie below our measurement temperature. This is contrary to our finding. (2) The magnetic exchange strength is much stronger than the pairing energy. In this case, the spin of the impurity is *screened* and the corresponding Kondo width is higher than the gap energy. In this case, we should observe a Kondo resonance in the superconducting state as well [177]. Therefore, the Kondo resonance observed in the normal state does not correspond to the Shiba state localized at the gap energy.

The Kondo resonance can however be related to the Shiba state inside the superconducting gap. Indeed, the energy of the Shiba state among different type A molecules ranges from 375 μeV to 900 μeV. In the case of an impurity with a *free spin*, the corresponding Kondo width $k_{\mathrm{B}}\mathrm{T}_{\mathrm{K}}$ calculated with Eq.5.1 will vary from 470 μeV to 575 μeV and their energy difference will be in the range of our energy resolution. Hereby, we conclude that the Kondo resonance corresponds to the Shiba state deep inside the superconducting gap.

To reveal the lateral extension of the Kondo resonance over the molecule, we performed the spectroscopy along the main axis of a type A molecule (see line in Fig.5.21(a)). Fig.5.21(b) presents the set of spectra as

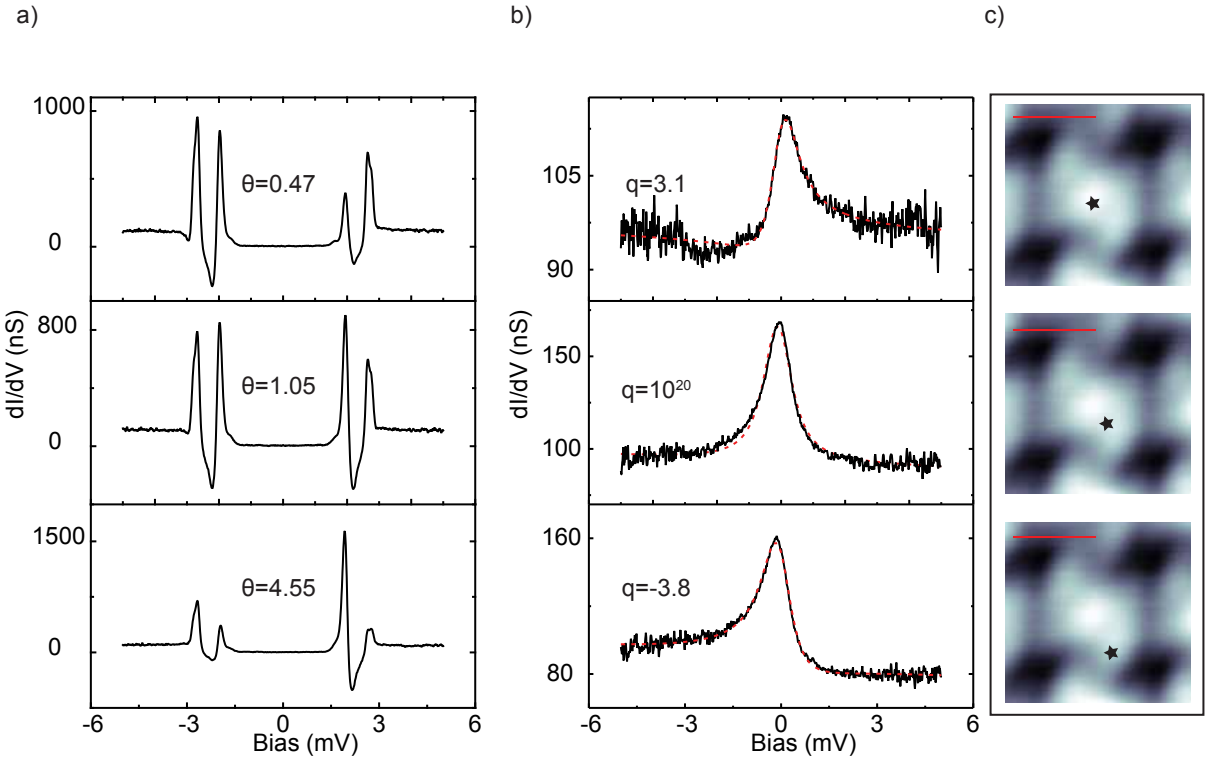

Figure 5.22: dI/dV spectra acquired on top of different parts of a type A molecule indicated by black stars in (c). a) In the superconducting state: the corresponding asymmetry factor of the intensity of the Shiba peaks θ is given for each spectrum. b) In the normal state (B=0.6 T): red dashed lines show the fits with a Fano function. The corresponding q factors of each spectrum are shown. The feedback opened at $I = 500$ pA and $V_{\mathrm{bias}} = 5$ meV with a modulation of $V_{rms} = 15$ μeV for (a) and $V_{\mathrm{rms}} = 50$ μeV for (b). c) STM images of a type A molecule. The red bar is 10Å long.

a 2D color plot. Fig.5.21(c) shows two spectra taken on the center and on the ligand of a type A molecule as indicated by two arrows in Fig.5.21(a,b). The fits of the spectra with a Fano function are represented with dashed lines. We see an extension of the Kondo resonance over the molecule. Moreover, the q factor of the fitted Fano line shape changes over the molecule. Interestingly, the sign of the q factor is negative for the Kondo resonance on the ligand and positive on the center.

To investigate the analogy between the Shiba state and its corresponding Kondo peak, we compare the spectra taken on the center (upper panel in Fig.5.22(a,b)), on the ligand (lower panel in Fig.5.22(a,b)) and on the bridge carbon atom (middle panel in Fig.5.22(a,b)) of a type A molecule in the superconducting and normal state. On the center of the molecule, the spectrum shows a Shiba state with higher intensity of the electron-like peak (upper panel in Fig.5.22(a)). In the normal state, this corresponds to a Kondo

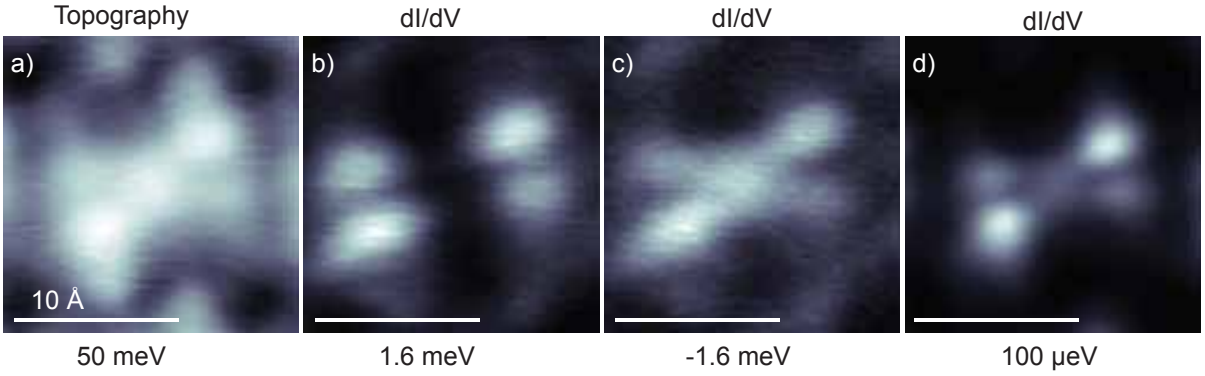

Figure 5.23: a) STM image of a Fe-TPyP type A molecule. b,c) Corresponding multi pass dI/dV maps of a Fe-TPyP molecule at the Shiba energy indicated under the maps. First the image scanned at $I = 500$ pA and $V_{\mathrm{bias}} = 5$ meV for the feedback reference then the map recorded at the corresponding energies at these height with a modulation of $V_{\mathrm{rms}} = 15$ μeV. For d) Constant height dI/dV map at $V_{\mathrm{bias}} = 50$ μeV and $I = 500$ pA with a modulation of $V_{\mathrm{rms}} = 15$ μeV.

resonance with a positive q factor (upper panel in Fig.5.22(b)). On the contrary, the Shiba state above the ligand of the molecule exhibits higher intensity of the hole-like peak, corresponding to a Kondo resonance with a negative q factor (lower panel in Fig.5.22(a,b)). Furthermore, the spectra taken on the bridge carbon atom shows a Shiba state with the same intensity of the electron-like and hole-like peaks (middle panel in Fig.5.22(a)). The corresponding Kondo exhibits an almost perfect Lorentzian peak with a q factor close to infinity (middle panel in Fig.5.22(b)).

The q factor usually quantifies the quantum interference between two tunneling channels: directly from tip to the substrate and from tip through the Kondo state [64, 180, 181]. Furthermore, the asymmetry of the intensity of the peaks of the Shiba state is associated with the tunneling to the occupied and unoccupied parts of the Shiba state. It seems that there is a clear correlation between these two parameters. To some extent this could be understood in both cases of the excitation spectrum of a many-body state that has correlated electron and hole components.

To see the precise evolution of the magnetic fingerprint we probe its lateral extension along a molecule. To do so, we map in Fig.5.23 the dI/dV signal at the energies corresponding to the Kondo state (d), the electron-like peak of Shiba state (c) and the hole-like peak of Shiba state (b) of a Fe-TPyP type A molecule. The resemblance of these states are two-fold: (1) The hole-like part of the Shiba state (Fig.5.23(b)) is mainly localized on the ligand and shows no signal above the center of the molecule. As for the electron-like part of the Shiba state (Fig.5.23(c)), it is delocalized over the ligand as well as the center of the molecule. Considering this localization, we can attribute the evolution of the asymmetry of the peaks of the Shiba state over a molecule to the variation of the localization of the hole-like part of the Shiba state. This variation has

been observed in case of single magnetic atoms on the superconductor substrate and assigned to the effect of different orbital assisted phase shifts of the electron and hole components of the Shiba state [39, 171]. (2) The Kondo state (Fig.5.23(d)) retains the same symmetry as the electron-like and hole-like components of the Shiba state that are mainly localized over the ligand of the molecule as well as the Fe center. This similarity indeed comes from the fact that these states represent the scattering of quasiparticles on the molecule.

As it has been discussed in Sec.3.2.3, the q factor of the Fano line-shape are determined by the interference between the tunneling paths to the Kondo state and to the sample continuum. However, in this general picture, the probability of tunneling with electrons or holes are considered to be the same. This means that, there is no difference between the interference obtained by probing the system with electrons or holes [64]. Some attempts have been done to investigate the effect of different carriers (electrons or holes) [57, 182–184]. Additionally, the effect of tunneling through different d-orbitals that are involved in the Kondo effect has been investigated. In this case, the interference factor (q factor) arises from tunneling into different d-orbitals that give rise to different q factor values with even different sign (negative in case of d_{xz} and d_{yz})[185, 186]. Experimentally, also some molecules have shown the position-dependence variation of the q factor with sign changes [146, 187–189]. Under the assumptions of different tunneling probability for electrons and holes due to different orbitals that are involved in Kondo effect, the correlation between the Shiba state asymmetry and the q factor of the Kondo state might be understood in a picture of the orbital-assisted tunneling. Similar to the case of type B molecules, tunneling to the hybridized orbitals of the Fe and the organic ligand results in observing the magnetic fingerprint across the whole molecule. On the center of the molecule, the tunneling occurs mainly via the Fe orbitals, particularly the d_{z^2} orbital. Hence, the character of the Shiba state and the Kondo resonance will be dominated by the Fe orbitals. In this case, the Shiba asymmetry and the q factor of the Fano line-shape are determined by the probability of the electron and hole tunneling through the Fe orbitals. However, on the ligand, the tunneling occurs through the hybrid orbital(s) which have character of the Fe orbitals as well as of the π system. These complexities can posses preference in the tunneling with electrons or holes depending on their wave functions, their occupations and energy with respect to the Fermi level. In a simple picture, the tunneling probability to excite the Shiba state with a hole is much higher than the one with an electron due to the tunneling via an unoccupied state that enhances the tunneling probability of holes. Therefore, this yields an increase of the hole-like intensity of the Shiba state. Correspondingly, in the Kondo resonance, this will change the interference by involving more hole carriers. Indeed, the localization and the symmetry of the hole-like part of the Shiba state 5.23(c,d) are similar to the LUMO (compare to Fig.5.4(d), Sec.5.3.2).

5.3.4 Bistable molecules: a molecule with both magnetic fingerprints

In the previous section we have investigated the magnetic properties of both types of molecules. Type A molecules exhibit two Shiba states, one that lies very close to the superconducting gap edge that gives

rise to the asymmetry in the intensity of the BCS peaks. Additionally, another Shiba state is well inside the superconducting gap and delocalized over the whole molecule. Type B molecules exhibit two spin excitations that are extended over the molecule. These spin excitations originate from transitions between the anisotropy-split spin state of the Fe center. It is known that, to be able to excite the spin states of an impurity on a substrate, the direct overlap between the orbitals of the impurity with the underlying substrate has to be minor. On the contrary, for having many-body states at the impurity such as the Kondo effect or/and Shiba states, the overlap between the orbitals of the magnetic impurity and the substrate has to be such that the electrons of the substrate are able to scatter with the impurity efficiently. Therefore, the hybridization between the Fe center of type B molecules has to be much less than the one in the case of type A molecules. This can be achieved by adapting slightly different saddle shapes from less buckling for type B to higher buckling for type A molecules [139, 190]. The variation of the saddle configurations can be understood by considering the effect of different adsorption sites. This means that for instance, top adsorption sites increase the hybridization of the Fe center with the underlying substrate due to the smaller Fe-substrate distance, while hollow adsorption sites maximize the Fe-sample distance and result in lowering the overlap between their orbitals.

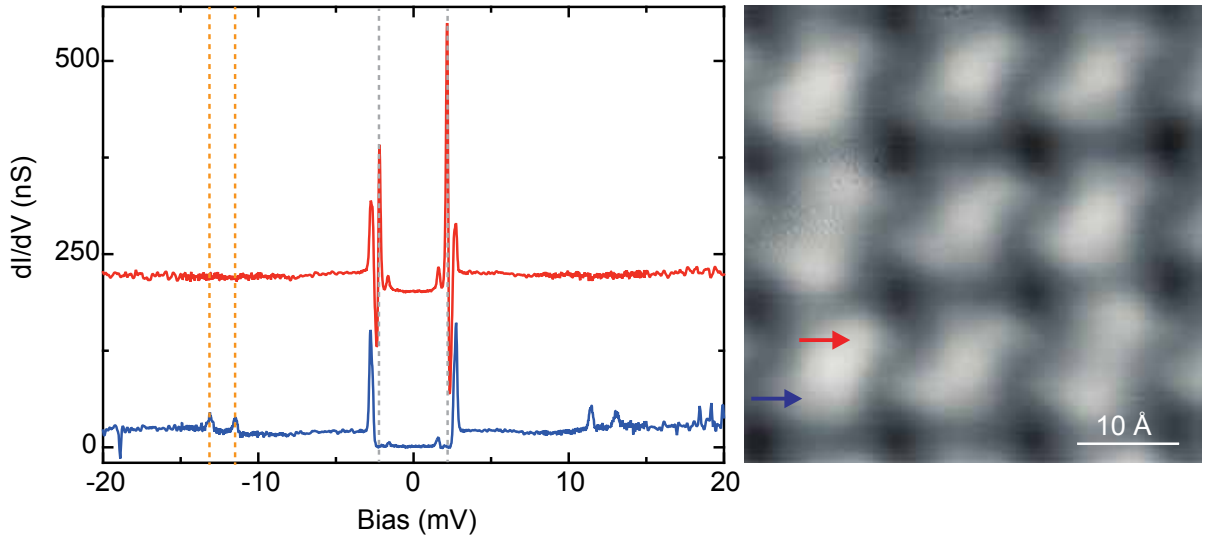

Figure 5.24: dI/dV spectra on two parts of a bistable molecule. Some parts of the molecule exhibit two spin excitations (blue) while the other half shows the Shiba state (red). STM image of a Fe-TPyP island. The corresponding point of taken spectra are indicated by the arrows. The feedback opened at $V_{\mathrm{bias}} = 20$ meV and $I = 500$ pA with a modulation of $V_{\mathrm{rms}} = 15$ μeV.

One strong indication for the influence of the adsorption site on different types of molecule mentioned above comes from observing molecules that shows the magnetic fingerprint of type A molecules on half of

the time, while the other half exhibits the magnetic fingerprint of type B molecules. Fig.5.24 shows two exemplary spectra recorded on different parts of such a molecule. The spectrum recorded on the upper pyrrole (red) shows the Shiba state, although the spectrum taken on the lower pyrrole exhibits two spin excitations. This can be explained by assuming a bistable conformation that the molecules can switch between them by the influence of the tip. In a simple picture this can be visualized as the molecule moves slightly and changes the hybridization between the Fe orbitals and substrate.

5.3.5 Summary

Self-assembled islands of Fe-TPyP on Pb(111) consist of two types of molecules (type B and A). Type B molecules exhibit a superstructure with a clear registry with the underlying substrate. On the contrary, type A molecules are randomly distributed without any obvious registry pattern with the underlying substrate.

Electronic properties of both types of molecules involve (frontier) molecular orbitals originating from the organic ligands, d-orbitals of Fe and hybridized states between the d-orbitals of the Fe atom and π orbitals of the organic macrocycle. In addition to these electronic states, both types of Fe-TPyP molecules exhibit some vibrational signatures. Tunneling to the molecular electronic states, make the vibrational modes more efficient. However, for type A molecules only one vibrational mode is detected. This might be due to different hybridization between the molecule and the underlying substrate that changes the efficiency of the excitation of the vibrational modes.

Both types of the Fe-TPyP molecules additionally show magnetic fingerprints. Type A molecules exhibit two Shiba states, one that lies very close to the superconducting gap edge and gives rise to the asymmetry in the intensity of the BCS peaks. Additionally, another Shiba state is well inside the superconducting gap and localized over the whole molecule. Interestingly, the ratio between the intensities of the electron-like and hole-like quasiparticle of the Shiba state changes over the molecule such that this ratio is smaller than the one for the center and increases by almost a factor 5 for the ligand. In the normal state, type A molecules exhibit a Kondo resonance that is extended over the whole molecule. The Kondo resonance arises from the same exchange scattering potential that also leads to the Shiba state well inside the superconducting gap. Interestingly, the asymmetry factor of the Fano line-shape of the Kondo resonance changes over the molecule including a sign change. The asymmetry of the Shiba state and the Kondo resonance appears correlated to each other.

Type B molecules exhibit two spin excitations that are extended over the ligand of the molecule. These spin excitations originate from transitions between the anisotropy split spin levels of the Fe center. Considering the S=1 system of the Fe center, two spin excitations can be obtained. Due to the presence of the ligand field, the Fe center has axial and transverse magnetic anisotropies. Via tunneling through the hybridized state, the spin of the central Fe can be excited on the ligand of type B molecules. Upon approaching the tip towards the molecule, the d-orbitals of the Fe center can be rearranged resulting in a variation of the D and E anisotropies.

All in all, by comparing the electronic and magnetic fingerprints of both types of the molecules, we can conclude that the Fe center of type A molecules hybridizes more strongly with the underlying substrate. This can be obtained by a more pronounced saddle configuration of the molecule, which is a result of the adsorption site that maximizes the overlap between the Fe center of the molecule and the underlying substrate. For type B molecules this hybridization is reduced. This indicates that type B molecules have slightly less saddle shape probably due to adsorption on a hollow site. As a result of the reduced hybridization, we do not find any Shiba states inside the superconducting energy gap. In contrast, the magnetic state of the molecule is reflected by inelastic spin excitations.

5.4 Manganese-porphyrin on Pb(111): importance of the central metal

In this part, we study the influence of the central atom by substituting the Fe atom with a Mn one. Indeed, different transition metals have different magnetic moments depending on their number of electrons in the d-orbitals. Additionally, the strength of spin-orbit coupling can change, leading to different magnetic anisotropy energies. In manganese atoms embedded in porphyrin molecules, the Mn atoms are in the +2 oxidation state and they have five electrons in their d-orbitals. Depending on the ligand field, they can have a low spin state $S = 1/2$ [191], an intermediate spin state $S = 3/2$ [17, 192, 193] or a high spin state $S = 5/2$ [194, 195]. It has been shown that manganese phthalocyanine (Mn-Pc) molecules on Pb(111) show multiple Shiba states and a Kondo resonance [17]. Moreover, depending on the adsorption site of Mn-Pc molecules, the exchange coupling strength of the Shiba states changes, such that the Shiba ground state undergoes a quantum phase transition [16, 17].

In this part of this chapter we focus on studying the interaction between manganese-5,10,15,20-Tetra(4-pyridyl)porphyrin (Mn-TPyP) molecules on the superconducting substrate Pb(111).

5.4.1 STM investigation of Mn-TPyP on Pb(111)

Deposition of a submonolayer of Mn-TPyP molecule onto Pb(111) at room temperature leads to the formation of long-range ordered molecular islands as shown in Fig 5.25(a). The molecules form structures with two distinct arrangements labeled as arrangement A and B. Fig 5.25(b) shows a close-up view of the molecular arrangement A, that consists of two different rows of molecules with different azimuthal orientations that are rotated by $\sim 30^\circ$ with respect to each other, which is indicated by I and II. The molecular arrangement A can be characterized by a nearly rectangular structure with lattice parameters of $a_1 = (13 \pm 0.2)$ Å, and $a_2 = (27 \pm 0.2)$ Å (green and blue lines). This arrangement is similar to the one of the free based molecules (H_2-TPyP) on Ag(111) [136]. The second molecular arrangement B, consists

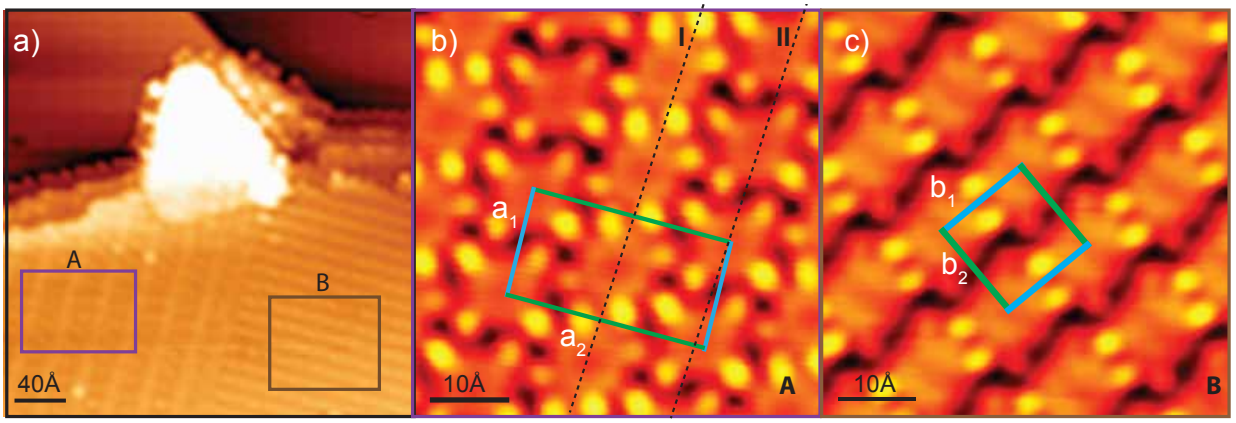

Figure 5.25: STM topographic images of a) self-assembled Mn-TPyP molecules. The molecular islands have two distinct arrangements indicated with A and B. b,c) Zoom into the Mn-TPyP structure. The A arrangement consists of two alternating molecular rows (I,II) and has a nearly rectangular unit cell indicated by a_1 and a_2 (blue and green lines in (b)). The B arrangement has a rectangular unit cell indicated by b_1 and b_2 (blue and green lines in (c)).

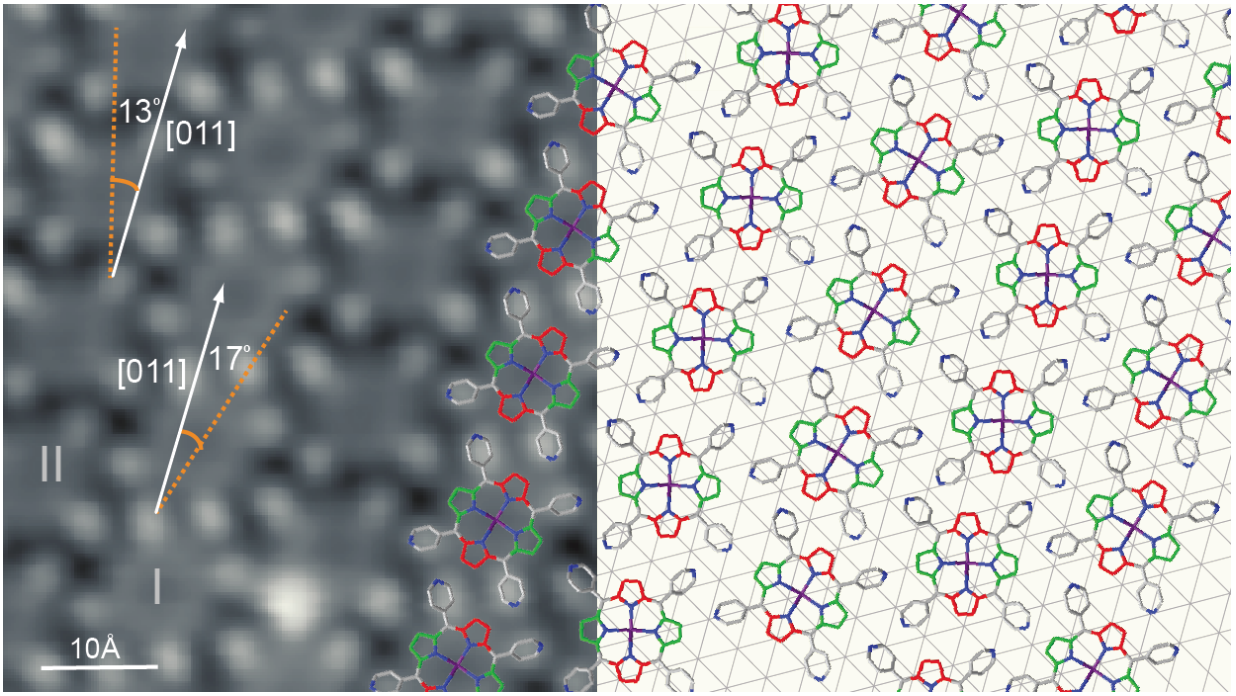

Figure 5.26: STM topographic images of self-assembled Mn-TPyP molecules. The main axis of Mn-TPyP molecules in rows I and II are rotated with respect to the [011] high symmetry direction of Pb(111) by 17° and $-13°$, respectively. The molecular models are overlaid on the STM image as well as the underlying substrate Pb(111). Mn-TPyP molecules adsorb randomly on Pb(111) with no preferred adsorption sites.

of molecular rows that are aligned with each other (Fig 5.25(c)). This structure has nearly square unit cell with lattice constants of $b_1 = b_2 = (13 \pm 0.2)$ Å (green and blue).

In both molecular arrangements, molecules show a rectangular shape with four bright protrusions and a depression at the center. The bright protrusions are attributed to the pyridine end groups that are rotated with respect to the substrate. In the case of the H_2-TPyP, it has been shown that the molecule exhibits a saddle shape such that the pyridine groups are rotated by $60°$ [136]. This leads to a relatively weak deformation of the macrocycle [127, 135, 139]. Hence, Mn-TPyP molecules similar to the Fe-TPyP molecules adapt the saddle configuration.

By overlaying the symmetry of the substrate to the molecular island, we can investigate the registry of the absorption behavior of the molecules with the underlying Pb(111) substrate. For the molecular arrangement A, as one can see in Fig.5.26, the main axes of the molecules are rotated by $17°$ and $-13°$ with respect to the high symmetry direction [011] of the substrate. Moreover, each of the molecular rows is following the high symmetry directions of Pb(111). The molecular unit cell is not commensurate with the substrate lattice and hence the molecules adapt all different adsorption sites, which is similar to the case of H_2-TPyP molecules on Ag(111). The same holds for arrangement B, where the molecules are also not commensurate with the underlying substrate.

Regarding different adsorption sites of the Mn-TPyP molecules, we want to investigate the impact of these different adsorption sites on their electronic and magnetic properties.

5.4.2 Electronic and magnetic properties of Mn-TPyP molecules

To investigate the electronic and magnetic properties of the Mn-TPyP molecules, we perform STS on different parts of the Mn-TPyP molecules (Fig.5.27). It is worth to mention that all of the Mn-TPyP in different molecular arrangements (A,B) show the same spectroscopic features. Fig.5.27(a) shows a typical set of constant height spectra taken on the pyridine end group (blue) and pyrrole ligand (green) of a Mn-TPyP molecule. The spectra exhibit a double resonance at 780 meV and 980 meV for both parts of the molecule, which are attributed to the LUMO where its degeneracy has been lifted [136]. Additionally, both spectra show a resonance at 2.05 eV that is attributed to the next higher unoccupied level LUMO+1. The energy position of the double peaks of the LUMO as well as their energy splitting is comparable with the case of Fe-TPyP (see Sec.5.3.2) with a slightly smaller energy difference in the case of Mn-TPyP. This is an indication of a smaller deformation of the macrocycle that gives rise to less splitting of the LUMO. Interestingly, none of the vibrational modes seen in the case of Fe-TPyP on Pb(111) (see Sec.5.3.2) are resolved above Mn-TPyP molecules.

To study the possible magnetic interaction of the Mn center with the underlying substrate, we recorded spectra on the Mn center (red) as well as the Pb(111) substrate with a superconducting tip (Fig.5.27(b)). Under such circumstances, the superconducting gap at 4.5 K is reduced to $\Delta = 1.1$ meV and subsequently the spectrum on Pb shows broader BCS peaks at smaller energy with respect to the one recorded at 1.1 K.

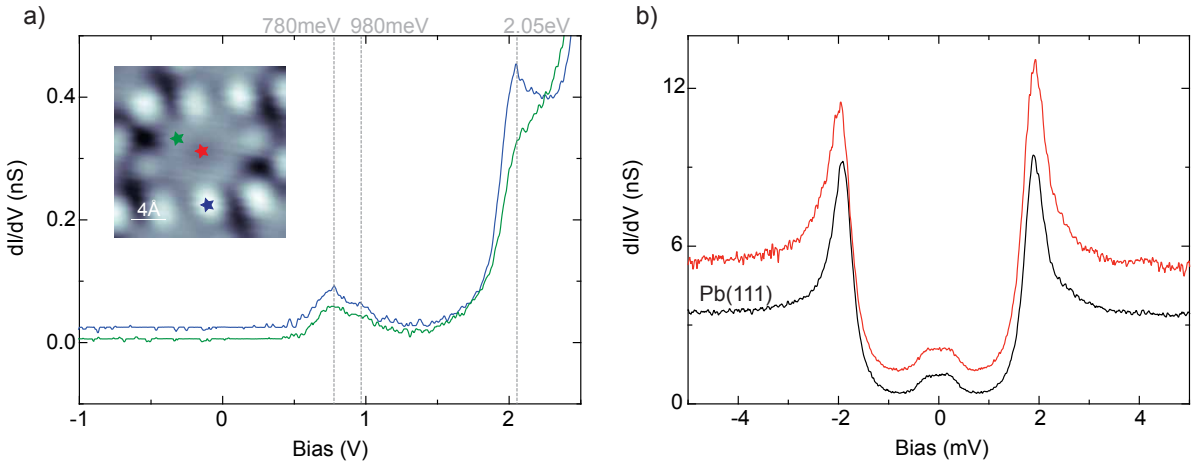

Figure 5.27: a,b) Constant height dI/dV spectra acquired on top of the Mn center (red), on top of the pyridine end group (blue) and on top of the pyrrole ligand (green) of a Mn-TPTBP molecule indicated by stars in the inset STM image. In (a) the feedback opened at $I = 300$ pA and $V_{\text{bias}} = 2.5$ eV with a modulation of $V_{\text{rms}} = 5$ meV. In (b) the feedback opened at $V_{\text{bias}} = 10$ meV and $I = 300$ pA with a modulation of $V_{\text{rms}} = 100$ μeV. All spectra are recorded at 4.5 K.

Additionally, the spectrum exhibits a small peak at the Fermi level, which originates from tunneling of the thermally populated unoccupied quasiparticle states of the tip to the thermally depleted occupied states of the sample and vice-versa. The spectrum taken on the Mn center shows the BCS peaks but with different intensity in addition to the thermal peak at the Fermi level. As we have discussed in the case of Fe-TPyP (Sec.5.3.3), the asymmetry in the BCS peak is caused by a Shiba state very close to the gap edge. Additionally, we did not detect any sign of a Kondo resonance at $\mathrm{E_F}$, we can therefore conclude (see Sec.5.3.3) that the impurity has a *free spin* ground state. The weak spin exchange scattering strength of this Shiba state might be due to a small hybridization of the Mn center with the underlying substrate. This small overlap would be a consequence of the deformation of the molecule, which is due to the rotation of pyridine end groups to minimize the steric forces. This might be also the origin of different energies splitting of LUMO as well as the absence of the vibrational modes in comparison with Fe-TPyP molecules on Pb(111). In order to modify the hybridization between the Mn center and the underlying substrate, one way is to exchange the end groups. Hence, we changed the pyridine end groups to the flexible tert-butyl end groups.

5.4.3 Summary

To manipulate the spin state and consequently the magnetic interaction between the metal-organic complexes and the Pb(111) superconducting substrate, we have substituted the central Fe atom with Mn. Deposition of the Mn-TPyP molecules yields self-assembled long ranged ordered molecular islands. The molecular

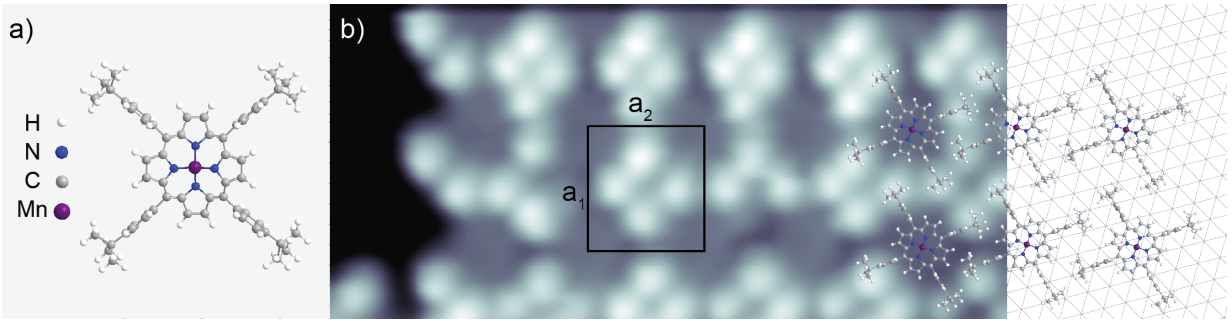

Figure 5.28: a) Molecular model of Mn-TPTBP. b) STM topographic image of self-assembled Mn-TPTBP molecules with a rectangular unit cell indicated by a_1 and a_2. Mn-TPTBP molecules are overlaid on the STM image as well as on the underlying substrate.

islands can be formed in two distinct arrangements: (1) two alternating rows of molecules with different azimuthal orientations, very similar to the case of free based H_2-TPyP molecules on Ag(111). (2) A square-like arrangement of the Mn-TPyP molecular rows. Acquired spectra on the molecule show the signal of the doubly degenerated LUMO orbital. Its splitting upon adsorption is slightly lower than in the case of Fe-TPyP on Pb(111). This can be explained by a lower deformation of the macrocycle. Additionally, we observed an asymmetry in the BCS peaks, which is due to a Shiba state at the energy close to the gap edge with the *free spin* ground state. The impact of substituting the central metal from Fe to Mn is not only on the magnetic properties but surprisingly on the molecular arrangement. Thus, to further manipulate the magnetic interaction between the Mn center with the underlying substrate, we embedded the Mn atom into another organic ligand. To do so, we have substituted the pyridine end groups with tert-butyl groups.

5.5 Mn-TPTBP molecules on Pb(111): exchanging the end groups

In this part, to manipulate the deformation of porphyrin macrocycle, we changed the pyridine end groups to phenyl-tert-butyl end groups. The manganese tetra-phenyl-tert-butyl-porphyrin (Mn-TPTBP) molecule consists of a Mn atom embedded inside the porphyrin macrocycle with four phenyl-tert-butyl end groups attached to it (Fig.5.28(a)). It has been shown that the manganese center retains the S=5/2 spin state in the case of Mn-TPTBP on the Au(111) substrate where the interaction with the substrate results in a many body Kondo state [196]. Evaporation of a submonolayer of Mn-TPTBP molecules onto Pb(111) at room temperature leads to the formation of ordered molecular islands as shown in Fig 5.28(b). The molecules arrange in a rectangular structure with lattice vectors of $a_1 = (17.5 \pm 0.5)$ Å and $a_2 = (15.5 \pm 0.5)$ Å. Each molecule appears as four bright protrusions, which are attributed to the bulky tert-butyl groups with a depression at the center. By overlaying the Pb(111) substrate to the molecular island, we investigate the adsorption sites of the molecule on the substrate. Each of the main axes of the porphyrin macrocycle

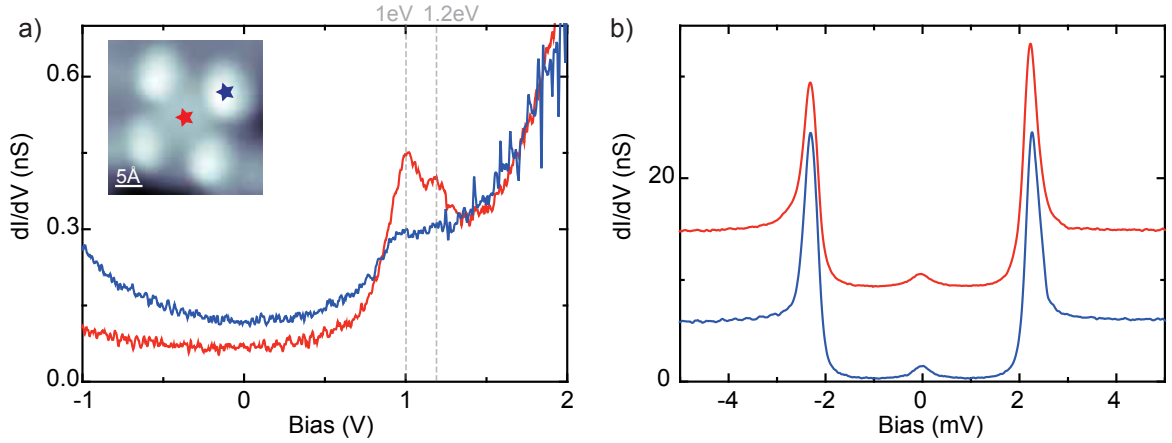

Figure 5.29: a,b) Constant height dI/dV spectra acquired on top of the Mn center(red) and on tert-butyl end group (blue) of a Mn-TPTBP molecule indicated by stars on the inset STM image. In (a) the feedback opened at $I = 500$ pA and $V_{bias} = 2$ eV with a modulation of $V_{rms} = 5$ meV. In (b) the set point is $V_{bias} = 10$ meV and $I = 500$ pA with a modulation of $V_{rms} = 50$ μeV. All spectra are recorded at 4.5 K.

follows the high-symmetry directions of the substrate. However, molecules adapt no preferred adsorption sites, hence, they are randomly distributed on the Pb(111) surface (Fig 5.28(b)). It is worth to mention that the molecule can be dragged out of the molecular island and be isolated from the other molecules by the help of the STM tip.

Fig.5.29(a) shows dI/dV spectra recorded on the ligand and on the center of the Mn-TPTBP molecules. The spectra exhibit two peaks at 1.1 eV and 1.2 eV that are attributed to the LUMO. This is very similar to the case of the same molecule on Au(111) [196].

To reveal the magnetic interaction between the Mn and the underlying superconducting substrate, dI/dV spectra are recorded in the Mn center (red) and on the butyl end group (blue). Similarly to the case of Mn-TPyP molecules on Pb(111), the spectrum in the Mn center exhibits an asymmetry of the BCS peaks that corresponds to a Shiba state at the gap edge and no Kondo resonance in the normal state. The Shiba state therefore has a *free spin* ground state, which indicates a weak hybridization of the Mn center with the superconducting substrate Pb(111). This might be due to the fact that the relatively large butyl end groups lift the macrocycle away from the substrate and, thus, reduce the hybridization between the Mn atom and the underlying substrate.

5.5.1 Summary

Deposition of the Mn-TPTBP molecules onto Pb(111) at room temperature gives rise to the formation of ordered molecular islands. The molecules adapt a rectangular arrangement with no commensuration

with the substrate. The signal of unoccupied molecular orbitals has been reordered, showing a very similar energy for the LUMO as in the case of Mn-TPTBP on Au(111). The magnetic fingerprint of the molecules resolved an asymmetry in the BCS peaks. Similar to the case of Mn-TPyP, due to the weak exchange interaction of the Mn center with the Pb substrate, a Shiba state at the gap edge with a *free spin* ground state is responsible for the asymmetry.

5.6 Conclusions

In this chapter, we have shown the importance of the metal-atom to the surface distances to determine different magnetic properties in the metal-organic complexes. In the first part, the evaporation of Fe-TPyP molecules provided the big variation of the Fe-Pb(111) distances, resulting in different magnetic fingerprints. Type A molecules exhibit Shiba states that have different energies among different molecules. This variation of the Shiba states energies was a consequence of the different spin exchange coupling strengths of Fe centers due to different hybridization between the Fe center and the underlying substrate. Although, the Shiba state energy was varied among different molecules but did not undergo any quantum phase transition in contrast to the Mn-Pc on Pb(111). This can be understood as a result of more decoupled Fe-TPyP molecules compared to Mn-Pc molecules. Interestingly, the quantum phase transition could have been induced to the type A molecules by means of the tip. The forces of the tip for different tip-molecules distances have changed the distance of Fe center to the substrate such that the Shiba ground state has been changed from *free spin* to *screened spin*. On the contrary, type B molecules adapt the hollow adsorption site, resulting in well decoupled Fe centers from the substrate. The fingerprint of such small overlap between the Fe center and the underlying substrate was detected as spin excitations of Fe center.

In the next part, the Fe center has been substituted with the Mn to manipulate the magnetic properties of the molecules. Surprisingly, this change not only modified the magnetic fingerprint of the Mn-TPyP molecule but also the molecular arrangement. The signal of weak exchange scattering strength of Mn center has been detected as a Shiba state at the energy very close to the gap edge.

In the last part, by exchanging the pyridine end groups of the Mn-TPyP molecules complex to the more bulky phenyl-tert-butyl, we attempted to alter the distance of Mn center to the underlying substrate. This modification, although results in a very similar magnetic fingerprint to the Mn-TPyP molecules.

This findings provide a general prospective of how to manipulate the magnetic properties of metal-organic nanostructures. The crucial impact of the hybridization of metal-atoms with the underlying substrate has been investigated. This can provide intelligent ways to manipulate the magnetic properties of metal-organic nanostructures for instance by dosing small organic molecules, *e.g.*,CO, H_2, N_2 as axial ligands.

Chapter 6

Summary and conclusion

In this thesis, we investigated the magnetic properties of different metal organic nanostructures on the superconducting Pb(111) substrate. The main aim was to produce a metal organic assembly, where the metal atoms have all different magnetic interaction strengths. To obtain such nanostructures, two main approaches have been followed: (1) *In-situ* linking of atoms with an organic acceptor molecule into a metal-organic network. (2) Deposition of already metallated porphyrin molecules. The variety of the metal atoms and organic ligands can provide a playground to manipulate the magnetic interaction of such metal organic nanostructures in a controlled way. Scanning tunneling microscopy (STM) has been used as a main experimental tool to study the structure and assembly of the metal-organic nanostructures with atomic precision. Moreover, to investigate their electronic and magnetic properties, scanning tunneling spectroscopy (STS) was utilized.

As a first attempt, we have used the organic electron acceptor tetracyanonaphtho-quinodimethane (TNAP) to link with different metals for producing metal organic networks. Due to the high mobility of Pb adatoms, coordination bonds are formed between them and cyano-based organic linker molecules. The incorporation of Pb is, however, not a desired structure, since Pb atoms are non-magnetic and their ionization potential is not sufficiently low for donating charge to the acceptor molecule. In an attempt to avoid coordination with Pb, we co-deposited NaCl, which provided Na as a donor atom.

Despite the charge transfer, these structures did not exhibit fingerprints of a magnetic interaction with the superconducting substrate. By exchanging the Na atoms with Fe, a Shiba state in the superconducting gap revealed the desired magnetic interaction with the superconducting substrate, although the effect of the direct environment of the Fe atoms on this Shiba state was not clear due to the high irregularity of the network. Nonetheless, we expect that a careful design of the molecular linkers will allow for the creation of magnetic metal-organic networks with long-range order.

The second strategy was to produce metal-organic nanostructures from already metallated molecules. Different metals and organic ligands have been used to manipulate the magnetic interaction of the nano struc-

tures with the underlying substrate.

In the first part, the evaporation of iron-tetrapyridineporphyrin (Fe-TPyP) on Pb(111) resulted in long-range ordered molecular islands that include in two types of molecules (type A and B) that both exhibit a saddle conformation. The Fe-TPyP molecule exhibits a doubly degenerate LUMO that upon adsorption on the surface splits by ~ 200 meV for both types of the molecule. Additionally, both types of molecules show some vibrational signal.

Furthermore, we have investigated the magnetic properties of each type of molecule. The magnetic fingerprint of type A molecules is detected as a two Shiba states, one at the energy of the gap edge and the other one inside the superconducting gap. The energy of the Shiba state inside the superconducting gap varies among different molecules. This variation is a sign of a different spin exchange scattering strength of the Fe center with the Cooper pairs. The origin of this change is the different hybridization between the Fe center and the underlying substrate that might come from different adsorption sites. Interestingly, contrary to the case of manganese-phthalocyanine (Mn-Pc) molecules on Pb(111), the interaction does not undergo a quantum phase transition. This might be due to the enhanced decoupling of the Fe center from the surface. However, the quantum phase transition can be obtained by the help of the tip. Depending on the tip-sample distances, different forces act on the Fe center, resulting in a decrease of the Fe-surface distance. At a certain coupling strength, the Fe undergoes a quantum phase transition. This manipulation of the magnetic fingerprint can be successfully reversed by retracting the tip from the Fe center. Additionally, by investigating the behavior of the Shiba state at different conductances, we could determine the Shiba ground state to be in the *free spin* ground state. This finding has been supported by measuring the corresponding Kondo resonance in the normal state. Moreover, the intensity ratio of the electron-like and hole-like quasiparticle components of a Shiba state inside the superconducting gap varies over the molecule. Interestingly, the q factor of the Fano line-shape of the Kondo resonance also changes over the molecule. It correlates with the intensity changes of the Shiba peaks. Therefore, this finding adds another factor to this universal correlation, which is determined by the tunneling process.

Type B molecules posses a very different magnetic fingerprint. We observed two spin excitations that originate from the Fe center. Interestingly, these spin excitations are extended over the whole molecule. To observe the spin excitations, the Fe center has to be decoupled such that no Cooper pairs are scattered at the Fe center. This situation can be obtained by maximizing the Fe-surface distance. Indeed, by adapting the hollow adsorption site, the hybridization of the Fe center with the underlying substrate is minimized.

In the next part, we exchanged the Fe center with Mn atoms that have five electrons in their d-orbitals resulting in a different spin state. This manipulation resulted in a different magnetic interaction between the metal-organic complexes and the Pb(111) superconducting substrate. Deposition of the Mn-TPyP molecules yields self-assembled long-range ordered molecular islands. The molecular islands consist of molecules with saddle shape conformations, very similar to the case of free based H_2-TPyP molecules on Ag(111). Additionally, the Mn-TPyP molecules show Shiba states at an energy close to the gap edge with

the *free spin* ground state. This is a signature of weak spin exchange interaction that originates from the small hybridization between the Mn center and the underlying substrate. In comparison with Fe-TPyP on Pb(111), this weak interaction might be due to a different saddle conformation such that the Mn-surface distance is increased.

To further manipulate the magnetic interaction between the Mn center and the underlying substrate, in the last part, we embedded the Mn atom into another organic ligand by substituting the pyridine end groups with phenyl-tert-butyl. Deposition of the Mn-TPTBP molecules onto Pb(111) at room temperature gives rise to the formation of ordered molecular islands. The magnetic fingerprint of the molecules is very similar to the case of Mn-TPyP, due to the weak exchange interaction of the Mn center with the Pb substrate. This indicates that, despite substituting the end groups, the Mn-sample distance did not change significantly.

The findings in this thesis give an overview of different ways to manipulate the properties of metal-organic structures. Our studies showed that the metal-atom substrate distances played a major role for the magnetic fingerprints among different metal-organic nanostructures. One strategy to tailor this atom-substrate distance could be to dose axial ligands like CO, NO, etc, as they have shown to alter the interaction to the substrate via the surface-trans-effect. Additionally, one could utilize various flexible organic ligands that can adapt distinct conformations under the influence of external forces, i.e., the electric field of the tip. Ultimately, this approach might allow to manipulate the hybridization between the embedded metals and the underlying substrate and consequently, yields different electronic and magnetic properties.

References

[1] Loth, S., Baumann, S., Lutz, C. P., Eigler, D. M. & Heinrich, A. J. Bistability in Atomic-Scale Antiferromagnets. *Science* **335**, 196 (2012).

[2] Miyamachi, T. *et al.* Robust spin crossover and memristance across a single molecule. *Nature communications* **3**, 938 (2012).

[3] Bogani, L. & Wernsdorfer, W. Molecular spintronics using single-molecule magnets. *Nature materials* **7**, 179 (2008).

[4] De Franceschi, S., Kouwenhoven, L., Schonenberger, C. & Wernsdorfer, W. Hybrid superconductor-quantum dot devices. *Nat Nano* **5**, 703–711 (2010).

[5] M. Tinkham. *Introduction to Superconductivity* (Dover Publications Inc., 2004), second edn.

[6] Essén, H. & Fiolhais, M. C. Meissner effect, diamagnetism, and classical physics—a review. *American Journal of Physics* **80**, 164–169 (2012).

[7] Bardeen, J., Cooper, L. N. & Schrieffer, J. R. Theory of Superconductivity. *Physical Review* **108**, 1175–1204 (1957).

[8] Bardeen, J., Cooper, L. N. & Schrieffer, J. R. Microscopic Theory of Superconductivity. *Physical Review* **106**, 162–164 (1957).

[9] Alonso, J. Electronic and atomic structure, and magnetism of transition-metal clusters. *Chemical reviews* **100**, 637–678 (2000).

[10] Yu, L. Bound State in Superconductors with Paramagnetic Impurities. *Acta Sin. Phys.* **21**, 75–91 (1965).

[11] Shiba, H. Classical Spins in Superconductors. *Progress of Theoretical Physics* **40**, 435–451 (1968).

[12] Rusinov, A. Superconductivity near a paramagnetic impurity. *Soviet Journal of Experimental and Theoretical Physics Letters* **9**, 85 (1969).

[13] Salkola, M. I., Balatsky, A. V. & Schrieffer, J. R. Spectral properties of quasiparticle excitations induced by magnetic moments in superconductors. *Physical Review B* **55**, 12648–12661 (1997).

[14] Yazdani, A., Jones, B. A., Lutz, C. P., Crommie, M. F. & Eigler, D. M. Probing the Local Effects of Magnetic Impurities on Superconductivity. *Science* **275**, 1767–1770 (1997).

[15] Ji, S.-H. *et al.* High-resolution scanning tunneling spectroscopy of magnetic impurity induced bound states in the superconducting gap of pb thin films. *Physical Review Letters* **100**, 226801 (2008).

[16] Franke, K. J., Schulze, G. & Pascual, J. I. Competition of Superconducting Phenomena and Kondo Screening at the Nanoscale. *Science* **332**, 940–944 (2011).

[17] Hatter, N., Heinrich, B. W., Ruby, M., Pascual, J. I. & Franke, K. J. Magnetic anisotropy in Shiba bound states across a quantum phase transition. *Nat Communications* **6** (2015).

[18] Heinrich, B. W., Braun, L., Pascual, J. I. & Franke, K. J. Tuning the Magnetic Anisotropy of Single Molecules. *Nano Letters* **15**, 4024–4028 (2015).

[19] Heinrich, B. W., Braun, L., Pascual, J. I. & Franke, K. J. Protection of excited spin states by a superconducting energy gap. *Nat Phys* **9**, 765–768 (2013).

[20] Https://en.wikipedia.org/wiki/Meissner-effect.

[21] Binnig, G., Rohrer, H., Gerber, C. & Weibel, E. Tunneling through a controllable vacuum gap. *Applied Physics Letters* **40**, 178–180 (1982).

[22] Binnig, G., Rohrer, H., Gerber, C. & Weibel, E. Surface Studies by Scanning Tunneling Microscopy. *Physical Review Letters* **49**, 57–61 (1982).

[23] Eigler, D. M. & Schweizer, E. K. Positioning single atoms with a scanning tunnelling microscope. *Nature* **344**, 524–526 (1990).

[24] Crommie, M. F., Lutz, C. P. & Eigler, D. M. Confinement of Electrons to Quantum Corrals on a Metal Surface. *Science* **262**, 218 (1993).

[25] Kuk, Y. & Silverman, P. Scanning tunneling microscope instrumentation. *Review of scientific instruments* **60**, 165–180 (1989).

[26] Julian Chen. *Introduction to Scanning Tunneling Microscopy* (Oxford University Press, 2007), second edn.

[27] Zugarramurdi, A., Zabala, N., Borisov, A. G. & Chulkov, E. V. Theoretical study of constant current scanning tunneling spectroscopy in Pb overlayers. *Physical Review B* **84**, 115422 (2011).

[28] Ziegler, M., Néel, N., Sperl, A., Kröger, J. & Berndt, R. Local density of states from constant-current tunneling spectra. *Physical Review B* **80**, 125402 (2009).

[29] Hansma, P. K. & Kirtley, J. Recent advances in inelastic electron tunneling spectroscopy. *Accounts of Chemical Research* **11**, 440–445 (1978).

[30] Weinberg, W. H. Inelastic Electron Tunneling Spectroscopy: A Probe of the Vibrational Structure of Surface Species. *Annual Review of Physical Chemistry* **29**, 115–139 (1978).

[31] Reed, M. A. Inelastic electron tunneling spectroscopy. *Materials Today* **11**, 46 – 50 (2008).

[32] Ternes, M. *Scanning tunneling spectroscopy at the single atom scale*. Ph.D. thesis, EPFL (2006).

[33] Hasegawa, Y. & Avouris, P. Direct observation of standing wave formation at surface steps using scanning tunneling spectroscopy. *Physical Review Letters* **71**, 1071 (1993).

[34] Hatter, N. *Fundamental Properties of Molecules on Surfaces*. Ph.D. thesis, Freie Universität Berlin (2016).

[35] Zhang, L., Miyamachi, T., Tomanić, T., Dehm, R. & Wulfhekel, W. A compact sub-kelvin ultrahigh vacuum scanning tunneling microscope with high energy resolution and high stability. *Review of Scientific Instruments* **82**, 103702 (2011).

[36] Kalff, F. E., Rebergen, M. P., Fahrenfort, E., Girovsky, J., Toskovic, R., Lado, J. L., Fernández-Rossier, J. & Otte, A. F. A kilobyte rewritable atomic memory. *Nat Nano* **advance online publication** (2016).

[37] De Franceschi, S., Kouwenhoven, L., Schonenberger, C. & Wernsdorfer, W. Hybrid superconductor-quantum dot devices. *Nat Nano* **5**, 703–711 (2010).

[38] Balatsky, A. V., Vekhter, I. & Zhu, J.-X. Impurity-induced states in conventional and unconventional superconductors. *Reviews of Modern Physics* **78**, 373–433 (2006).

[39] Ruby, M., Peng, Y., von Oppen, F., Heinrich, B. W. & Franke, K. J. Orbital picture of Yu-Shiba-Rusinov multiplets. *Physical Review Letters* **117**, 186801 (2016).

[40] Clay, J. & Kammerlingh Onnes, H. On the change of the resistance of metals at very low temperatures and the influence excerted on it by small amounts of mixtures. *textKNAW, Proceedings* **10 I**, 207–215 (1907).

[41] Kammerlingh Onnes, H. *Proc. K. Ned. Akad. Wet.* **14**, 113 (1911).

[42] Bogoliubov, N. N., Tolmachev, V. & Shirkov, D. A new method in the theory of superconductivity. *Translated from Russian (New York, Consultants Bureau, 1959)* (1960).

[43] Ruby, M., Heinrich, B. W., Pascual, J. I. & Franke, K. J. Experimental Demonstration of a Two-Band Superconducting State for Lead Using Scanning Tunneling Spectroscopy. *Physical Review Letters* **114**, 157001 (2015).

[44] Floris, A., Sanna, A., Massidda, S. & Gross, E. Two-band superconductivity in pb from ab initio calculations. *Physical Review B* **75**, 054508 (2007).

[45] Dante Gatteschi, Roberta Sessoli & Jacques Villain. *Molecular Nanomagnets* (Oxford University Press, 2006).

[46] Miessler, G. & Tarr, D. Inorganic chemistry. vol. 642 (1999).

[47] Dai, D., Xiang, H. & Whangbo, M.-H. Effects of spin-orbit coupling on magnetic properties of discrete and extended magnetic systems. *Journal of Computational Chemistry* **29**, 2187–2209 (2008).

[48] Bruno, P. Physical origins and theoretical models of magnetic anisotropy. *Magnetismus von Festkörpern und Grenzflächen* **24**, 1–28 (1993).

[49] Ternes, M. Spin excitations and correlations in scanning tunneling spectroscopy. *New Journal of Physics* **17**, 063016 (2015).

[50] Seth, R. & Woods, S. Electrical resistivity and deviations from Matthiessen's rule in dilute alloys of aluminum, cadmium, silver, and magnesium. *Physical Review B* **2**, 2961 (1970).

[51] Kondo, J. Resistance Minimum in Dilute Magnetic Alloys. *Progress of Theoretical Physics* **32**, 37–49 (1964).

[52] Madhavan, V., Chen, W., Jamneala, T., Crommie, M. F. & Wingreen, N. S. Tunneling into a Single Magnetic Atom: Spectroscopic Evidence of the Kondo Resonance. *Science* **280**, 567–569 (1998).

[53] Li, J., Schneider, W.-D., Berndt, R. & Delley, B. Kondo Scattering Observed at a Single Magnetic Impurity. *Physical Review Letters* **80**, 2893–2896 (1998).

[54] Cronenwett, S. M., Oosterkamp, T. H. & Kouwenhoven, L. P. A Tunable Kondo Effect in Quantum Dots. *Science* **281**, 540–544 (1998).

[55] Goldhaber-Gordon, D., Göres, J., Kastner, M. A., Shtrikman, H., Mahalu, D. & Meirav, U. From the Kondo Regime to the Mixed-Valence Regime in a Single-Electron Transistor. *Physical Review Letters* **81**, 5225–5228 (1998).

[56] Tsukahara, N., Shiraki, S., Itou, S., Ohta, N., Takagi, N. & Kawai, M. Evolution of Kondo resonance from a single impurity molecule to the two-dimensional lattice. *Physical Review Letters* **106**, 187201 (2011).

[57] Morr, D. K. Theory of scanning tunneling spectroscopy: from Kondo impurities to heavy fermion materials. *Reports on Progress in Physics* **80**, 014502 (2016).

[58] Girovsky, J. *et al.* Long-range ferrimagnetic order in a two-dimensional supramolecular kondo lattice. *Nature communications* **8**, 15388 (2017).

[59] Anderson, P. W. Localized magnetic states and Fermi-surface anomalies in tunneling. *Physical Review Letters* **17**, 95–97 (1966).

[60] Anderson, P. W. Localized Magnetic States in Metals. *Physical Review* **124**, 41–53 (1961).

[61] Schrieffer, J. & Wolff, P. Relation between the Anderson and Kondo hamiltonians. *Physical Review* **149**, 491 (1966).

[62] Hewson, A. C. *The Kondo Problem to Heavy Fermions* (Cambridge University Press, 1997).

[63] Ternes, M. and Heinrich, A. J. and Schneider, W.-D. Spectroscopic manifestations of the Kondo effect on single adatoms. *Journal of Physics: Condensed Matter* **21**, 053001 (2009).

[64] Fano, U. Effects of Configuration Interaction on Intensities and Phase Shifts. *Physical Review* **124**, 1866–1878 (1961).

[65] Nagaoka, K., Jamneala, T., Grobis, M. & Crommie, M. Temperature dependence of a single kondo impurity. *Physical review letters* **88**, 077205 (2002).

[66] Costi, T. A. Kondo Effect in a Magnetic Field and the Magnetoresistivity of Kondo Alloys. *Physical Review Letters* **85**, 1504–1507 (2000).

[67] Quay, C. H. L., Cumings, J., Gamble, S. J., Picciotto, R. d., Kataura, H. & Goldhaber-Gordon, D. Magnetic field dependence of the spin-1/2 and spin-1 Kondo effects in a quantum dot. *Physical Review B* **76**, 245311 (2007).

[68] Zhang, Y.-h. *et al.* Temperature and magnetic field dependence of a Kondo system in the weak coupling regime. *Nature Communications* **4**, 2110 (2013).

[69] von Oppen, F., Peng, Y. & Pientka, F. Topological superconducting phases in one dimension. *Topological Aspects of Condensed Matter Physics: Lecture Notes of the Les Houches Summer School: Volume 103, August 2014* **103**, 387 (2017).

[70] Matsuura, T. The effects of impurities on superconductors with kondo effect. *Progress of Theoretical Physics* **57**, 1823–1835 (1977).

[71] Satori, K., Shiba, H., Sakai, O. & Shimizu, Y. Numerical renormalization group study of magnetic impurities in superconductors. *Journal of the Physical Society of Japan* **61**, 3239–3254 (1992).

[72] Sakai, O., Shimizu, Y., Shiba, H. & Satori, K. Numerical renormalization group study of magnetic impurities in superconductors. ii. dynamical excitation spectra and spatial variation of the order parameter. *Journal of the Physical Society of Japan* **62**, 3181–3197 (1993).

[73] Heinrich, B. W., Pascual, J. I. & Franke, K. J. Single magnetic adsorbates on s-wave superconductors. *arXiv preprint arXiv:1705.03672* (2017).

[74] Flatté, M. E. & Byers, J. M. Local Electronic Structure of a Single Magnetic Impurity in a Superconductor. *Physical Review Letters* **78**, 3761–3764 (1997).

[75] Barth, J. V. Molecular architectonic on metal surfaces. *Annu. Rev. Phys. Chem.* **58**, 375–407 (2007).

[76] Cicoira, F., Santato, C. & Rosei, F. Two-dimensional nanotemplates as surface cues for the controlled assembly of organic molecules. *Stm and Afm Studies on (bio) molecular systems: Unravelling the nanoworld* 203–267 (2008).

[77] Liang, H. *et al.* Two-dimensional molecular porous networks constructed by surface assembling. *Coordination Chemistry Reviews* **253**, 2959–2979 (2009).

[78] Otero, R., Gallego, J. M., Vázquez de Parga, A. L., Martín, N. & Miranda, R. Molecular self-assembly at solid surfaces. *Advanced Materials* **23**, 5148–5176 (2011).

[79] Zhang, J. L., Zhong, S., Zhong, J. Q., Niu, T. C., Hu, W. P., Wee, A. T. S. & Chen, W. Rational design of two-dimensional molecular donor–acceptor nanostructure arrays. *Nanoscale* **7**, 4306–4324 (2015).

[80] Barth, J. V. Fresh perspectives for surface coordination chemistry. *Surface Science* **603**, 1533–1541 (2009).

[81] Lin, N., Stepanow, S., Ruben, M. & Barth, J. V. Surface-confined supramolecular coordination chemistry. In *Templates in Chemistry III*, 1–44 (Springer, 2008).

[82] Theobald, J. A., Oxtoby, N. S., Phillips, M. A., Champness, N. R. & Beton, P. H. Controlling molecular deposition and layer structure with supramolecular surface assemblies. *Nature* **424**, 1029–1031 (2003).

[83] Wintjes, N., Bonifazi, D., Cheng, F., Kiebele, A., Stöhr, M., Jung, T., Spillmann, H. & Diederich, F. A supramolecular multiposition rotary device. *Angewandte Chemie* **119**, 4167–4170 (2007).

[84] Pivetta, M., Pacchioni, G. E., Schlickum, U., Barth, J. V. & Brune, H. Formation of Fe cluster superlattice in a metal-organic quantum-box network. *Physical Review Letters* **110**, 086102 (2013).

[85] Palma, C.-A., Björk, J., Rao, F., Kühne, D., Klappenberger, F. & Barth, J. V. Topological dynamics in supramolecular rotors. *Nano Letters* **14**, 4461–4468 (2014).

[86] Gonzalez-Lakunza, N., Fernandez-Torrente, I., Franke, K., Lorente, N., Arnau, A. & Pascual, J. Formation of dispersive hybrid bands at an organic-metal interface. *Physical Review Letters* **100**, 156805 (2008).

[87] Lobo-Checa, J., Matena, M., Müller, K., Dil, J. H., Meier, F., Gade, L. H., Jung, T. A. & Stöhr, M. Band formation from coupled quantum dots formed by a nanoporous network on a copper surface. *Science* **325**, 300–303 (2009).

[88] Klappenberger, F. *et al.* Tunable quantum dot arrays formed from self-assembled metal-organic networks. *Physical Review Letters* **106**, 026802 (2011).

[89] Gambardella, P. *et al.* Supramolecular control of the magnetic anisotropy in two-dimensional high-spin Fe arrays at a metal interface. *Nature Materials* **8**, 189–193 (2009).

[90] Umbach, T. *et al.* Ferromagnetic coupling of mononuclear Fe centers in a self-assembled metal-organic network on Au (111). *Physical Review Letters* **109**, 267207 (2012).

[91] Abdurakhmanova, N., Tseng, T.-C., Langner, A., Kley, C.S., Sessi, V., Stepanow, S. & Kern, K. Superexchange-Mediated Ferromagnetic Coupling in Two-Dimensional Ni-TCNQ Networks on Metal Surfaces. *Physical Review Letters* **110**, 027202 (2013).

[92] Röntynen, J. & Ojanen, T. Topological Superconductivity and High Chern Numbers in 2d Ferromagnetic Shiba Lattices. *Physical review letters* **114**, 236803 (2015).

[93] Lu, Y., He, W.-Y., Xu, D.-H., Lin, N. & Law, K. T. Platform for engineering topological superconductors: Superlattices on Rashba superconductors. *Physical Review B* **94**, 024507 (2016).

[94] Kanai, K., Ikame, T., Ouchi, Y. & Seki, K. Molecular orientation and electronic structure of 11, 11, 12, 12-tetracyanonaphtho-2, 6-quinodimethane vacuum-deposited on metal substrates: Charge transfer, complexation, and potassium doping. *Journal of Applied Physics* **105**, 023703 (2009).

[95] The orientation of the Pb lattice was determined from atomic resolution images in a different preparation and from Ne subsurface inclusions, which result in hexagonal shaped apparent depression/protrusions in the STM images due to the formation of quantum well states.

[96] Umbach, T., Fernandez-Torrente, I., Ladenthin, J., Pascual, J. & Franke, K. Enhanced charge transfer in a monolayer of the organic charge transfer complex TTF–TNAP on Au (111). *Journal of Physics: Condensed Matter* **24**, 354003 (2012).

[97] Fiedler, B., Reckien, W., Bredow, T., Beck, J. & Sokolowski, M. Structure and charge transfer in binary ordered monolayers of two sulfur-containing donor molecules and tnap on the au (111) surface. *The Journal of Physical Chemistry C* **118**, 3035–3048 (2014).

[98] Yu, D. & Scheffler, M. First-principles study of low-index surfaces of lead. *Physical Review B* **70**, 155417 (2004).

[99] Braun, S., Salaneck, W. R. & Fahlman, M. Energy-level alignment at organic/metal and organic/organic interfaces. *Advanced Materials* **21**, 1450–1472 (2009).

[100] Torrente, I. F., Franke, K. J. & Pascual, J. I. Spectroscopy of c60 single molecules: the role of screening on energy level alignment. *Journal of Physics: Condensed Matter* **20**, 184001 (2008).

[101] Ishii, H., Sugiyama, K., Ito, E. & Seki, K. Energy Level Alignment and Interfacial Electronic Structures at Organic/Metal and Organic/Organic Interfaces. *Advanced Materials* **11**, 605–625 (1999).

[102] Tseng, T.-C. *et al.* Two-dimensional metal-organic coordination networks of Mn-7, 7, 8, 8-tetracyanoquinodimethane assembled on Cu (100): Structural, electronic, and magnetic properties. *Physical Review B* **80**, 155458 (2009).

[103] Tseng, T.-C., Abdurakhmanova, N., Stepanow, S. & Kern, K. Hierarchical assembly and reticulation of two-dimensional Mn-and Ni–TCNQ x (x= 1, 2, 4) coordination structures on a metal surface. *The Journal of Physical Chemistry C* **115**, 10211–10217 (2011).

[104] Faraggi, M. N., Jiang, N., Gonzalez-Lakunza, N., Langner, A., Stepanow, S., Kern, K. & Arnau, A. Bonding and charge transfer in metal–organic coordination networks on Au (111) with strong acceptor molecules. *The Journal of Physical Chemistry C* **116**, 24558–24565 (2012).

[105] Abdurakhmanova, N., Floris, A., Tseng, T.-C., Comisso, A., Stepanow, S., De Vita, A. & Kern, K. Stereoselectivity and electrostatics in charge-transfer Mn-and Cs-TCNQ4 networks on Ag (100). *Nature Communications* **3**, 940 (2012).

[106] Yang, Z. *et al.* Orbital redistribution in molecular nanostructures mediated by metal–organic bonds. *ACS nano* **8**, 10715–10722 (2014).

[107] Perry, C., Haq, S., Frederick, B. & Richardson, N. Face specificity and the role of metal adatoms in molecular reorientation at surfaces. *Surface Science* **409**, 512–520 (1998).

[108] Pawin, G. *et al.* A surface coordination network based on substrate-derived metal adatoms with local charge excess. *Angewandte Chemie International Edition* **47**, 8442–8445 (2008).

[109] Björk, J. *et al.* STM fingerprint of molecule–adatom interactions in a self-assembled metal–organic surface coordination network on Cu (111). *Physical Chemistry Chemical Physics* **12**, 8815–8821 (2010).

[110] Xiao, J. *et al.* Temperature-dependent chemical and structural transformations from 2H-tetraphenylporphyrin to copper (ii)-tetraphenylporphyrin on Cu (111). *The Journal of Physical Chemistry C* **116**, 12275–12282 (2012).

[111] Sirtl, T. *et al.* Control of intermolecular bonds by deposition rates at room temperature: hydrogen bonds versus metal coordination in trinitrile monolayers. *Journal of the American Chemical Society* **135**, 691–695 (2013).

[112] Umbach, T. *et al.* Site-specific bonding of copper adatoms to pyridine end groups mediating the formation of two-dimensional coordination networks on metal surfaces. *Physical Review B* **89**, 235409 (2014).

[113] Rodríguez-Fernández, J., Lauwaet, K., Herranz, M. Á., Martín, N., Gallego, J. M., Miranda, R. & Otero, R. Temperature-controlled metal/ligand stoichiometric ratio in Ag-TCNE coordination networks. *The Journal of Chemical Physics* **142**, 101930 (2015).

[114] Lian, J. *et al.* Mapping antibonding electron states of a Pb adatom on Pb (111). *Physical Review B* **81**, 195411 (2010).

[115] Katz, M. J., Aguiar, P. M., Batchelor, R. J., Bokov, A. A., Ye, Z.-G., Kroeker, S. & Leznoff, D. B. Structure and multinuclear solid-state NMR of a highly birefringent lead- gold cyanide coordination polymer. *Journal of the American Chemical Society* **128**, 3669–3676 (2006).

[116] Gil, D. M., Avila, M., Reguera, E., Pagola, S., Gómez, M. I. & Carbonio, R. E. Lead hexacyanoferrate (ii) tetrahydrate: Crystal structure, FTIR spectroscopy and thermal decomposition studies. *Polyhedron* **33**, 450–455 (2012).

[117] Lyu, G., Zhang, R., Zhang, X., Liu, P. N. & Lin, N. On-surface assembly of low-dimensional Pb-coordinated metal–organic structures. *Journal of Materials Chemistry C* **3**, 3252–3257 (2015).

[118] Shimoni-Livny, L., Glusker, J. P. & Bock, C. W. Lone pair functionality in divalent lead compounds. *Inorganic Chemistry* **37**, 1853–1867 (1998).

[119] Yang, J., Li, G.-D., Cao, J.-J., Yue, Q., Li, G.-H. & Chen, J.-S. Structural variation from 1d to 3d: effects of ligands and solvents on the construction of lead (ii)–organic coordination polymers. *Chemistry-A European Journal* **13**, 3248–3261 (2007).

[120] Papageorgiou, N., Ferro, Y., Salomon, E., Allouche, A., Layet, J., Giovanelli, L. & Le Lay, G. Geometry and electronic structure of lead phthalocyanine: Quantum calculations via density-functional theory and photoemission measurements. *Physical Review B* **68**, 235105 (2003).

[121] Wäckerlin, C., Iacovita, C., Chylarecka, D., Fesser, P., Jung, T. A. & Ballav, N. Assembly of 2D ionic layers by reaction of alkali halides with the organic electrophile 7, 7, 8, 8-tetracyano-p-quinodimethane (TCNQ). *Chemical Communications* **47**, 9146–9148 (2011).

[122] Umbach, T. *et al.* Atypical charge redistribution over a charge-transfer monolayer on a metal. *New Journal of Physics* **15**, 083048 (2013).

[123] Repp, J., Meyer, G. & Rieder, K.-H. Snell's law for surface electrons: Refraction of an electron gas imaged in real space. *Physical Review Retters* **92**, 036803 (2004).

[124] Lauwaet, K., Schouteden, K., Janssens, E., Van Haesendonck, C. & Lievens, P. Dependence of the NaCl/Au (111) interface state on the thickness of the nacl layer. *Journal of Physics: Condensed Matter* **24**, 475507 (2012).

[125] Heidorn, S.-C., Sabellek, A. & Morgenstern, K. Size dependence of the dispersion relation for the interface state between NaCl (100) and Ag (111). *Nano Letters* **14**, 13–17 (2013).

[126] Liao, M.-S. & Scheiner, S. Electronic structure and bonding in metal porphyrins, metal= Fe, Co, Ni, Cu, Zn. *The Journal of Chemical Physics* **117**, 205–219 (2002).

[127] Auwärter, W., Écija, D., Klappenberger, F. & Barth, J. V. Porphyrins at interfaces. *Nature Chemistry* **7**, 105–120 (2015).

[128] Schouteden, K., Ivanova, T., Li, Z., Iancu, V., Janssens, E. & Van Haesendonck, C. Probing magnetism in 2D molecular networks after in situ metalation by transition metal atoms. *The Journal of Physical Chemistry Letters* **6**, 1048–1052 (2015).

[129] Wang, Y., Zheng, X. & Yang, J. Kondo screening and spin excitation in few-layer CoPc molecular assembly stacking on Pb (111) surface: A DFT+ HEOM study. *The Journal of Chemical Physics* **145**, 154301 (2016).

[130] Zhao, A. *et al.* Controlling the Kondo effect of an adsorbed magnetic ion through its chemical bonding. *Science* **309**, 1542–1544 (2005).

[131] Niu, T. & Li, A. Exploring single molecules by scanning probe microscopy: porphyrin and phthalocyanine. *The Journal of Physical Chemistry Letters* **4**, 4095–4102 (2013).

[132] Zotti, L., Teobaldi, G., Hofer, W., Auwärter, W., Weber-Bargioni, A. & Barth, J. Ab-initio calculations and STM observations on tetrapyridyl and Fe(II)-tetrapyridyl-porphyrin molecules on Ag(111). *Surface Science* **601**, 2409–2414 (2007).

[133] Iancu, V., Deshpande, A. & Hla, S.-W. Manipulating Kondo temperature via single molecule switching. *Nano Letters* **6**, 820–823 (2006).

[134] Iancu, V., Schouteden, K., Li, Z. & Van Haesendonck, C. Electron-phonon coupling in engineered magnetic molecules. *Chemical Communications* **52**, 1359–11362 (2016).

[135] Gottfried, J. M. Surface chemistry of porphyrins and phthalocyanines. *Surface Science Reports* **70**, 259–379 (2015).

[136] Auwärter, W., Weber-Bargioni, A., Riemann, A., Schiffrin, A., Gröning, O., Fasel, R. & Barth, J. V. Self-assembly and conformation of tetrapyridyl-porphyrin molecules on Ag(111). *The Journal of Chemical Physics* **124**, 194708 (2006).

[137] Zoldan, V. C., Faccio, R., Gao, C. & Pasa, A. A. Coupling of cobalt–tetraphenylporphyrin molecules to a copper nitride layer. *The Journal of Physical Chemistry C* **117**, 15984–15990 (2013).

[138] Pham, V. D. *et al.* Control of Molecule–Metal Interaction by Hydrogen Manipulation in an Organic Molecule. *The Journal of Physical Chemistry Letters* **7**, 1416–1421 (2016).

[139] Albrecht, F., Bischoff, F., Auwärter, W., Barth, J. V. & Repp, J. Direct identification and determination of conformational response in adsorbed individual nonplanar molecular species using noncontact atomic force microscopy. *Nano Letters* **16**, 7703–7709 (2016).

[140] Zhang, Q., Kuang, G., Pang, R., Shi, X. & Lin, N. Switching molecular Kondo effect via supramolecular interaction. *ACS Nano* **9**, 12521–12528 (2015).

[141] Lovat, G., Forrer, D., Abadía, M., Dominguez, M., Casarin, M., Rogero, C., Vittadini, A. & Floreano, L. On Surface Synthesis of a Pure and Long Range Ordered Titanium (IV)-Porphyrin Contact Layer on Titanium Dioxide. *The Journal of Physical Chemistry C* **121**, 13738–13746 (2017).

[142] Chen, X., Lei, S., Lotze, C., Czekelius, C., Paulus, B. & Franke, K. J. Conformational adaptation and manipulation of manganese tetra (4-pyridyl) porphyrin molecules on Cu (111). *The Journal of Chemical Physics* **146**, 092316 (2017).

[143] Auwärter, W., Weber-Bargioni, A., Brink, S., Riemann, A., Schiffrin, A., Ruben, M. & Barth, J. V. Controlled metalation of self-assembled porphyrin nanoarrays in two dimensions. *chemical Physics and Physical Chemistry* **8**, 250–4 (2007).

[144] Jarvis, S. P. *et al.* Physisorption Controls the Conformation and Density of States of an Adsorbed Porphyrin. *The Journal of Physical Chemistry C* **119**, 27982–27994 (2015).

[145] Minamitani, E., Tsukahara, N., Matsunaka, D., Kim, Y., Takagi, N. & Kawai, M. Symmetry-Driven Novel Kondo Effect in a Molecule. *Physical Review Letters* **109**, 1–5 (2012).

[146] Liu, L. *et al.* Revealing the Atomic Site-Dependent g Factor within a Single Magnetic Molecule via the Extended Kondo Effect. *Physical Review Letters* **114**, 126601 (2015).

[147] Minamitani, E., Fu, Y.-S., Xue, Q.-K., Kim, Y. & Watanabe, S. Spatially extended underscreened Kondo state from collective molecular spin. *Physical Review B* **92** (2015).

[148] A low-spin Fe (III) complex with 100-ps ligand-to-metal charge transfer photoluminescence, author=Chábera, Pavel and Liu, Yizhu and Prakash, Om and Thyrhaug, Erling and El Nahhas, Amal and Honarfar, Alireza and Essén, Sofia and Fredin, Lisa A and Harlang, Tobias CB and Kjær, Kasper S and others, journal=Nature, volume=543, number=7647, pages=695–699, year=2017, publisher=Nature Research .

[149] Bartolomé, J., Monton, C. & Schuller, I. K. Magnetism of metal phthalocyanines. In *Molecular Magnets*, 221–245 (Springer, 2014).

[150] Warner, B., El Hallak, F., Prüser, H., Ajibade, A., Gill, T. G., Fisher, A. J., Persson, M. & Hirjibehedin, C. F. Controlling electronic access to the spin excitations of a single molecule in a tunnel junction. *Nanoscale* **9**, 4053–4057 (2017).

[151] Wang, W., Pang, R., Kuang, G., Shi, X., Shang, X., Liu, P. N. & Lin, N. Intramolecularly resolved Kondo resonance of high-spin Fe-porphyrin adsorbed on Au(111). *Physical Review B* **91**, 045440 (2015).

[152] Houwaart, T., Le Bahers, T., Sautet, P., Auwärter, W., Seufert, K., Barth, J. V. & Bocquet, M.-L. Scrutinizing individual CoTPP molecule adsorbed on coinage metal surfaces from the interplay of STM experiment and theory. *Surface Science* **635**, 108–114 (2015).

[153] Seufert, K., Bocquet, M.-L., Auwärter, W., Weber-Bargioni, A., Reichert, J., Lorente, N. & Barth, J. V. Cis-dicarbonyl binding at cobalt and iron porphyrins with saddle-shape conformation. *Nature Chemistry* **3**, 114–119 (2011).

[154] Donovan, P., Robin, A., Dyer, M. S., Persson, M. & Raval, R. Unexpected deformations induced by surface interaction and chiral self-assembly of CoII-Tetraphenylporphyrin (Co-TPP) adsorbed on Cu (110): A combined STM and periodic DFT study. *Chemistry-A European Journal* **16**, 11641–11652 (2010).

[155] Frisch, M. J. & *et al*. Gaussian 09, revision D.01 (2016). Gaussian, Inc., Wallingford CT, http://gaussian.com/g09citation/, 2017-07-24.

[156] Hay, P. J. & Wadt, W. R. Ab initio effective core potentials for molecular calculations. potentials for k to au including the outermost core orbitals. *The Journal of Chemical Physics* **82**, 299–310 (1985).

[157] Ohta, N., Arafune, R., Tsukahara, N., Kawai, M. & Takagi, N. Enhancement of inelastic electron tunneling conductance caused by electronic decoupling in iron phthalocyanine bilayer on ag (111). *The Journal of Physical Chemistry C* **117**, 21832–21837 (2013).

[158] Ohta, N., Arafune, R., Tsukahara, N., Takagi, N. & Kawai, M. Adsorbed states of iron (ii) phthalocyanine on ag (111) studied by high-resolution electron energy loss spectroscopy. *Surface and Interface Analysis* **46**, 1253–1256 (2014).

[159] Mugarza, A., Robles, R., Krull, C., Korytár, R., Lorente, N. & Gambardella, P. Electronic and magnetic properties of molecule-metal interfaces: Transition-metal phthalocyanines adsorbed on ag (100). *Physical Review B* **85**, 155437 (2012).

[160] Auwärter, W. *et al.* Conformational Adaptation and Selective Adatom Capturing of Tetrapyridyl-porphyrin Molecules on a Copper (111) Surface. *Journal of the American Chemical Society* **129**, 11279–11285 (2007).

[161] Auwärter, W. *et al.* Site-specific electronic and geometric interface structure of Co-tetraphenyl-porphyrin layers on Ag(111). *Physical Review B* **81** (2010).

[162] Scudiero, L., Barlow, D. E., Mazur, U. & Hipps, K. W. Scanning Tunneling Microscopy, Orbital-Mediated Tunneling Spectroscopy, and Ultraviolet Photoelectron Spectroscopy of Metal(II) Tetraphenylporphyrins Deposited from Vapor. *Journal of the American Chemical Society* **123**, 4073–4080 (2001).

[163] Lauhon, L. & Ho, W. Effects of temperature and other experimental variables on single molecule vibrational spectroscopy with the scanning tunneling microscope. *Review of Scientific Instruments* **72**, 216–223 (2001).

[164] Stipe, B. C., Rezaei, M. A. & Ho, W. Single-Molecule Vibrational Spectroscopy and Microscopy. *Science* **280**, 1732–1735 (1998).

[165] Heinrich, B. W., Ahmadi, G., Müller, V. L., Braun, L., Pascual, J. I. & Franke, K. J. Change of the Magnetic Coupling of a Metal–Organic Complex with the Substrate by a Stepwise Ligand Reaction. *Nano Letters* **13**, 4840–4843 (2013).

[166] Tanaka, K., Elkaim, E., Li, L., Jue, Z. N., Coppens, P. & Landrum, J. Electron density studies of porphyrins and phthalocyanines. IV. Electron density distribution in crystals of (meso-tetraphenylporphinato) iron(II). *The Journal of Chemical Physics* **84**, 6969–6978 (1986).

[167] Ichibha, T., Hou, Z., Hongo, K. & Maezono, R. New Insight into the Ground State of FePc: A Diffusion Monte Carlo Study. *Scientific Reports* **7** (2017).

[168] Wang, Y., Zheng, X. & Yang, J. Environment-modulated Kondo phenomena in FePc/Au(111) adsorption systems. *Physical Review B* **93**, 115114 (2016).

[169] Hirjibehedin, C. F., Lutz, C. P. & Heinrich, A. J. Spin Coupling in Engineered Atomic Structures. *Science* **312**, 1021–1024 (2006).

[170] Giessibl, F. J. Advances in atomic force microscopy. *Reviews of Modern Physics* **75**, 949 (2003).

[171] Choi, D.-J., Rubio-Verdú, C., de Bruijckere, J., Ugeda, M. M., Lorente, N. & Pascual, J. I. Mapping the orbital structure of impurity bound states in a superconductor. *Nature Communications* **8**, 15175 (2017).

[172] Žitko, R., Peters, R. & Pruschke, T. Properties of anisotropic magnetic impurities on surfaces. *Physical Review B* **78**, 224404 (2008).

[173] Ternes, M., Schneider, W.-D., Cuevas, J.-C., Lutz, C. P., Hirjibehedin, C. F. & Heinrich, A. J. Subgap structure in asymmetric superconducting tunnel junctions. *Physical Review B* **74**, 132501 (2006).

[174] Brand, J., Ribeiro, P., Néel, N., Kirchner, S. & Kröger, J. Impact of atomic-scale contact geometry on Andreev reflection. *Physical Review Letters* **118**, 107001 (2017).

[175] Flatté, M. E. & Byers, J. M. Local electronic structure of defects in superconductors. *Physical Review B* **56**, 11213 (1997).

[176] Ruby, M., Pientka, F., Peng, Y., von Oppen, F., Heinrich, B. W. & Franke, K. J. Tunneling Processes into Localized Subgap States in Superconductors. *Physical Review Letters* **115**, 087001 (2015).

[177] Žitko, R., Lim, J. S., López, R. & Aguado, R. Shiba states and zero-bias anomalies in the hybrid normal-superconductor Anderson model. *Physical Review B* **91**, 045441 (2015).

[178] von Bergmann, K., Ternes, M., Loth, S., Lutz, C. P. & Heinrich, A. J. Spin Polarization of the Split Kondo State. *Physical Review Letters* **114**, 076601 (2015).

[179] Bauer, J., Pascual, J. I. & Franke, K. J. Microscopic resolution of the interplay of Kondo screening and superconducting pairing: Mn-phthalocyanine molecules adsorbed on superconducting Pb (111). *Physical Review B* **87**, 075125 (2013).

[180] Plihal, M. & Gadzuk, J. W. Nonequilibrium theory of scanning tunneling spectroscopy via adsorbate resonances: Nonmagnetic and Kondo impurities. *Physical Review B* **63**, 085404 (2001).

[181] Knorr, N., Schneider, M. A., Diekhöner, L., Wahl, P. & Kern, K. Kondo Effect of Single Co Adatoms on Cu Surfaces. *Physical Review Letters* **88**, 096804 (2002).

[182] Újsághy, O., Kroha, J., Szunyogh, L. & Zawadowski, A. Theory of the Fano resonance in the STM tunneling density of states due to a single Kondo impurity. *Physical Review Letters* **85**, 2557 (2000).

[183] Sharifzadeh, S., Huang, P. & Carter, E. A. Origin of tunneling lineshape trends for Kondo states of Co adatoms on coinage metal surfaces. *Journal of Physics: Condensed Matter* **21**, 355501 (2009).

[184] Figgins, J. & Morr, D. K. Differential conductance and quantum interference in kondo systems. *Physical review letters* **104**, 187202 (2010).

[185] Frank, S. & Jacob, D. Orbital signatures of Fano-Kondo line shapes in STM adatom spectroscopy. *Physical Review B* **92**, 235127 (2015).

[186] Karolak, M. & Jacob, D. Effects of valence, geometry and electronic correlations on transport in transition metal benzene sandwich molecules. *Journal of Physics: Condensed Matter* **28**, 445301 (2016).

[187] Meyer, J. *et al.* Influence of organic ligands on the line shape of the kondo resonance. *Physical Review B* **93**, 155118 (2016).

[188] Feng, W., Liu, Q., Lai, X. & Zhao, A. The kondo tip decorated by the co atom. *Nanotechnology* **27**, 455203 (2016).

[189] Gargiani, P., Betti, M. G., Taleb Ibrahimi, A., Le Feýre, P. & Modesti, S. Orbital symmetry of the Kondo state in adsorbed FePc molecules on the Au (110) metal surface. *The Journal of Physical Chemistry C* **120**, 28527–28532 (2016).

[190] Brune, H. & Gambardella, P. Magnetism of individual atoms adsorbed on surfaces. *Surface Science* **603**, 1812–1830 (2009).

[191] Basumatary, D., Lal, R. A. & Kumar, A. Synthesis, and characterization of low-and high-spin manganese (II) complexes of polyfunctional adipoyldihydrazone: Effect of coordination of N-donor ligands on stereo-redox chemistry. *Journal of Molecular Structure* **1092**, 122–129 (2015).

[192] Kügel, J., Karolak, M., Senkpiel, J., Hsu, P.-J., Sangiovanni, G. & Bode, M. Relevance of Hybridization and Filling of 3d Orbitals for the Kondo Effect in Transition Metal Phthalocyanines. *Nano Letters* **14**, 3895–3902 (2014).

[193] Stróżecka, A., Soriano, M., Pascual, J. I. & Palacios, J. J. Reversible Change of the Spin State in a Manganese Phthalocyanine by Coordination of CO Molecule. *Physical Review Letters* **109**, 147202 (2012).

[194] Ali, M. E., Sanyal, B. & Oppeneer, P. M. Tuning the magnetic interaction between manganese porphyrins and ferromagnetic Co substrate through dedicated control of the adsorption. *The Journal of Physical Chemistry C* **113**, 14381–14383 (2009).

[195] Chylarecka, D. *et al.* Indirect magnetic coupling of manganese porphyrin to a ferromagnetic cobalt substrate. *The Journal of Physical Chemistry C* **115**, 1295–1301 (2010).

[196] Chen, X. *Structural, Electronic and Switching Properties of Metalloporphyrin Molecules on Metal Surfaces*. Ph.D. thesis, Freie Universität Berlin (2015).

List of Abbreviations

DOS	(local) density of states
DFT	density functional theory
Fe-TPyP	iron tetrapyridine porphyrin
FeOEP	iron octaethyl porphyrin
HOMO	highest occupied molecular orbital
HWHM	half width at half maximum
LUMO	lowest unoccupied molecular orbital
M-TPyP	metal tetrapyridine porphyrin
Mn-TPyP	manganese tetrapyridine porphyrin
Mn-TPTBP	manganese tetraphenyltertbutyl porphyrin
MnPc	manganese phthalocyanine
NaCl	sodium chloride
STM	(low temperature) scanning tunneling microscopy
STS	scanning tunneling spectroscopy
TNAP	11, 11, 12, 12-tetracyanonaphtho-2, 6-quinodimethane
UHV	ultra high vacuum

List of Publications

Publications related to this thesis

G. Ahmadi and K. J. Franke
Self-assembly of tetracyanonaphtho-quinodimethane (TNAP) based metal-organic networks on Pb(111): Structural, electronic, and magnetic properties
Applied Surface Science **373**, 2-7 (2015)

Publications not related to this thesis

M. Bernien, A. Krüger, C. Schmidt, Sören T. Waßerroth, G. Ahmadi, B. W. Heinrich, M. Schneider, P. W. Brouwer, K. J. Franke, E. Weschke, W. Kuch,
Magnetic Coupling of Gd3N@C80 Endohedral Fullerenes to a Substrate
Phys. Rev. Lett. **111**, 167203 (2013)

B. W. Heinrich, G. Ahmadi, V. L. Müller, L. Braun, J. I. Pascual, K. J. Franke,
Change of the magnetic coupling of a metal-organic complex with the substrate by a stepwise ligand reaction
NanoLetters **13**, 4840 (2013)

R. Malekfar, G. Ahmadi A. Cheraghi, J. Rohollahnejad, F. Sahraeian, M. Khanzadeh
Micro-Raman Scattering of KTP (KTiOPO4) Nanocrystallites synthesized by sol-gel Modified Pechini Method
J. vibrational Spectroscopy **51**, 308 (2009)

R. Malekfar, A.Cheraghi, G. Ahmadi M. Khanzadeh
Raman Spectra and Structural Data of the Nanocrystalline KTP (KTiOPO4) Synthesized by Pechini Method
J. Acta Physica Polonica A **6**, 116 (2009)

Conference Contributions

2008

- Sokendai Asian Winter School Dec 9-12. 2008, Okazaki, Japan.
  (Poster) *The effects of some rare earth elements doping on the lattice vibrations of KTP (KTiOPO4) nanocrystallites synthesized by Pechini method*

2013

- DPG Spring Meeting of the Condensed Matter Section, Regensburg, Germany, 10.03 - 15.03.2013
  (poster) *Monitoring the ring closure on the ligand of an Fe-Porphyrin molecule*

  (Oral presentation) *Modifying the magnetic properties of an Fe-Porphyrin molecule by in-situ chemical reaction of the organic ligand* Workshop of the SFB 658-Integrated Research Training Group, Zeuthen, Germany 16.05 - 17.05.2013

2014

- DPG Spring Meeting of the Condensed Matter Section, Dresden, Germany, 30.03 - 04.04.2014
  (Poster) *Electronic and magnetic properties of $Gd_3N@C_{80}$ on Cu(100)*
- 563^{th} WE-Heraeus Seminar: Functional Molecules at Surfaces, Bad Honnef, Germany, 19.05 - 21.05.2014
  (Poster) *Electronic and magnetic properties of $Gd_3N@C_{80}$ on Cu(100)*

2015

- DPG Spring Meeting of the Condensed Matter Section, Berlin, Germany, 15.03 - 20.03.2015
  (Poster) *Structural and electronic properties of metal-organic networks on Pb(111)*

Acknowledgements

First of all special thanks goes to Prof. Katharina Franke, who gave me the ticket for being a part of her group and conduct my research. Without her support, I would have not been able to stay here and finish my dissertation during all difficult last five and half years. There are not enough words to value her personality, responsibility, understanding, kindness and, on top of all, her scientific character. I will never be able to thank you enough, Katharina. I also would like to thank Prof. Wolfgang Kuch for being my second supervisor and for reading my thesis in such a short time. Many thanks go also to Laeti, Daniela, Chris, Ben, Micha, Nino, Gael and of course Isa for helping me through the process of my doctorate, with helpful discussions, good ideas, and the proof reading of my thesis.

I spent a really great time in the group thanks to its strong group spirit. Coffee clubs, cake clubs, ice cream clubs and many other group social events made me enjoy every day of my life during last five and half years. All former and present members of the group convinced me that, despite our cultural differences, we can build a great friendship. Anna, Martina, Li, Bo, Yung, Rory, Max, Asieh, Sergey, Rojhat, Nils, Nils B, Olaf, Lisa, Timo, Wibke, Mark, Tobi, Paul, Eva, Valentin, Janina.... ohhh I can't remember the rest, I might be getting old. I had really cheerful chats with Prof. Nacho Pascual during his visits to the group in Berlin. I also want to thank the group's secretary, Birgit Dabisch, for helping me through complicated German bureaucracy: danke Birgit!

Additionally, I want to thank all the members of the Iranian mafia in our department, Nazanin, Asieh, Maryam, Zahra, Siavash, reza, Hossein, Mehdi, Ghazaleh, Mojtaba, ... Sepas bacheha.

I would like to thank my husband for his understanding and standing by my side always. Special thanks goes to my lovely and beautiful daughter Kani. I would like to thank the rest of my family, my father, my sister, my brothers, my aunts, my uncles, my grandmother Daiga, for their support and non-stop love. Additionally, I want to thank our family friends, Shahla and Jamal and their lovely girls for their warm family atmosphere which minimized our homesick feeling.

Last but not least, I want to dedicate my deepest gratitude to the soul of my mother, Parvin, for all her love, responsibility, kindness, braveness, and for showing me how to fight for life. She convinced me, despite all the discrimination, complications, and difficulties which we have been through, that there is always a chance to have a happy life. I will love you mom forever and I miss you so much.

Selbstständigkeitserklärung

Hiermit erkläre ich, dass ich die vorliegende Arbeit selbständig und nur unter Verwendung der angegebenen Literatur und Hilfsmittel angefertigt habe. Zudem erkläre ich, dass diese Arbeit in keinem früheren Promotionsverfahren eingereicht und dort angenommen oder für ungenügend befunden wurde.

Own Work Declaration

Hereby I declare to have made this thesis on my own only by use of the denoted literature and resources. Contents taken over from external sources, directly or indirectly, are denoted as such.

Berlin, 25. July 2017